PROPERTIES OF INORGANICALLY SURFACE-MODIFIED ZEOLITES AND ZEOLITE/ POLYIMIDE NANOCOMPOSITE MEMBRANES

A Dissertation
Presented to
The Academic Faculty

by

Megan Elizabeth Lydon

In Partial Fulfillment
of the Requirements for the Degree
Doctorate of Philosophy in the
School of Chemistry and Biochemistry

Georgia Institute of Technology
August 2013

PROPERTIES OF INORGANICALLY SURFACE-MODIFIED ZEOLITES AND ZEOLITE/ POLYIMIDE NANOCOMPOSITE MEMBRANES

Approved by:

Dr. Christopher W. Jones, Advisor
School of Chemical & Biomolecular Engineering
School of Chemistry and Biochemistry
Georgia Institute of Technology

Dr. Angus Wilkinson
School of Chemistry and Biochemistry
Georgia Institute of Technology

Dr. Sankar Nair, Advisor
School of Chemical & Biomolecular Engineering
Georgia Institute of Technology

Dr. Mostafa El-Sayed
School of Chemistry and Biochemistry
Georgia Institute of Technology

Dr. Z. John Zhang
School of Chemistry and Biochemistry
Georgia Institute of Technology

Date Approved: June 10, 2013

There is a single light of science, and to brighten it anywhere is to brighten it everywhere.

-Isaac Asimov

Dedicated to my loving and supporting parents,
George and Donna Lydon.

Acknowledgements

I could not have completed this thesis without the many important players in my life for the past five years. Firstly, I would like to thank my two advisors: Dr. Jones and Dr. Nair. Their strengths are opposite and complementary but form a synergistic working environment and I could not have done it without either of them. I would also like to express my appreciation for the many opportunities I have been able to take advantage of due to the support of my advisors and the unique situation I was in by working in two departments.

I am grateful for the many Jones and Nair group members that have provided scientifically stimulating conversations, support, and assistance. Special thanks needs to be given to Yolande Berta and Yong Ding for their passion, time, and patience in working with me to improve my microscopy skills and bearing with me when I accidentally dumped the vacuum. I would like to thank Walter for his patience and cooperation while I tried to resurrect the art of Harmonix mode. And I would like to acknowledge Kinga Unocic at Oak Ridge National Laboratory for working with me to obtain TEM images on my particles early in my thesis research. Lastly, I am thankful for Dr. Rod Schoonover, my college chemistry teacher, who fortified my fascination in chemistry and encouraged me to progress in the field.

Graduate school requires some fun and I would like to thank our physical chemistry gang (with a few honorary physical chemists) for providing an enjoyable distraction. I would especially like to thank Song Seto, Kristen Baugh, O'Neil Smith, Anselmo Kim, Jeff Drese, Weiyin Xu, Ryan Lively, Václav Beránek, Helen Westbrook, Ariel Marshall, Jessie Whiteman, Jenna Arruda and my sister Katie Lydon. All of these

people have been vital confidants with whom I have had many terrific conversations and will miss dearly.

I would like to thank my Uncle Tom and Auntie Paula for providing me with an east coast home-away-from-home to enjoy good company, relax, and drink plenty of cappuccinos.

Lastly, and most importantly, I would like to thank my parents, George and Donna Lydon. They provided me with the yearning for knowledge that drove me to this point and provided the love, support, and encouragement to back it up.

Table of Contents

Page

Acknowledgements iv

List of Tables ix

List of Figures xi

List of Symbols and Abbreviations xviii

Summary xix

1 Chapter 1: Introduction 1

1.1 Natural Gas Separations 1
1.2 Membrane Background 3

1.2.1 Theory 3
1.2.2 Glassy Polymer Membranes 5
1.2.3 Inorganic membranes 7
1.2.4 Mixed Matrix Membranes 7

1.3 Materials for Use in MMMs 8

1.3.1 Matrimid polymer 8
1.3.2 LTA and MFI Zeolites 9
1.3.3 MMM Non-idealities 11
1.3.4 Strategies to Improve the Zeolite-Polymer Interface 12

1.4 Deposition of Mg- based Nanostructures on Zeolites 16

1.4.1 Functionalization methods 16
1.4.2 Previous Theories on Improvements to Adhesion by Nanostructuring 19

1.5 Materials Background 21

1.5.1 Zeolites 21
1.5.2 $Mg(OH)_2$ 24
1.5.3 MgO 26
1.5.4 MgO_xH_y Materials 27
1.5.5 Other Composite Materials 28

1.6 Objectives and Strategy 30

2 Chapter 2: Functionalization of LTA and MFI and analysis of the MgO_XH_Y nanostructures produced 32

2.1 Introduction 32
2.2 Experimental Methods 34

2.2.1 Materials 34
2.2.2 Synthesis of Zeolite LTA and MFI Particles 35
2.2.3 Surface Modification Techniques 35
2.2.4 Characterization 37

2.3 Results and Discussion 40

2.3.1 Surface Nanostructures on Zeolite LTA 40
2.3.2 Surface Nanostructures on Pure-silica Zeolite MFI 55

2.4 Conclusions 62

3 Chapter 3: Morphological, mechanical, and natural gas separation properties of polyimide-based nanocomposite membranes containing functionalized LTA 65

3.1 Introduction 65
3.2 Methodology 66

3.2.1 Membrane Fabrication 66
3.2.2 Dynamic Light Scattering 67
3.2.3 Membrane Imaging 67
3.2.4 Dispersion 68
3.2.5 Mechanical Properties 71
3.2.6 Gas Permeation Measurements 75

3.3 Results and Discussion 77

3.3.1 Solvent choice 77
3.3.2 Membrane imaging 78
3.3.3 Assessment of Composite Membrane Dispersion 81
3.3.4 Membrane Mechanical Properties 82
3.3.5 CO_2/CH_4 Gas Permeation Measurements 91

3.4 Conclusions 95

4 Chapter 4: Characterization of the Zeolite/Polymer Interface in LTA/Polyimide MMMs 96

4.1 Introduction 96
4.2 Chemistry at Oxide-Poly(imide) Interfaces 97

4.2.1 Mechanisms of Adhesion 97
4.2.2 Zeolite-Polymer Interface 100
4.2.3 MgO_xH_y-Polymer Interface 103
4.3 Analysis of Interfacial Polymer Properties Using NMR 105
4.3.1 NMR Theory 105
4.3.2 Spin-Spin Relaxation 105
4.3.3 Methods and Results 113
4.3.4 Discussion 123
4.4 Mechanical properties 130
4.4.1 Theory 130
4.4.2 Experimental methods 132
4.4.3 Results 132
4.5 Conclusions 135

5 Conclusions and Future Work 137
5.1 Summary 137
5.2 Conclusions 137
5.3 Future Work 140
5.3.1 Solvothermal Functionalization Mechanism and the Impact of Specific Surface Structures 140
5.3.2 Assessment of Strength in Each Joint of the Interfacial Region 141

Appendix A 143
Appendix B 145
References 158
Vita 173

List of Tables

Table 1-1. Quality standards for natural gas pipelines [1,3,4] 2

Table 1-2. Characteristics of gases.[10] 5

Table 1-3. Gas separation properties of methane and carbon dioxide in zeolite materials. 11

Table 2-1. MgO and $Mg(OH)_2$ properties 49

Table 2-2. Atom % values of Ca-exchanged LTA and modified-LTA samples measured EA, EDS, and XPS and normalized to Si value to be compared across methods. XPS values are for Na-exchanged samples.[84] 50

Table 2-3. Surface area and micropore volume of LTA and modified-LTA materials, obtained from nitrogen physisorption isotherms and expressed per gram of Si. These values can be converted to cm^2/g zeolite *via* a conversion factor of ~6.15 g zeolite/g Si. [84] 53

Table 2-4. Elemental composition of bare and functionalized MFI samples by EDS and XPS. [84] 59

Table 2-5. Surface area and micropore volume of MFI and modified-MFI materials, obtained from nitrogen physisorption isotherms and expressed per gram of Si. These values can be converted to cm^2/g zeolite *via* a conversion factor of 2.14 g zeolite/g Si. [84] 60

Table 2-6. T-plot porosity and surface area of LTA functionalized with the modified solvothermal method with and without Mg. 61

Table 2-7. T-plot porosity and surface area of MFI functionalized with the modified solvothermal method with and without Mg. 61

Table 2-8. Summary of properties of surface nanostructures produced by four different surface modification methods on LTA. *All scale bars represent 100 nm except bare LTA which is 500. [84] 63

Table 2-9. Summary of properties of surface nanostructures produced by three different surface modification methods on MFI. [84] 64

Table 3-1. Size and polydispersity (PdI) for zeolite/solvent solutions (particle only) and zeolite/polymer/solvent solutions (Matrimid)..... 78

Table 3-2. Free space length of the composite LTA/Matrimid® membranes. 82

Table 4-1. Isoelectric points of various mineral oxide materials. [125,131,132] 104

Table 4-2. Spin properties of ^{1}H atom.[136]..... 105

Table 4-3. The activation energies (ΔE^*) of the two fitted regions in each membrane material. 122

Table A-1. Elemental composition weight % of Ca-exchanged samples normalized to Si by EA, EDX, and XPS. *XPS values are for Na-exchanged samples..... 143

Table B-2. Relaxation times of the polymer and composite materials measured by NMR. 151

List of Figures

Figure 1-1. Diagram of membrane operation.[10] 3

Figure 1-2. A) Illustration of the upper bound tradeoff between permeability and selectivity in CO_2/CH_4 separation membranes by Robeson.[15] B) A revised version of the upper bound including recent developments. [16] 6

Figure 1-3. Structure of Matrimid® polymer. 8

Figure 1-4. LTA framework viewed along the [100] direction.[24] 10

Figure 1-5. MFI framework viewed along the [010] direction.[24] 10

Figure 1-6. Gas permeation path when a void space is present in the MMM. 12

Figure 1-7. Illustration of A) condensation reaction between silanol and zeolite surface and B) reaction of polyimide with silane functionalized surface to connect the zeolite and bulk phase polymer. Figure modified from Mahajan et al.[19] 14

Figure 1-8. Cartoon of the nanoscale gap between the bulk polymer and zeolite with the use of silane crosslinkers. [19] 14

Figure 1-9. Illustration of dense polymer layer formed when zeolites are crosslinked to the polymer phase.[29] 15

Figure 1-10. Illustration of how functionalization improves membrane gas separation properties 16

Figure 1-11. Synthesis of nanostructures for A) Grignard, B) solvothermal, C) modified solvothermal, and D) ion exchange functionalization methods. [84] 17

Figure 1-12. Cartoon of polymer attachment to nanostructured zeolites and the entropically-costly deformation required for this attachment.[26] 20

Figure 1-13. Illustration of the additional points of contact in a functionalized zeolite compared to bare zeolite.[26] 20

Figure 1-14. Crystal growth mechanism of LTA.[43] 22

Figure 1-15. Crystal growth mechanism of TPA-MFI.[42] 23

Figure 1-16. $Mg(OH)_2$, or brucite, unit cell and structure.[51] 25

Figure 1-17. Illustration of chlorophyll-α-water-chlorophyll- α interaction. [38] 26

Figure 1-18. MgO, or periclase, unit cell and structure.[51] 27

Figure 1-19. Examples of possible intermediate MgO_xH_y species between $Mg(OH)_2$ and MgO. The light gray represents magnesium, dark gray-oxygen, and white-hydrogen. The u value is the degree of dehydroxylation.[54] 27

Figure 1-20. Free energy (dark grey), enthalpy (light gray), and bulk moduli (black) for MgO, $Mg(OH)_2$, and the stoichiometric intermediates. In the structure shown, the light gray represents magnesium, dark gray-oxygen, and white-hydrogen. The u value is the degree of dehydroxylation. [46]..... 28

Figure 2-1. X-ray diffraction patterns of (a) unmodified 300 nm LTA particles, and after modification by (b) Grignard, (c) solvothermal, (d) modified solvothermal, and (e) ion exchange methods. The reference peak positions of LTA [83]. The arrow indicates the XRD peak corresponding to crystalline MgO_xH_y structures such as $Mg(OH)_2$ or MgO.[84] 41

Figure 2-2. Low-magnification TEM images of 300 nm LTA particles modified by A) Grignard, B) Solvothermal, C) Modified solvothermal, and D) Ion exchange functionalization methods. [84] 42

Figure 2-3. TEM image showing existence of secondary phase produced by Solvothermal functionalization of LTA. [84] 43

Figure 2-4. SEM images of LTA particles surface-modified by (a) Grignard, (b) Solvothermal, (c) Modified Solvothermal, and (d) Ion Exchange. [84]..... 43

Figure 2-5. Intermediate-resolution transmission electron micrographs of nanostructures produced by a) Grignard, b) solvothermal, c) modified solvothermal, and d) ion exchange methods. The yellow line demarcates the border between zeolite and nanostructures. [84] 45

Figure 2-6. HRTEM images of A) Grignard, B) solvothermal, and C) modified solvothermal functionalized LTA and the Fourier transform of the functionalization highlighted by the white rectangle. The text is the corresponding d-spacing for each observable point. The yellow line demarcates the border between zeolite and nanostructures. [84]..... 46

Figure 2-7. (A) HRTEM of Solvothermal functionalized LTA showing layered material (B) Fourier transform of functionalization generated from rectangle on the left image. The text is the corresponding d-spacing for each observable point. [84] 47

Figure 2-8. TEM images showing example of an ion exchange functionalization penetrating into the zeolite. [84] 48

Figure 2-9. EDS mapping and line profiles in STEM mode of the edge of ion exchange functionalized LTA. All measurements represent the K-edge energy. 52

Figure 2-10. Nitrogen adsorption isotherms for 300 nm Ca-exchanged the four functionalized LTA particles; all normalized to the Si content obtained from elemental analysis. These values can be converted to cm^2/g zeolite *via* a conversion factor of ~6.15 g zeolite/g Si. [84] 54

Figure 2-11. X-ray diffraction patterns of (A) unmodified 300 nm MFI particles, and after modification by (B) Grignard, (C) solvothermal, and (D) modified solvothermal methods. [84] 56

Figure 2-12. Scanning electron microscopy images of (A) Grignard, (B) Solvothermal, and (C) Modified solvothermal functionalized MFI. [84] 57

Figure 2-13. TEM images of (A) Grignard, (B) Solvothermal, and (C) Modified-solvothermal functionalized MFI; and (D) HRTEM of Grignard nanostructure on MFI with Fourier transform (inset) of the area in the white rectangle. The corresponding *d*-spacings are shown for each observable point in the Fourier transform. [84] 58

Figure 2-14. Nitrogen physisorption isotherms of bare and functionalized MFI normalized to the weight% of Si by EDX. These values can be converted to cm^2/g zeolite *via* a conversion factor of 2.14 g zeolite/g Si. [84] 60

Figure 3-1. Process of marking particle location on the composite membranes. 69

Figure 3-2. Illustration of the particle distribution histograms produced during each step of the Khare and Burris method.[94] The bottom histogram represents the final L_f size with a mode of 0. 70

Figure 3-3. An illustration of L_f values (sizes) for several different levels of distribution/ agglomeration.[94] 70

Figure 3-4. Scanning probe microscopy images of the surface roughness before polishing (top row) and after polishing (bottom row) of composite membranes fabricated with A) no filler, B) bare LTA, and LTA functionalized with the C) ion exchange, D) modified solvothermal, E) original solvothermal, and F) grignard methods. 72

Figure 3-5. Diagram of parameters during a nanoindentation experiment.[97] 73

Figure 3-6. Anatomy of a nanoindentation measurement and illustration of important parameters of the Oliver and Pharr method. 74

Figure 3-7. A) Loading function on nanoindentation measurement and B) spatial arrangement of indentation points per data set. 75

Figure 3-8. Gas permeation measurement through a Matrimid-LTA composite membrane. The 'breakthrough time' is highlighted by the purple dashed lines. 76

Figure 3-9. SEM images of membranes made with pure polymer, bare LTA, and LTA functionalized with four different methods at 15 and 30 wt.% loadings. Scale bars represent 1 μm. 79

Figure 3-10. High (left panel) and low (right panel) magnification TEM images of composite membranes made with functionalized nanoparticles. 80

Figure 3-11. Example nanoindentation measurement force vs. depth curve for A) pure Matrimid® polymer and Matrimid® mixed matrix membranes with B) bare LTA, C) ion exchange D) modified solvothermal, E) original solvothermal, and F) Grignard functionalized LTA. 83

Figure 3-12. The reduced elastic modulus determined by nanoindentation for membranes with (A) 15 wt.% and (B) 30 wt.% zeolite loading. The divided box represents the 25^{th}, 50^{th}, and 75^{th} percentile values, the whiskers represent the statistical outliers, the X represents the maximum and minimum values in the data set, and the square represents the average value. 85

Figure 3-13. The measured average elastic moduli versus predicted Voigt and Reuss bounds. 86

Figure 3-14. Hardness determined by nanoindentation for A) 15 w/w% loading and B) 30 w/w% loading membranes. The divided box represents the 25^{th}, 50^{th}, and 75^{th} percentile values, the whiskers represent the statistical outliers, the X represents the maximum and minimum values in the data set, and the square represents the average value. 89

Figure 3-15. (A) Free space length versus elastic modulus, and (B) free space length versus hardness. 90

Figure 3-16. Gas permeation properties of 15 wt.% membranes and 30 wt.% zeolite loaded membranes. [84] 92

Figure 3-17. (A) Elastic modulus versus CO_2 permeability and CO_2/CH_4 selectivity and (B) Hardness versus CO_2 permeability and CO_2/CH_4 selectivity. 93

Figure 3-18. (A) Free space length versus CO_2 permeability and (B) Free space length versus CO_2/CH_4 selectivity. The pure polymer value is represented by the dashed line.. 94

Figure 4-1. Bronsted acid sites in aluminosilicates (II), silicate (III), and aluminate (IV) materials.[128] 101

Figure 4-2. Schematic of surface bound polyimide as the "weak boundary layer" and the bulk polyimide as a method of attachment between the two phases.[123,125]..... 102

Figure 4-3. Comparison of the ^1H NMR spectral motions in the frequency and time domains.[168] 106

Figure 4-4. Cartoon of the pulse sequence, timing, and echo response of the Hahn spin-echo experiment where δ_1 represents the slower and δ_2 the faster spin.[144] 108

Figure 4-5. Diagram of possible mobile molecular parts of a crosslinked polymer system where: 1) inter-crosslink chains, 2) dangling chain ends, and 3) sol molecules. [138].. 110

Figure 4-6. Illustrations of bound, interfacial, and mobile polymer segments in a rubbery composite material.[137,150] 111

Figure 4-7. Figure of the type of crystalline domains in a crystalline polymer material.[153,154]..... 113

Figure 4-8. ^1H NMR spectra of Matrimid at increasing temperatures and cooling. 114

Figure 4-9. ^1H spectra at different τ times of a pure Matrimid membrane for calculating relaxation curves. 116

Figure 4-10. T_2 relaxation curve for Matrimid, bare LTA MMM, $Mg(OH)_2$ MMM, and pure $Mg(OH)_2$. The arrow indicates a unique inflection point present only in Mg-containing samples. 117

Figure 4-11. T_2 relaxation curve for MMMs made with ion exchange, modified solvothermal, original solvothermal, and Grignard functionalized LTA. The arrow indicates a unique inflection point present only in Mg- containing samples..... 118

Figure 4-12. Spin-spin relaxation curve for all MMMs at 190°C. A) Full dataset B) emphasis on the early relaxation behavior. 119

Figure 4-13. The fitted T_{2-1} and T_{2-2} relaxation times for all membranes at the four temperatures. The solid lines/markers correspond to T_{2-1} and dashed lines/open markers correspond to $T_{2-2.}$ 120

Figure 4-14. The ratio of T_{2-1}/T_{2-2} components determined by A_1 and A_2 in equation (4.7) for all membranes at the four temperatures. These values represent the rigid/ intermediate portion. 121

Figure 4-15. Arrhenius plot of T_2 relaxation data. 122

Figure 4-16. Schematic of Matrimid polymer's electron donating and withdrawing groups forming inter- and intra-molecular charge transfer complexes.[155] 123

Figure 4-17. Illustration of three domains present in pure glassy polymer system. The glassy region is the ordered section of the polymer between the two lines, while the intermediate region consists of the polymers outside the dashed lines. 124

Figure 4-18. Illustration of the types of local polymer environments in a functionalized zeolite MMM system. (R) is the rigid, oriented, noncrystalline polymer domain and (I) is an intermediate domain where the polymer has one point of restraint (p.o.r.). 127

Figure 4-19. HarmoniX cantilever with an offset tip location. [160] 131

Figure 4-20. log (Modulus) of cross sections of a bare LTA MMM (A) and B)ion exchange, C) modified solvothermal, D) original solvothermal, and E) Grignard functionalized LTA MMMs. 133

Figure 4-21. Height of cross sections of a bare LTA MMM (A) and B)ion exchange, C) modified solvothermal, D) original solvothermal, and E) Grignard functionalized LTA MMMs. 133

Figure A-1. XPS raw data of (a) unmodified 300 nm LTA particles, and after modification by (b) Grignard, (c) solvothermal, (d) modified solvothermal, and (e) ion exchange methods. 144

Figure A-2. XPS raw data of (a) unmodified 300 nm MFI particles, and after modification by (b) Grignard, (c) solvothermal, and (d) modified solvothermal methods. 144

Figure B-3. Matrimid ^{1}H NMR spectra at increasing temperatures 145

Figure B-4. Bare LTA/Matrimid MMM ^{1}H NMR spectra at increasing temperatures . 146

Figure B-5. Ion exchange modified LTA/Matrimid MMM ^{1}H NMR spectra at increasing temperatures 147

Figure B-6. Modified solvothermal modified LTA/Matrimid MMM ^{1}H NMR spectra at increasing temperatures 148

Figure B-7. Original solvothermal modified LTA/Matrimid MMM ^{1}H NMR spectra at increasing temperatures 149

Figure B-8. Original solvothermal modified LTA/Matrimid MMM ^{1}H NMR spectra at increasing temperatures 150

Figure B-9. T_2 relaxation curve for pure, solid zeolite LTA..... 152

Figure B-10. ^{13}C CP-MAS spectra of Matrimid with a spinning frequency of 11kHz and contact time of 1.0 ms. Peak assignments are based off the work by Grobelny et al.[169] 152

Figure B-11. Atomic force microscopy images of topography and material properties using HarmoniX mode of a cross section of LTA in Matrimid..... 153

Figure B-12. Atomic force microscopy images of topography and material properties using HarmoniX mode of a cross section of ion exchange functionalized LTA in Matrimid 154

Figure B-13. Atomic force microscopy images of topography and material properties using HarmoniX mode of a cross section of modified solvothermal functionalized LTA in Matrimid 155

Figure B-14. Atomic force microscopy images of topography and material properties using HarmoniX mode of a cross section of original solvothermal functionalized LTA in Matrimid 156

Figure B-15. Atomic force microscopy images of topography and material properties using HarmoniX mode of a cross section of grignard functionalized LTA in Matrimid 157

List of Abbreviations

AFM – atomic force microscopy
BET –Braunaer-Emmet-Teller
DCM – dichloromethane
DETA – diethylenetriamine
DI – deionized water
DLS – dynamic light scattering
ΔE^* – activation energy
ED – electron diffraction
EDA – ethylenediamine
EDS – energy dispersive x-ray spectroscopy
en – ethylenediamine (in ligand form)
FID – free induction decay
ICP-AES – inductively coupled plasma atomic emission spectroscopy
HRTEM – high resolution transmission electron microscopy
LTA – zeolite 4A
MMM – mixed matrix membrane
NMR – nuclear magnetic resonance
PdI – polydispersity index
SDA – structure directing agent
SEM – scanning electron microscopy
SPM – scanning probe microscopy
STEM – scanning transmission electron microscopy
τ – decay time
T_2 – spin-spin relaxation time
τ_c – correlation time
TE – echo time
TEM – transmission electron microscopy
THF – tetrahydrofuran
VDW – Van der Waals forces
XPS – X-ray photoelectron spectroscopy
XRD – X-ray diffraction

Summary

Mixed matrix membranes (MMMs) are an ideal membrane technology for gas separations because they are able to combine the advantages of inorganic and polymeric membranes while mitigating the disadvantages. However, one of the main problems with these membranes are their interfacial compatibility issues. These issues will be addressed at length in this thesis.

Chapter 1 is an introduction to the background of why MMMs are used, previous work in the field, and the motivation for zeolite surface functionalization. Additionally, the surface functionalization methods and the materials used in this work will be explained. Chapter 2 focuses on a detailed characterization of the nanostructures produced by each functionalization method. This work includes the elemental composition, morphology, crystallinity, porosity and surface area and how each of these properties may affect performance in MMM applications. Chapter 3 addresses MMMs fabricated with the functionalized zeolites. The membranes' quality is assessed by characterizing their dispersion, mechanical properties, and CO_2/CH_4 gas separation properties. These membrane properties are then correlated to the nanostructure properties and predicted performance from Chapter 2. Chapter 4 studies the interfacial region between the two phases in a MMM by studying the mobility and local mechanical properties of the polymer. This work resolves changes in the polymer structure that occur due to the added filler and theories about the specific bonding mechanisms are proposed. Chapter 5 suggests future work in addition to a summary of conclusions and results.

1 Chapter 1: Introduction

1.1 Natural Gas Separations

Natural gas is an important fuel and a key feedstock for the chemical industry.[1] It is also becoming increasingly important because of its environmental advantage of releasing 30-45% less CO_2 per unit thermal energy, and a minimal amount of sulfur,[2] compared to other fossil fuels such as coal and oil. It has especially gained interest in the United States over the past half century with the discovery of many new natural gas reserves, improvements in fracturing technology that are able to obtain difficult to recover resources, and an interest in energy independence for national security purposes.[2] U.S. consumption of natural gas occurs at a rate of 22 trillion cubic feet per year and it is estimated that there is enough gas immediately available in the lower 48 states to last approximately another 50-60 years in addition to new resources that have not yet been tapped.[1,2]

Natural gas composition varies widely depending on the well it came from, and is influenced by many factors including the geography and method of extraction.[1] Once natural gas is removed from the well, it must be transported in pipelines and the pipeline infrastructure has specific quality standards for consumer protection and to minimize infrastructure damage and extend its lifetime.[1,3] The standards and the typical composition of as-extracted natural gas are shown in **Table 1-1** and from a comparison of these values, it is apparent that natural gas often needs additional processing before being transported.[1,3,4] Specifically, the work described in this thesis focuses on the separation of carbon dioxide from the methane (sour gas sweetening), as it is an

Table 1-1. Quality standards for natural gas pipelines [1,3,4]

Component	Specification	Typical composition of natural gas
CO_2	<2%	0-8%
Higher carbons: Ethane, propane, and butane		0-20%
H_2S	<4 ppm	0-5%
Inert Gases (N_2, He)	<4%	0-5%

acidic gas that causes corrosion in pipelines.[5]

CO_2/CH_4 natural gas separations are conventionally done using costly, infrastructure-heavy, thermally driven methods such as cryogenic distillation, absorption in liquids (typically amines), or adsorption on solid materials.[2,5–7] The large capital costs of these methods is especially problematic for the purification of gas from smaller point sources and they are often left untapped because of the burdensome treatment costs.[8] An alternate approach to gas separation is via application of cellulose acetate or poly(imide) membranes that offer lower energy and capital costs compared to the traditional methods.[6,9] Membranes for CO_2/CH_4 separations were actually one of the first patented membranes for gas separations in industry.[10] Membranes are an especially attractive technology for use in industry because they allow an instantaneous response to changes in process conditions, a rapid start-up time, a modular method of expansion, greater reliability, and a lower energy requirement.[8,11]

1.2 Membrane Background

1.2.1 Theory

Membrane separation systems operate by preferentially transferring one component of the feed stream across the membrane. This creates a permeate stream that is enriched in the favored gas penetrant and a retentate stream that has a much lower concentration of that penetrant, as shown in **Figure 1-1**.[10]

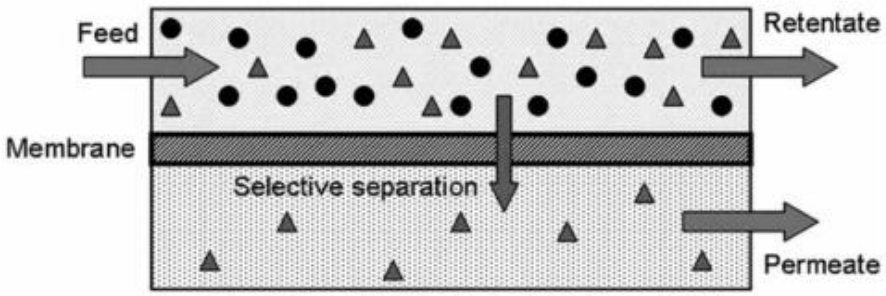

Figure 1-1. Diagram of membrane operation.[10]

Membranes for gas separation are typically formed from polymeric materials that operate through the solution-diffusion mechanism, or inorganic materials that work through molecular sieving or Knudsen mechanisms.[10] In polymers, the gas permeability (P) follows the solution-diffusion mechanism and is related to the interaction between the gas species and the polymer.[10] This interaction can be expressed as **equation (1.2)**:

$$P = D \times S \qquad (1.1)$$

where diffusivity (D), the kinetic factor, represents the average diffusivity of the gas molecule- a complex function that can have 12 or more unique diffusivity terms

depending on the membrane material.[12] The solubility (S), the thermodynamic factor, is related to the membrane's ability to adsorb and desorb the penetrant gas molecule and is dependent on the composition and functional groups of the membrane material. The membrane's permeability represents the overall rate of gas transport and is an indicator of a membrane's productivity.

The selectivity of a gas separation membrane is another key descriptor. It describes selectivity for one penetrant (A) compared to another (B) as shown in **equation (1.2)**:

$$\alpha_{AB} = \frac{P_A}{P_B} \tag{1.2}$$

where P_A is the permeability of penetrant A and P_B is the permeability of penetrant B. Typically the faster penetrant is in the numerator of the selectivity equation. To achieve the best separation, it is desirable to have the fastest throughput and the highest purity as achieved by having a higher permeability and selectivity, respectively.[7,8]

Molecular sieving in inorganic materials takes advantage of their rigid structure and defined pore size to size exclude one gas from going through the membrane. For example, in the case of CO_2/CH_4 separations, the two gases possess different kinetic diameters listed in **Table 1-2**. Zeolite DDR with a pore size of 3.65 Å is the most ideal for this separation because its pore diameter is between the kinetic diameters of the two gases and will allow passage of the CO_2 while blocking the CH_4. Knudsen diffusion occurs in

Table 1-2. Characteristics of gases.[10]

Molecule	Molecular weight	Kinetic diameter
CO_2	44	3.3
CH_4	16	3.8

spaces where the gap is on the order of the gas mean free path and might occur in cracks or large pores or channels. The movement of gas through this void is impacted by collisions between the gas and the channel walls and is inversely proportional to the molecular weight of the gas.[10]

1.2.2 Glassy Polymer Membranes

Glassy polymers are polymers with a glass transition temperature (T_g) above room temperature. Typically they show minimal polymer chain motion and polymer chain rearrangement occurs on a very long time scale.[7,10,13] This generally results in an excess in free volume due to imperfect packing (and slow rearrangement) of polymer chains.[10] Glassy polymers are more ideal for gas permeation than rubbery polymers (that lack the free volume) because the additional void spaces have the potential to increase adsorption interactions between the gas and membrane and, thus, the solubility component of the permeability.[10,12] For example, hexafluorodianhydride (6FDA)-based polymers are excellent candidates for gas separations because their bulky $–C(CF_3)_2$ groups reduce polymer mobility and density of chain packing, allowing more free volume for improved permeability.[7] Cellulose acetate and poly(sulfone) membranes are also commonly used membranes for gas separations; however, poly(imide)s show better

selectivity properties and recent investigations have increasingly focused on these materials.[10,14]

Polymer membranes have advantages for use in industrial applications because they are easier to process, more flexible, and lower cost than inorganic membranes.[5] However, despite the improvement in selectivity by poly(imide) materials, polymer membranes still have disadvantages that impact their use in actual industrial applications. The major disadvantage of polymer membranes is the 'upper bound' tradeoff. Robeson showed that polymer membranes that have a high CO_2 permeability have a lower CO_2/CH_4 selectivity and vice versa.[15] The upper bound is the limit polymers have not been able to cross into in order to provide a high permeability and selectivity membrane. **Figure 1-2-A** shows the initially declared upper bound and clearly illustrates the difference in properties between glassy and rubbery polymers as mentioned before. A new upper bound was introduced in 2008 (**Figure 1-2-B**) with the inclusion of new polymer materials, including thermally rearranged polymers.[16]

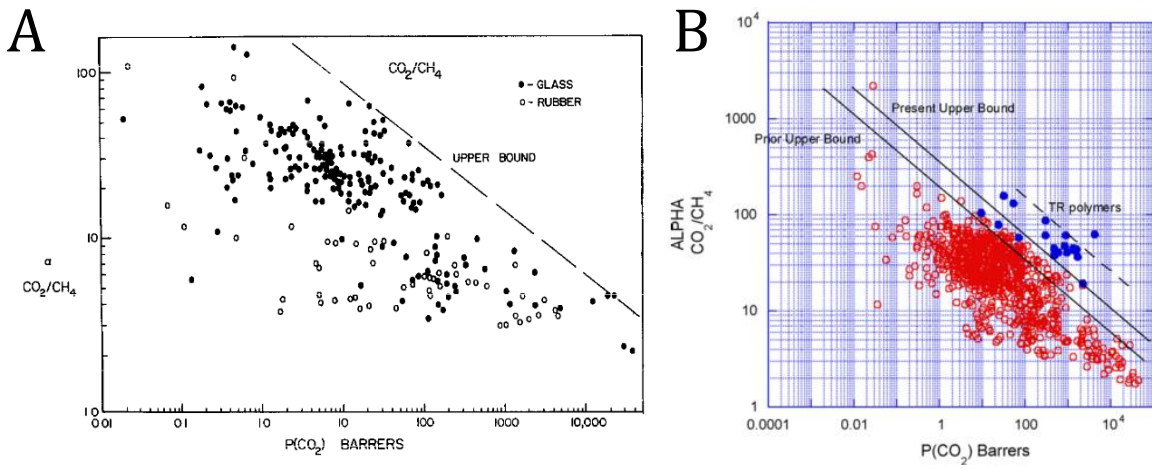

Figure 1-2. A) Illustration of the upper bound tradeoff between permeability and selectivity in CO_2/CH_4 separation membranes by Robeson.[15] B) A revised version of the upper bound including recent developments. [16]

1.2.3 Inorganic membranes

Inorganic materials, especially those with molecular sieving capabilities, offer a potentially excellent membrane for gas separations that far exceeds the selectivity of polymer membranes. Additionally, inorganic membranes can have a longer lifespan and are tolerant of higher temperatures and harsher operating conditions.[8,17] However, inorganic membranes have several shortcomings that have prevented them from being commonly used for gas separations in industry. The most significant is their brittleness and difficulty to scale to industrially relevant sizes.[6,8,17] When inorganic membranes are scaled up, they often develop cracks either during synthesis or handling and even a minor crack in the membrane can void the molecular sieving capabilities of the material. Inorganic membranes are also more expensive in terms of both the membrane materials and the capital and repair costs necessary to utilize the membranes in separations.[8,17]

1.2.4 Mixed Matrix Membranes

Although polymeric membranes have formed the mainstay of industrial membrane applications, polymer/inorganic composite membranes are emerging as a higher-performance alternative.[6] Specifically, mixed matrix membranes (MMMs) are composite membranes containing a polymer bulk phase and a dispersed inorganic selective phase. These composite membranes incorporate the selectivity of inorganic membranes and the ability to go beyond the upper bound of purely polymer materials while also maintaining the processability and affordability of polymer membranes.[6,12,18–22] In addition to adding a dispersed, size discriminating component, MMMs also increase the selectivity of the membrane by causing the methane (the larger gas in sour gas separations) to travel a more tortuous path around the selective

filler (often a zeolite as will be described later in the chapter), thereby decreasing its rate of permeation and increasing the membrane selectivity for carbon dioxide.[6] Addition of the filler also has the potential to disrupt polymer chains thereby creating a greater free volume in glassy polymers and subsequently increasing the permeability of gases through the membrane.[8]

1.3 Materials for Use in MMMs

1.3.1 Matrimid polymer

The MMMs in this work are made from the polymer Matrimid® and the filler materials zeolites LTA and MFI. Matrimid®, 3,3'-4, 4'-benzophenone tetracarboxylic-dianhydride diaminophenylindane, is a glassy poly(imide) originally developed for use in microelectronics with the structure shown in **Figure 1-3.** [14] However, more recently it has been proven an excellent candidate for gas separations because it has separation properties near the upper bound, it is commercially available, and it can be fabricated in the industrially relevant format of an asymmetric hollow fiber membrane.[5]

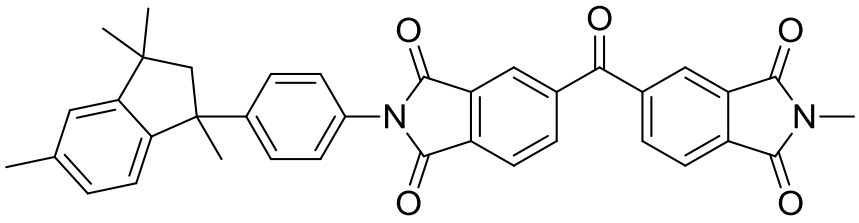

Figure 1-3. Structure of Matrimid® polymer.

1.3.2 LTA and MFI Zeolites

LTA and MFI are both members of the zeolite class of inorganic materials. Zeolites are classified as aluminosilicate crystalline materials composed of TO_4 tetrahedra (where T= Si or Al) and have microporous channels throughout the crystal.[23] LTA (also called zeolite 4A) is an aluminosilicate zeolite with an aluminum to silicon ratio of 1:1, a pore size of 4.1Å, and a three dimensional pore structure as shown in **Figure 1-4.**[24] LTA is particularly interesting because the alumina inserted into the framework causes the zeolite to be negatively charged and balance the charge at the aluminum sites in the framework with a Na^+ cation. The cation also allows for tuning of the zeolite pore size to fit the desired separation by exchanging the cation from Na (4Å, LTA 4A) to K (3Å, LTA 3A) or Ca (5Å, LTA 5A) where the accessible pore size in the zeolite after the exchange and the name of the corresponding zeolite are in parenthesis. The MFI framework is shown in **Figure 1-5** and can have a silicon to aluminum ratio of 3.5-∞.[24] The specific MFI composition used in this work is called pure silica MFI and it has an infinite[1] ratio of silicon to aluminum, a discriminating pore size of 5.5 Å, and a neutral charge.[24,25] The pore size of MFI is too large for molecular sieving of CO_2/CH_4 but was chosen because its surface functionalization, properties, and synthesis methods have been widely studied and are well known. LTA is also a commonly used and well-understood aluminosilicate zeolite structure. The permeability and ideal selectivity for CO_2 and CH_4 in the zeolites used in this work are listed in **Table 1-3**. The

[1] Aluminum may be present in the framework as a trace impurity from the silicon source but is minimal.

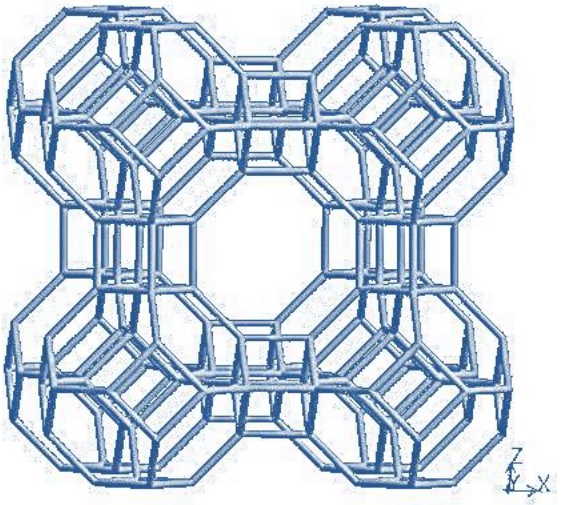

Figure 1-4. LTA framework viewed along the [100] direction.[24]

pore size of LTA is very close to the kinetic diameter of methane, which means that diffusion of methane through the structure will be very slow. Hence, the ideal selectivity of LTA 4A is well above the Robeson upper bound.

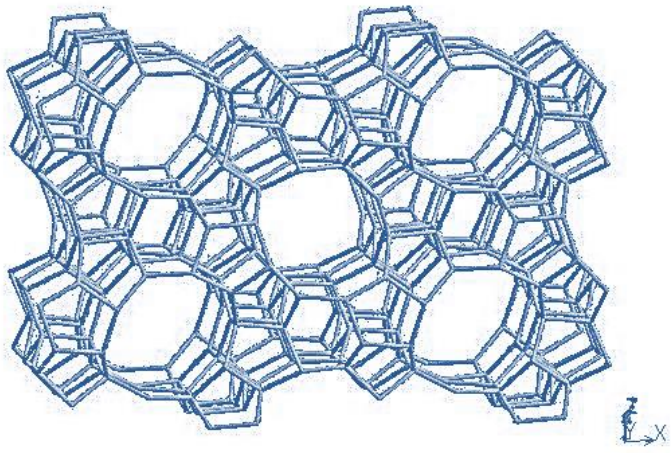

Figure 1-5. MFI framework viewed along the [010] direction.[24]

Table 1-3. Gas separation properties of methane and carbon dioxide in zeolite materials.

	CH_4 Permeability (Barrers)	**CO_2 Permeability (Barrers)**	**Ideal Selectivity**
Pure Silica MFI [165,166]	$1.1x10^{4}$	$3.4x10^{3}$	3.24
LTA (4A) [167]	$4.4x10^{-2}$	$1.5\ x10^{1}$	340

1.3.3 MMM Non-idealities

A critical design issue in the fabrication of MMMs is control over the polymer/inorganic interfaces, which often determines the overall membrane performance.[18] Typically, in rubbery or hydrophilic polymers such as poly(vinyl acetate) the interface between the zeolite and polymer is an ideal transition.[5,26] However, as mentioned previously, these polymers may not have the best properties for gas separations. When glassy polymers are used in MMMs, a void or defect often occurs between the polymer and filler phase caused by incompatibility between the two phases. [27,28] Zeolites are typically hydrophilic and do not adhere strongly to hydrophobic poly(imide)s.[18] This lack of compatibility is compounded when the glassy poly(imide) sets into its final form after casting but before all of the solvent is removed. In this case, the minimal chain mobility of the poly(imide)s that enables better gas separation prevents the polymer from rearranging during solvent removal, the polymer contracts and pulls away from the zeolite during the solvent removal process, and the interactions between the two phases are not strong enough to keep them adhered, resulting in a void space.[5,8,18] These voids are especially detrimental to gas separation applications because the voids provide fast, non-selective gas permeation pathways that allow the gas

penetrants to bypass the more selective zeolite as illustrated in **Figure 1-6**. This contributes to a decrease in membrane performance compared to what would be expected and needs to be addressed to improve the performance of MMMs.[8,18,20,21,27–30]

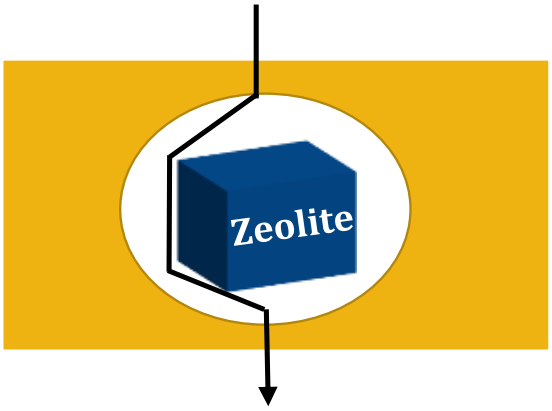

Figure 1-6. Gas permeation path when a void space is present in the MMM.

1.3.4 Strategies to Improve the Zeolite-Polymer Interface

Several strategies have been employed to control the interface between the two phases. These include changing the bulk polymer properties by using surface initiated in-situ polymerization[31,32] or addition of plasticizer to allow the polymer to conform better to the filler material during casting. [8] These modifications typically resulted in better MMMs with respect to the improved interfaces, but they limited the MMM system to specific polymers that were able to be processed through these methods, or decreased the intrinsic gas separation properties of the membrane. MMMs have also been prepared above the glass transition temperature of the polymer. These MMMs also resulted in a better interface between the two phases and improvement in gas transport properties; however, this method of fabrication is quite cumbersome, limited to solvents with a high boiling point, and is impractical for industrial use.[18] Additionally, simply using a

polymer with better gas separation properties does not always result in a better MMM. For example, Mahajan et al. used the polymer, poly[2,2'-bis(3,4-dicarboxyphenyl) hexafluoropropane dianhydride-4,4'-hexafluoro-isopropyl-idene dianiline/2,3,4,5-tetra methyl-1,4-phenylene diamine/3,5-diaminobenzoic acid)], or 6FDA-6FpDA/4MPD/ DABA, for O_2/N_2 gas separations. This polymer had an O_2 permeability of 22 barrers and selectivity of 4.2 compared to the traditionally used polymer Ultem (0.4 Barrers, 7.8 selectivity) – a significant permeability enhancement.[18] However, upon addition of zeolites, the Ultem MMM showed an improvement in selectivity by 5 for 30% weight loading and a constant permeability while the 6FDA-6FpDA/4MPD/DABA MMM selectivity remained constant and the permeability decreased compared to the original polymer.[18] This example shows that matching the intrinsic gas permeation properties of each phase is also important to the design of successful MMMs.

There has also been work to improve the zeolite-polymer interaction by using silane linkers to covalently link the zeolite to the polymer.[8,18,33] The silane, such as aminopropyltriethoxysilane (APTES) or 3-aminopropyltrimethoxysilane (APTMS), is reacted with surface silanol groups on the zeolite through a condensation reaction as shown in **Figure 1-7-A**.[8,18,33] This modification serves two functions: 1) it makes the zeolite surface more organophilic and 2) the newly attached organic moiety can be used to crosslink with the polymer as illustrated in **Figure 1-7-B**.[19] Covalent attachment between the two phases led to MMMs that appeared to have good adhesion via SEM images. However, they exhibited poor, or less than ideal, improvement in gas permeation properties depending on the processing conditions of the MMM fabrication. When a Matrimid MMM was cast at room temperature with silylated zeolites, the resulting

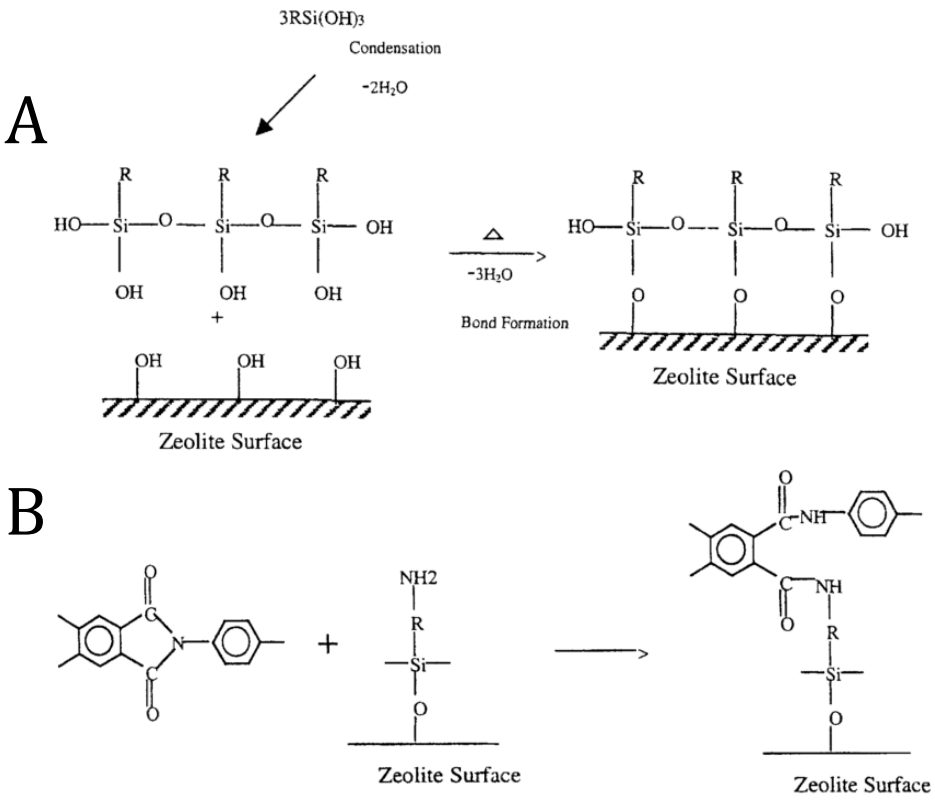

Figure 1-7. Illustration of A) condensation reaction between silanol and zeolite surface and B) reaction of polyimide with silane functionalized surface to connect the zeolite and bulk phase polymer. Figure modified from Mahajan et al.[19]

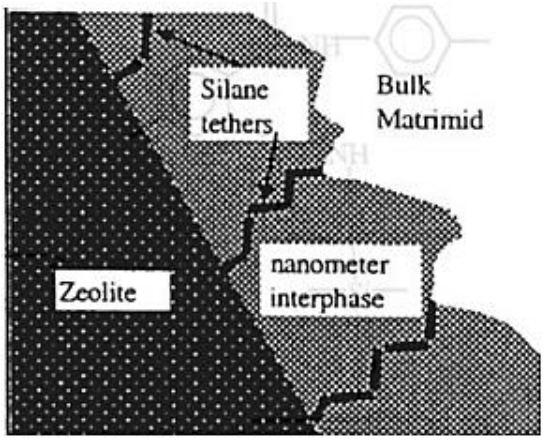

Figure 1-8. Cartoon of the nanoscale gap between the bulk polymer and zeolite with the use of silane crosslinkers. [19]

membrane showed a decrease in selectivity and no change in permeability compared to the pure polymer membrane.[19] In this case, it was proposed that silylation decreased the gap between the two phases but did not fully eliminate it, and thus the gases were still able to circumvent the zeolite as illustrated in **Figure 1-9**.[19] A different behavior was seen when a copolymer consisting of m-phenyl-diamenel/3,5 di-t-butyl (aminophenoxy) benzene (3:1) and 4,4'-Bisphenol A dianhydride (MPD/3,5di-t-Bu- APB-124 (3:l) and BPADA), a more rigid polymer, was processed above the polymer glass transition temperature with silylated zeolites.[18] The MMM appeared to have good adhesion in SEM images but showed gas transport properties that were practically unchanged from the original polymer. It was suggested that the reaction between the coupling agent and the polymer did work to bind the two phases. However, during drying the polymer contracted against the zeolite and created a dense polymer layer at the interface of the materials as clarified in **Figure 1-9**.[5,8,18,29] This dense polymer layer blocked the gases from going through the more selective zeolite.

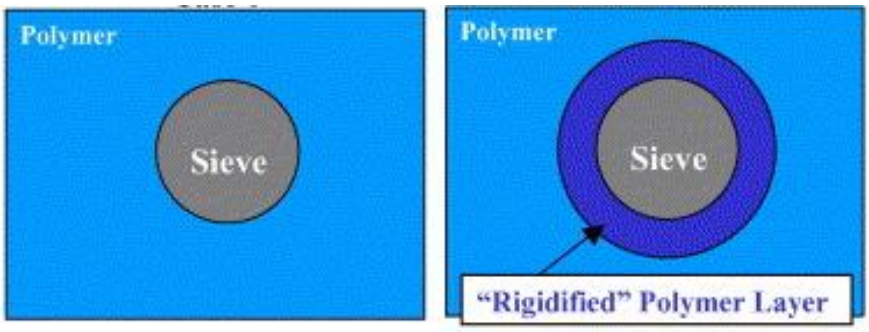

Figure 1-9. Illustration of dense polymer layer formed when zeolites are crosslinked to the polymer phase.[29]

The methods for improving MMMs discussed thus far are less than optimal because they do not improve the MMM gas separation performance, require complicated processing conditions, or are limited to a specific class of polymers and/or casting solvents. A more generally applied method is by depositing inorganic whisker structures on the zeolite surface to provide roughness for interlocking between polymer and zeolite as illustrated in **Figure 1-10**.[8,20–22,26,30]

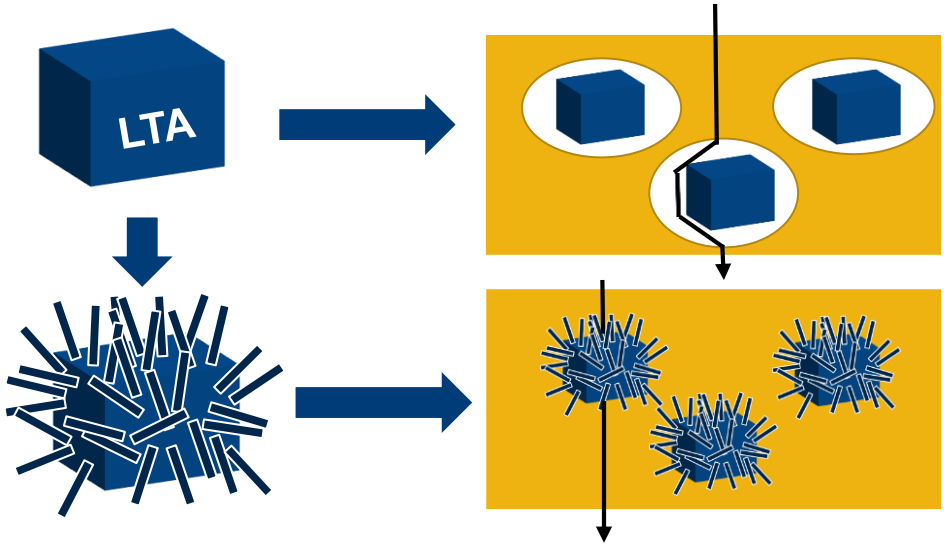

Figure 1-10. Illustration of how functionalization improves membrane gas separation properties.

1.4 Deposition of Mg- based Nanostructures on Zeolites

1.4.1 Functionalization methods

The deposition of inorganic nanostructures has been used to roughen molecular sieve particle surfaces. In particular, MgO_xH_y ($1 \leq x \leq 2$, $0 \leq y \leq 2$) nanostructures have been grown on the surface of zeolites such as pure-silica MFI and aluminosilicate LTA through four techniques: Grignard decomposition reactions,[26,30] solvothermal and

modified solvothermal depositions,[21,22] and ion-exchange induced surface crystallization.[34] The four surface-modification techniques are summarized in **Figure 1-11**.

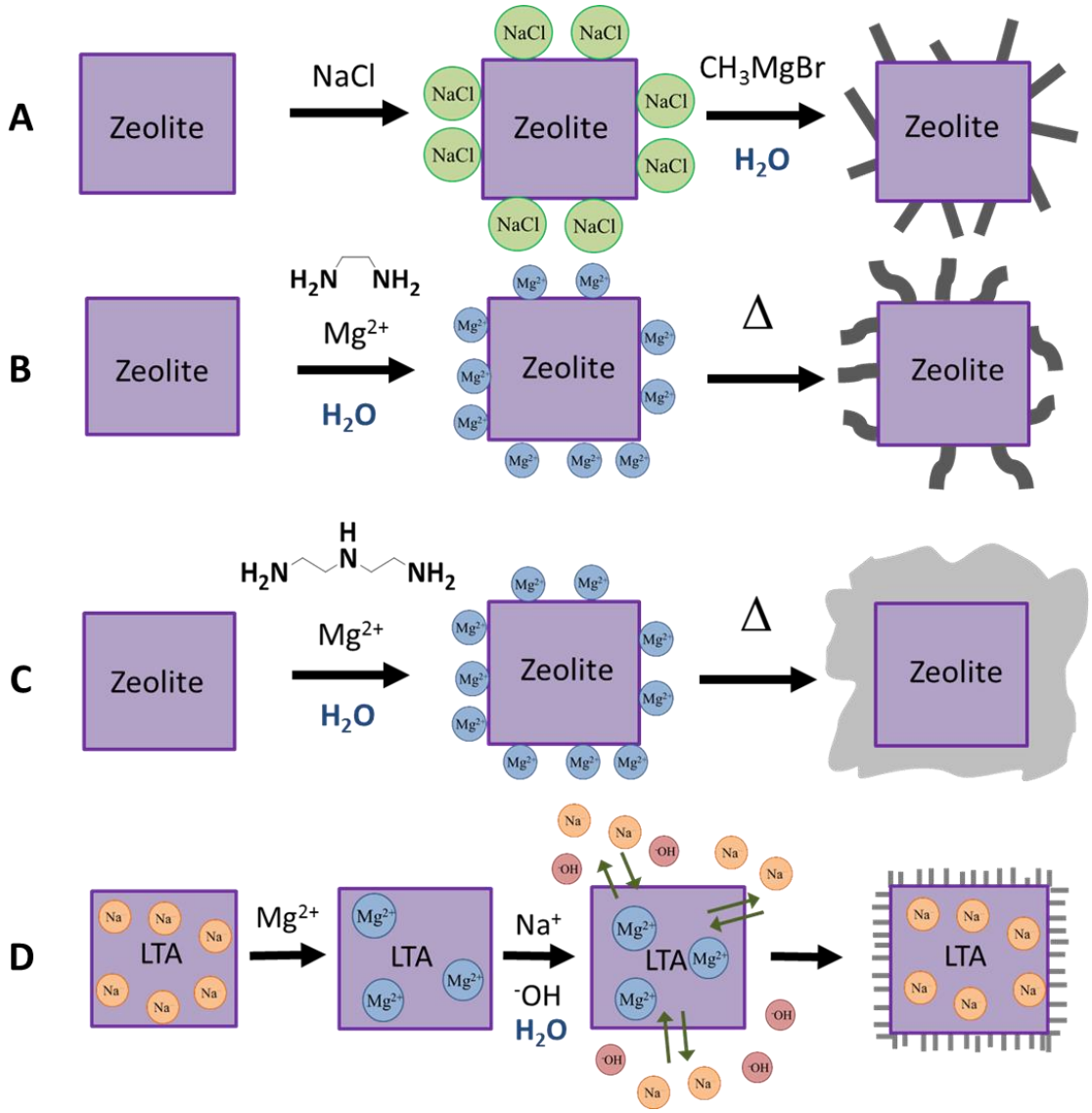

Figure 1-11. Synthesis of nanostructures for A) Grignard, B) solvothermal, C) modified solvothermal, and D) ion exchange functionalization methods. [84]

The Koros group developed a Grignard-based functionalization route, whereby a Grignard (alkylmagnesium bromide) reagent was hydrolyzed in the presence of the zeolite material.[26,30,35] There are currently two variants of the Grignard method that use different pretreatment procedures: the use of thionyl chloride for dealumination of LTA surfaces[30,35] or the use of NaCl to seed zeolite surfaces.[30,36] Additionally, a sol-gel variation of the Grignard method has recently been published.[37] In previous work, the synthesis method involved dispersing the Grignard reagent in toluene with the zeolite, quenching with isopropanol, and reacting the Grignard intermediate with water to form the precipitate of $Mg(OH)_2$.[26,30] It was initially thought that the reaction of the Grignard reagent and isopropanol created the crystals, and that the $Mg(OH)_2$ crystals form regardless of surface preparation. However, to get the nanorod shaped crystals as desired, it was found helpful to have NaCl deposited on the surface by soaking the zeolite in a NaCl solution or reacting an aluminosilicate zeolite such as LTA with thionyl chloride. The resulting structures from the Grignard method (after the thionyl chloride dealumination) were suggested to be crystalline $Mg(OH)_2$ by X-ray diffraction(XRD), and improved CO_2/CH_4 gas selectivity was observed compared to unmodified zeolite MMMs and pure polymer membranes.[26,30]

More recently, solvothermal methods were developed by the Jones and Nair groups to produce nanostructures that were generally comparable in morphology to those produced by the Grignard reaction on both pure-silica MFI and aluminosilicate LTA zeolite surfaces, via more benign chemistry amenable to scale-up.[21,22] These methods depend on the use of a basic organic solvent complex with water and Mg^{2+} ions to nucleate and grow the nanowhiskers that deposit on the surface of the zeolite. The

resulting deposited magnesium species were not identified by X-ray diffraction because the zeolite peaks overwhelm those of the much smaller volume of surface nanocrystals, but in the original solvothermal method they were suggested to be $Mg(OH)_2$ when synthesized in the absence of zeolite.[38] Membrane permeation data showed that the solvothermal methods lead to the formation of membranes that showed better gas separation properties than MMMs made without zeolite surface modification.[21]

In the final ion-exchange method developed by the Jones and Nair groups, the extra-framework cations, Na^+, were first exchanged with Mg^{2+} from a salt solution at a neutral pH. Clearly this method can only be used on aluminosilicate zeolites that possess counter ions such as Na^+LTA^-. Subsequently, the zeolite was hydrothermally reacted with a source of Na^+ ions at a slightly basic pH (~ 9.5). During the hydrothermal treatment, reverse ion-exchange occurs. Due to the low solubility products of $Mg(OH)_2$ and related MgO_xH_y materials, the Mg^{2+} ions exiting the zeolite reacted immediately with the basic solution to form nanostructures at the zeolite surface.[34]

1.4.2 Previous Theories on Improvements to Adhesion by Nanostructuring

Shu et al. proposed a mechanism for the observed improvement in adhesion between the polymer and functionalized zeolite that consists of entropic and enthalpic contributions.[26] Firstly, it has been suggested that the polymer, which has a natural random coil shape in solution, does not have to deform to attach to the nanostructures on the surface of the zeolite because it can penetrate between them and is, consequently, more entropically favorable. In an unfunctionalized zeolite system, the polymer must rearrange to a linear conformation to have contact with the zeolite. These two scenarios are illustrated in **Figure 1-12**. It is also hypothesized that the roughened surfaces provide

a higher surface area for non-covalent interactions such as Van Der Waals forces to take place compared to the unfunctionalized zeolite.[26] This results in more points of contact between a polymer chain and the functionalized zeolite and requires more energy to cause debonding between the two phases, as might occur during the solvent removal step in MMM processing (**Figure 1-13**).[26]

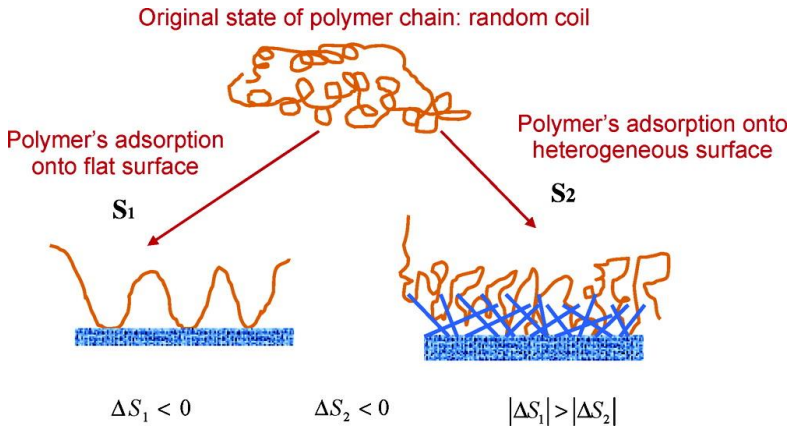

Figure 1-12. Cartoon of polymer attachment to nanostructured zeolites and the entropically-costly deformation required for this attachment.[26]

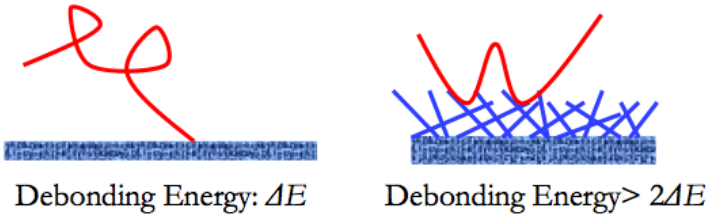

Figure 1-13. Illustration of the additional points of contact in a functionalized zeolite compared to bare zeolite.[26]

1.5 Materials Background

1.5.1 Zeolites

In addition to gas separations, zeolites have a wide variety of other applications. Aluminosilicate zeolites can be used as desiccants or adsorbents for small, polar molecules such as water or alcohols because of their hydrophilic or charged structure and their size selective pores.[23,39] Additionally, they are important as acidic catalysts especially when the reaction is aided by a size selective catalysis mechanism such as hydrocarbon transformation using fluidized catalytic cracking used to produce gasoline.[39] Zeolites form ideal catalysts or catalyst supports because they can be used in a heterogenous manner and are easily separated, regenerated, and modified.[23] Furthermore, aluminosilicates with a balancing cation can also be used for their ion exchange properties such as in detergents for water softening and Cs^{+} and Sr^{2+} removal from radioactive waste streams.[17,23,40]

The composition of the zeolite framework is generally determined by the synthesis conditions of the zeolite but can also come from post synthetic modification. In particular, a lower Si/Al ratio is very important for creating ion exchangeable zeolite species and determines the concentration and strength of acidic sites present. A higher Si/Al ratio also forms more hydrophobic and hydrothermally stable zeolite species. Zeolites can have a Si/Al ratio of 1 (such as the LTA in this work) to infiniti. A 1:1 Si:Al ratio is the lower limit composition because AlO_4 tetrahedra exhibit electrostatic repulsion and bonding below this ratio is not favorable.[23] In addition to silica and alumina, other elements can be incorporated into a zeolite-type structure including B, Zn, P and transition metals such as Co, Ge, and Mn. The resulting product is called a

'crystalline molecular sieve,' rather than a zeolite, and can expand the functionality of these materials.[23]

1.5.1.1 Synthesis Mechanism

Zeolites have several stages in their synthesis including an induction period, nucleation, and crystal growth/aggregation.[41] A simplified example of what these stages look like during the synthesis are shown in **Figure 1-14** and the specific mechanism of growth in solution is illustrated in **Figure 1-15.**[42,43] Typically, zeolite synthesis is done via a hydrothermal, basic reaction where silica, alumina, and an additional cation and/or structure directing agent (SDA) are combined in a sealed container and heated at elevated temperatures.[41,43] The first step of the synthesis is the induction period where the amorphous reactants blend together throughout the solution

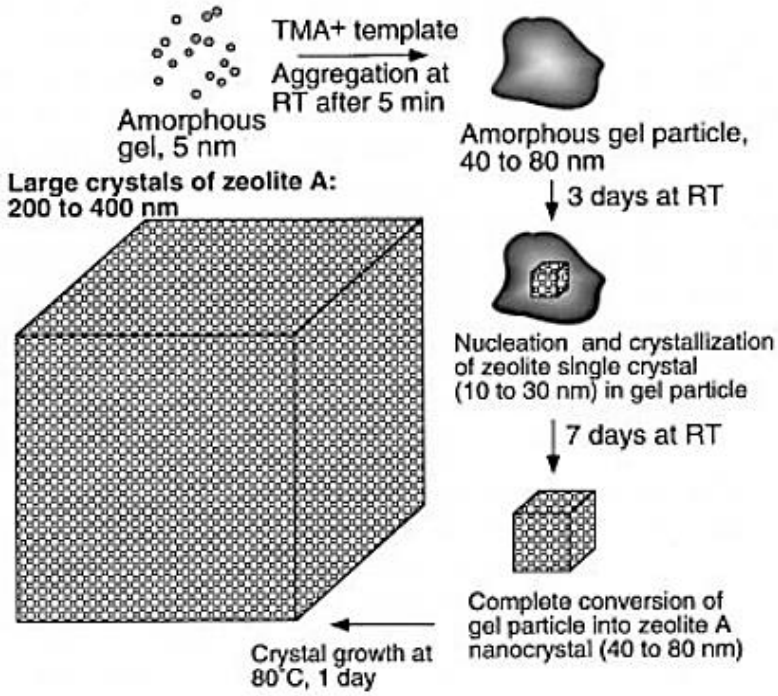

Figure 1-14. Crystal growth mechanism of LTA.[43]

and come to a well distributed equilibrium. During this period, amorphous silicate or aluminosilicate materials are formed that equilibrate between their solid amorphous and polymeric form.[41] This step is often called the "evolution of order" and it has been determined to be crucial to the formation of an ordered zeolite product. Without this step, the resulting product would be amorphous or quartz-like without the pore channels that

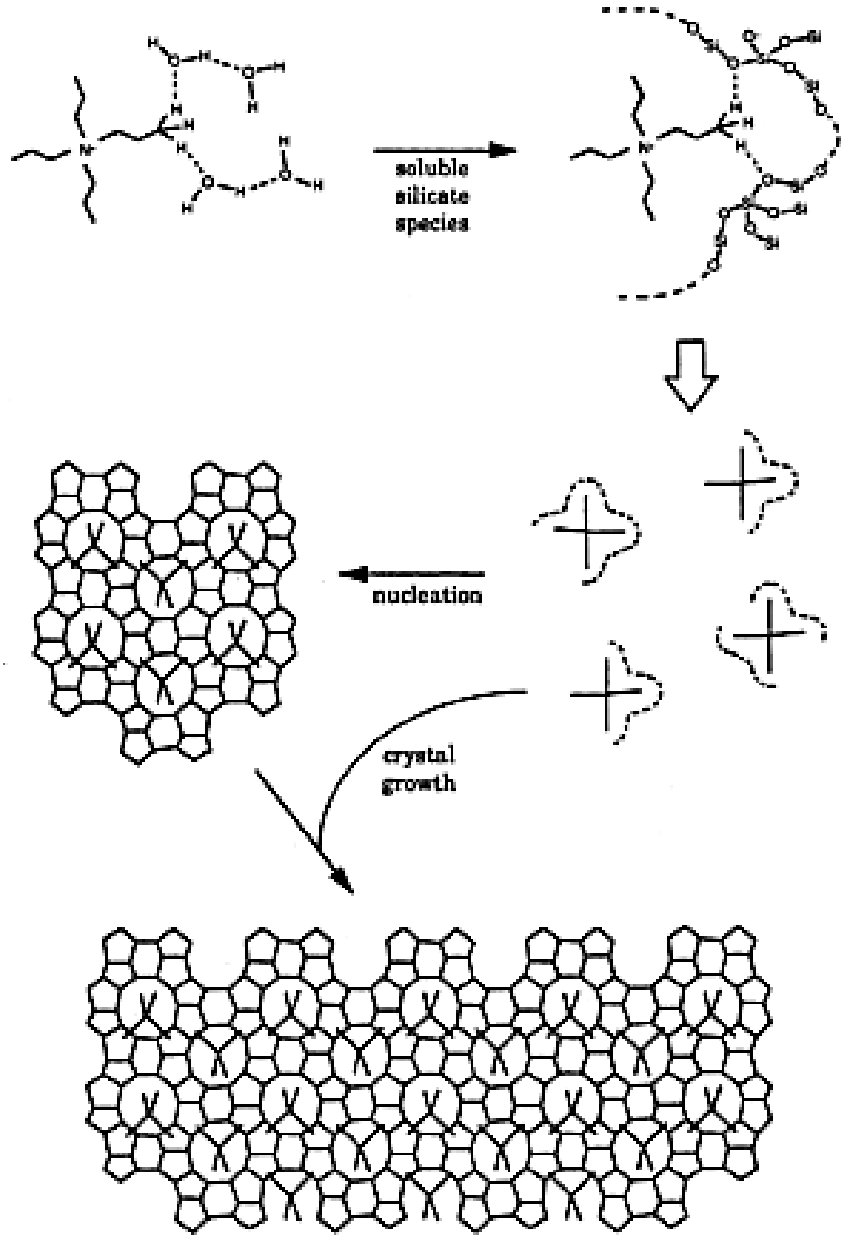

Figure 1-15. Crystal growth mechanism of TPA-MFI.[42]

are vital to zeolite applications.[41] An example of how the SDA contributes to this order and forms the pores is illustrated in the right of **Figure 1-15**.[41] After the induction period, nucleation occurs and the crystal growth starts. Nucleation is a step in the phase transition mechanism where the ordered amorphous materials convert into an ordered collection that is able to sustain and propagate crystal growth. [41] The nucleation phase can also be aided by the use of seeds (small preformed zeolite crystals) that can be used as the growth center. The crystal growth can continue by step-by-step addition to the crystalline zeolite or an aggregation of smaller particles.[41,43] The reaction is typically stopped when the reactants are consumed, the reaction is cooled, or there is a significant change in the pH of the zeolite synthesis solution.

1.5.2 $Mg(OH)_2$

$Mg(OH)_2$ is a bivalent metal hydroxide material that is naturally occurring and has the mineral name of brucite.[44] The $Mg(OH)_2$ structure (**Figure 1-16)** and consists of a CdI_2 arrangement with hexagonal Mg^{2+} and OH^- layers where Mg forms $Mg(OH)_6$ octahedra.[44] $Mg(OH)_2$ is a mineral of interest for its uses as an insulator, paint additive, flame retardant, acid neutralizer, and fertilizer additive.[45] Additionally, a growing application is the use of $Mg(OH)_2$ as a permanent CO_2 sink by forming $MgCO_3$ compounds. [46] Brucite often occurs in nature in equilibrium with MgO hydration and dehydroxylation determine the forward and reverse reactions.[45,47]

$Mg(OH)_2$ can be synthesized using hydrothermal, solvothermal, electrodeposition, sol-gel, and microwave synthesis methods.[45] The hydrothermal and solvothermal synthesis methods are relevant to the work in this thesis and will be explained further. Hydrothermal synthesis methods typically combine a Mg salt such as $Mg(NO_3)_2$ or

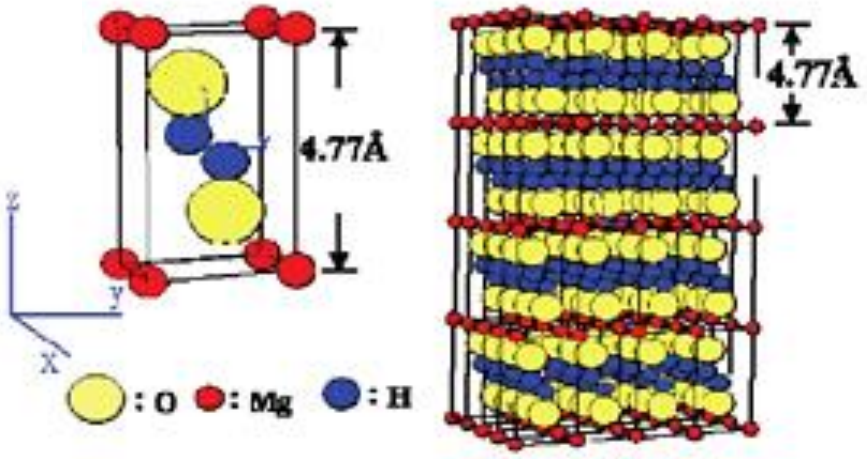

Figure 1-16. $Mg(OH)_2$, or brucite, unit cell and structure.[51]

$Mg(SO_4)$ and a basic, aqueous solution to produce a highly homogenous crystal with a uniform composition and narrow particle size distribution.[45] Yan et al. and Zhao et al. were able to modify the shape of $Mg(OH)_2$ by adding a surfactant (PEG-1000 and Pluronic P123), forming nanorods and nanotubes with controllable size and aspect ratios. [44,48] Solvothermal reactions have also been used to form $Mg(OH)_2$. Solvothermal reactions are typically done in one or two steps by combining a Mg salt such as $MgCl_2$, trace water, and a basic solvent/reaction medium such as ethylenediamine (en). [38,49,50] The solvothermal synthesis is hypothesized to occur because the ethylenediamine acts as a bidentate ligand to form a Mg^{2+}-en complex. [38] Water in the solvothermal reaction provides hydroxyl groups that coordinate with the Mg and fully replace the en-ligand when the complex decomposes at higher temperatures during the solvothermal reaction. The intermediate complex proposed in this mechanism is thought to be similar to chlorphyll-water complexes shown in **Figure 1-17**.[38] Additionally, it

has been noted that a high ethylenediamine to water ratio was important to form the nanorod shape.[22]

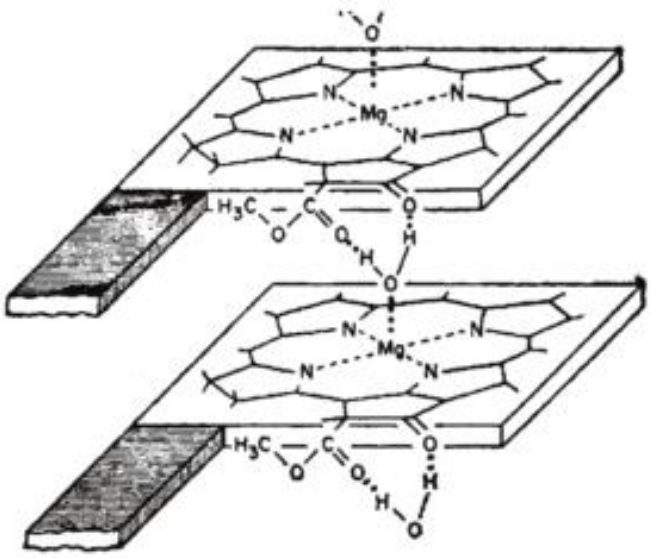

Figure 1-17. Illustration of chlorophyll-α-water-chlorophyll- α interaction. [38]

1.5.3 MgO

MgO, also known as periclase, has a NaCl, cubic structure as shown in **Figure 1-18**.[49,51] The bonding in this structure is highly ionic in character and MgO has a high thermal stability with a melting point of 2852 °C. [49] MgO has been used in applications as a catalyst, catalyst support, filler in cosmetics, toxic water treatment, chemical warfare remediation, and for its optical properties.[49,52] MgO is typically formed by dehydration of $Mg(OH)_2$ precursors synthesized through the aforementioned hydrothermal or solvothermal reactions by calcination at high temperatures.[52] However, it has been seen that this dehydration can start occurring as low as 300 °C. [45] Additionally, MgO has been formed through reaction of a $Mg(O_4C_2)$-oleylamine complex and triphenylphosphine at a temperature of 240°C.[53]

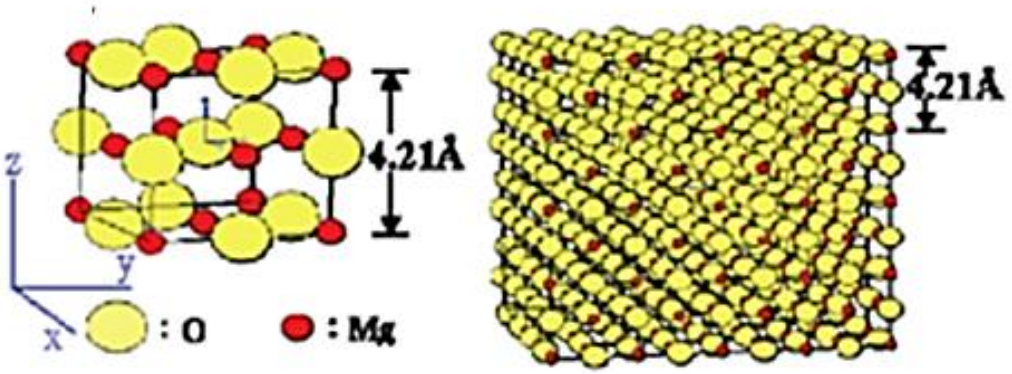

Figure 1-18. MgO, or periclase, unit cell and structure.[51]

1.5.4 MgO_xH_y Materials

Because there is an equilibrium between MgO and $Mg(OH)_2$, there is also the possibility of partial hydration or dehydroxylation to form MgO_xH_y intermediates.[46,54] These MgO_xH_y intermediates act as solid solutions and contain both the MgO and $Mg(OH)_2$ structures as shown in **Figure 1-20** that vary by layer.[46,54] It has been observed that when $Mg(OH)_2$ is slowly dehydrated at a low temperature, the MgO maintains the morphology of the original $Mg(OH)_2$ structure but consists of intergrown

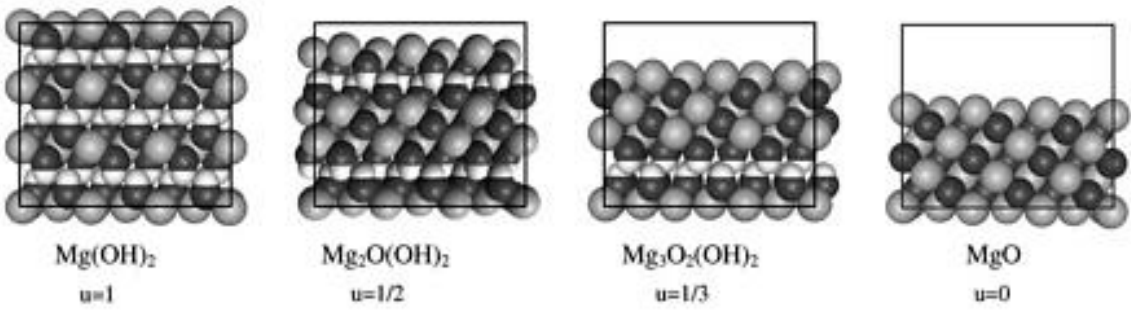

Figure 1-19. Examples of possible intermediate MgO_xH_y species between $Mg(OH)_2$ and MgO. The light gray represents magnesium, dark gray-oxygen, and white-hydrogen. The u value is the degree of dehydroxylation.[54]

cubic MgO domains.[46] Each of these intermediates is stable but may not be enthalpically favorable as can be seen in **Figure 1-20**.[46]

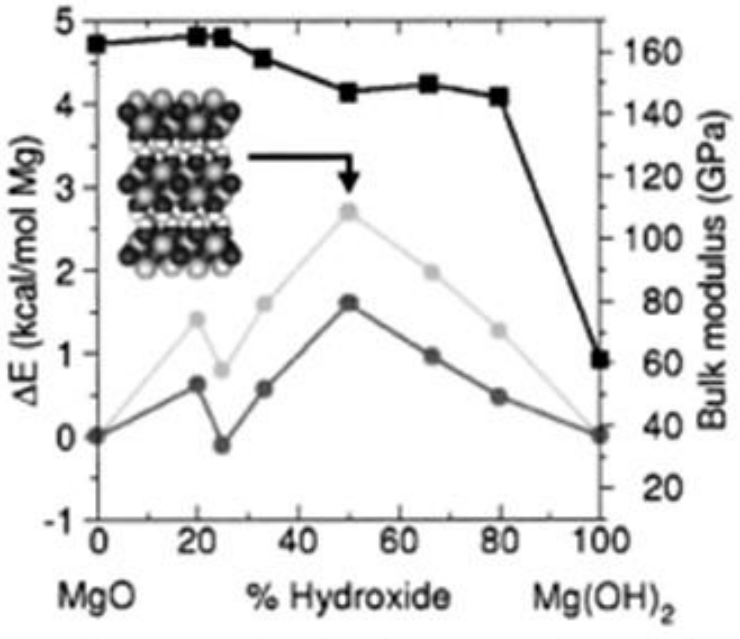

Figure 1-20. Free energy (dark grey), enthalpy (light gray), and bulk moduli (black) for MgO, $Mg(OH)_2$, and the stoichiometric intermediates. In the structure shown, the light gray represents magnesium, dark gray-oxygen, and white-hydrogen. The u value is the degree of dehydroxylation. [46]

1.5.5 Other Composite Materials

Composites consist of at least two material phases that have more desirable properties when combined than the original two materials. Composite materials are used in many applications including coatings, medical implants, optical materials, membranes, sensors, reinforced metals, electronic components, and superconductors.[55–60] Composites are often polymer-polymer, inorganic-inorganic, or polymer-inorganic combinations and can be used to contribute anti-microbial properties, strength, rust protection, faster or more selective transport through membranes, addition of

photocatalytic or catalytic properties, hydrophobicity/hydrophillicity, or an advantageous processing quality (i.e. metal based coating materials).[61–65] Several important parameters to be considered when choosing the material phases include an assessment of their mechanical properties (elastic modulus and tensile strength), density, thermal stability, thermal expansion coefficients, size and shape, compatibility between the materials, and the cost.[66] Occasionally, these properties are not compatible and result in poor performing composites such as the original MMMs introduced in this thesis.

Polymer-ceramic membranes have been widely used in many membrane separations applications including gas separations, pervaporation, ultrafiltration and nanofiltration, reverse osmosis, and fuel cell applications.[67–69] One interesting and novel gas separation membrane combined TiO_2 nanoparticles and poly(vinylidene-fluoride) (PVDF) polymer for the purpose of increasing the membrane's pressure stability and resistance to compaction.[67]. Zeolite-polymer membranes have also been applied to direct methanol fuel cells using Mordenite (zeolite, typical Si/Al=5, main channel pore size of 7 Å) and poly(vinyl alcohol) (PVA).[68] Specifically, a delaluminated form of Mordenite with a Si/Al ratio of 40, preferential adsorption of water over methanol, and a pore size of up to 20 nm was used in this work. The traditionally low conductivity of the zeolite was increased by soaking in sulfuric acid.[68] PVA was used because of its hydrophilic nature and good adhesion to the zeolite.[68] This composite material resulted in a 20-fold improvement of the proton conductivity/ methanol permeability compared to Nafion, the traditionally used material for this application, and shows promise for producing a better fuel cell.[68] Additionally, Lind et al. have done work on improving membranes for reverse osmosis applications by coating

zeolite-poly(amide) thin film composites (TFC) on poly(sulfone) ultrafiltration membranes.[69] These membranes were formed by interfacial polymerization of diamine and acid chloride monomer solutions with LTA zeolites.[69] The LTA particles used were used because of their pore diameter which can exclude Na^+ and Cl^- ions that have hydrated diameters of 8-9 Å. [69] The zeolite size (100 nm) was specially chosen to match the TFC thickness allowing preferential flow through the zeolite with a higher flux and similar (salt) rejection to other conventional poly(amide) TFCs.[69] Later, LTA was easily replaced with silver exchanged LTA to give the membrane additional antibacterial properties.[69]

1.6 Objectives and Strategy

Previous work on surface-roughened-zeolites has mainly been devoted to developing a range of surface nanostructuring methods and characterization of their MMM gas permeation performance. However, there is little knowledge of the microscopic structural properties of these surface nanostructures, how these properties relate to the polymer/inorganic interfaces and their subsequent effect on the gas separation performance and membrane quality. The objective of this work is to *provide a more fundamental understanding of the nanostructured-zeolite mixed matrix membrane system with a specific emphasis on the components of the interfacial region between the two materials*. Different methods of analysis were used to probe each aspect of the MMM including the nanostructured zeolite, the interfacial region, and the bulk membrane properties of MMMs made with four different surface functionalization methods. The specific objectives of this work were to:

- Functionalize zeolites LTA (Aluminosilicate) and pure silica MFI (silicate) with four functionalization methods, characterize the nanostructures produced by each method and the properties of the zeolite post-functionalization, and evaluate their suitability for use in MMM materials.
- Assess the quality of MMMs produced with each of the four functionalization methods by studying the membrane 'bulk' properties including gas permeation, dispersion, and mechanical properties.
- Characterize the interfacial properties between the zeolite and polymer in MMMs produced with each of the four functionalization methods by examining the polymer properties at the interface compared to the bulk material, and evaluating the chemical interactions between the two materials.

2 Chapter 2: Functionalization of LTA and MFI and analysis of the MgO_XH_Y nanostructures produced[2]

2.1 Introduction

A critical design issue in the fabrication of MMMs is control over the polymer/inorganic interfaces, which often determine the membrane performance.[70] Control over the interfacial properties of such composite systems may also find applications in other areas such as supercapacitor devices,[71] composite building materials,[64,72] and photovoltaic devices.[73] The use of inorganic nanostructures to roughen molecular sieve particle surfaces has recently allowed enhancements in the properties of MMMs in gas separations.[20,21,30] In particular, MgO_xH_y ($1 \leq x \leq 2$, $0 \leq y \leq 2$) nanostructures have been grown on the surface of zeolites such as pure-silica MFI and aluminosilicate LTA through four techniques: Grignard decomposition reactions,[26,30] solvothermal and modified solvothermal depositions,[21,22] and ion-exchange induced surface crystallization.[34] The roughened surfaces provide a high surface area for non-covalent interactions, and also allow for entanglement of the polymer chains leading to

---

[2] This chapter is largely reproduced from "Structure-property relationships of inorganically surface-modified zeolite molecular sieves for nanocomposite memrbaen fabrication," by Megan E. Lydon, Kinga A. Unocic, Tae-Hyun Bae, Christopher W. Jones, and Sankar Nair, published in the Journal of Physical Chemistry C, in 2012, volume 116, pages 9636-9645.

enhanced adhesion.[26,64,72,74] The four functionalization methods studied in this work produce surface nanostructures that may appear superficially similar under SEM observation, but in fact differ considerably in shape, size, surface coverage, surface area/roughness, type of attachment to the zeolite surface, and degree of zeolite pore blocking. The evaluation of these characteristics by a combination of TEM, HRTEM, N_2 physisorption, multiscale compositional analysis (XPS, EDX, and ICP-AES elemental analysis), and diffraction (ED and XRD) allows improved understanding of the origin of disparate gas permeation properties observed in MMMs made with four types of surface-modified zeolite LTA materials, as well as a rational selection of the method expected to result in the best enhancement of the desired properties (in the present case, CO_2/CH_4 selectivity increase without sacrificing permeability). A parallel study on pure silica MFI surface nanostructures is also presented, to compare and contrast with the zeolite LTA case.

The previous work on surface-roughened-zeolites has been mainly devoted to developing a range of surface nanostructuring and roughening methods and their use in the fabrication of MMMs for improved gas permeation properties. However, there is little knowledge of the microscopic structural properties of these roughened surface nanostructures, and their correlation to the properties of the membranes obtained using particles modified by each of the four methods described above. The purpose of this investigation was to probe the structural properties of the nanowhiskers produced by each method and correlate these properties with its suitability for use in composite membranes. We focus on the surface modification of aluminosilicate zeolite LTA and pure-silica zeolite MFI, both of which have been used in the fabrication of MMMs for separation

applications.[12,21,22,28,75] In particular, we apply a range of physicochemical characterization techniques to study the surface morphology, crystallinity, surface area, and micropore volume of the modified zeolite particles. All these factors are expected to strongly affect the control of polymer/zeolite adhesion properties. The new insight obtained also enables a rational selection and application of the appropriate surface-modification technique.

2.2 Experimental Methods

2.2.1 Materials

The following chemicals were commercially available and were used as received: deionized water (DI water), sodium hydroxide (NaOH, 98%, Sigma Aldrich), aluminum isopropoxide ($Al(OiPr)_3$, 97%, Sigma Aldrich), tetramethylammonium hydroxide (TMAOH, 25% w/w aqueous solution, Alfa Aesar), colloidal silica (Ludox HS-30, 30 weight % aqueous solution, Sigma Aldrich), tetraethylorthosilicate (TEOS, 98% Sigma Aldrich), tetrapropylammonium hydroxide (TPAOH, 40% w/w aqueous solution, Alfa Aesar), magnesium chloride hexahydrate ($MgCl_2$, 99-102.0%, Sigma Aldrich), sodium nitrate ($NaNO_3$, 99.0%,Sigma Aldrich), sodium chloride (NaCl, Fisher Scientific), methylmagnesium bromide (3.0 M in diethyl ether, Sigma Aldrich), isopropanol (99.50%, BDH), magnesium sulfate heptahydrate ($MgSO_4$, Acros), diethylenetriamine (DETA, 99%, Sigma Aldrich), ethylenediamine (EDA, 99%, Sigma Aldrich), calcium chloride dehydrate ($CaCl_2$, 99%, Sigma Aldrich), and toluene (99.80%, Sigma Aldrich).

2.2.2 Synthesis of Zeolite LTA and MFI Particles

Zeolite LTA was prepared as described in previous work.[21,22,76] First, 1.080 g NaOH was combined with 246.86 g H_2O under stirring. A solution of molar composition 1 Na_2O:10 SiO_2:5 Al_2O_3:20 TMA_2O:170 H_2O was made by adding 28.435g aluminum isoproproxide, 196.62g tetramethylammonium hydroxide, and 28.43g Ludox silica solution (HS-30) in order with stirring. The solution was stirred 4 hours and then heated in an autoclave at 100°C for 24 hours with rotation. The resulting zeolite LTA particles were washed with water, sonicated, and centrifuged four times to wash the particles. Zeolite MFI was also prepared as described in previous work.[77,78] First, 25 g of TEOS was added dropwise into 21.53 g TPAOH. This solution was stirred for one hour until the solution turned clear. Next, 368.12 g deionized water was added to the solution and stirred for an additional 24 hours. The solution was then heated in an autoclave at 150°C for 48 hours with stirring. The zeolite was washed in the same manner as LTA.

2.2.3 Surface Modification Techniques

2.2.3.1 Grignard Method

The Grignard reaction used in this work was completed using the NaCl seeding pre-treatment method.[36] This method produces nanostructures of a different morphology from those produced by the thionyl chloride method,[30,35] but does not change the surface properties of the zeolite. First, 0.805 g zeolite LTA was added into a solution of 14.11 g NaCl in 80.5 ml H_2O to 'seed' the zeolite surface with NaCl. The zeolites were stirred for 2 hours, filtered, and dried overnight. All glassware, stir bar, cannula needle, and the zeolite particles were dried at 80°C before the reaction to eliminate moisture. Next, 0.75 g NaCl seeded zeolite and 12 mL toluene were added to a

round bottom flask with stir bar. The stoppered flask was sonicated for 5 minutes to disperse particles and then purged with nitrogen. The Grignard reagent was transferred by cannula into a (sealed) secondary container and 2 mL of reagent was transferred to the reaction vessel by needle transfer from the secondary container. The Grignard reagent was added dropwise with stirring. The reaction mixture was sonicated for 4 hours and stirred for another 12 hrs. The reaction was placed under N_2 flow with stirring and an ice bath to dissipate extra heat. The reaction was quenched by slowly adding isopropanol dropwise and then to excess. Particles were washed and centrifuged twice with isopropanol and twice with 40 mL DI H_2O.

2.2.3.2 Solvothermal Method

This method was carried out as described in previous work.[21,22] All zeolites were washed with isopropanol prior to functionalization. A 23 mL Teflon liner, stir bar, and the isopropanol washed zeolite particles were dried at 80°C before use. First, 0.2 g zeolite was added to 10 mL ethylenediamine (EDA) in a Teflon liner and sonicated for 30 seconds with a sonication horn. Then, 1 mL of a 1M $MgSO_4$ aqueous solution was added to the EDA mixture dropwise with stirring. The solution was stirred at room temperature for 1 hour, autoclaved at 160°C for 12 hours with rotation, and washed with isopropanol and DI water.

2.2.3.3 Modified Solvothermal Method

This method was carried out as described in previous work[21,22] and differs from the solvothermal method only in the substitution of the solvent. To prevent infiltration and trapping of EDA in the pores of zeolite LTA, a larger amine solvent molecule was used. Zeolites in this method were also washed prior to use in isopropanol.

The washed particles and a 23 mL Teflon liner were dried prior to use in an 80°C oven. First, 0.2 g zeolite, 0.124 g $MgSO_4$, and 10 mL diethylenetriamine (DETA) were combined in a liner and sonicated with a sonication horn for 30 seconds. Next, 1 mL H_2O was added dropwise to the solution and left at room temperature for 1 hour. The solution was autoclaved at 180°C for 12 hours with rotation and particles were washed with isopropanol and DI water.

2.2.3.4 Ion Exchange Method

Before functionalization as synthesized LTA, Na-LTA, was ion-exchanged to Mg-LTA by dispersing 1g LTA in a solution of 1.0165 g $MgCl_2$ in 50 mL H_2O. The mixture was stirred for 1 hour at room temperature, filtered with a 0.2 μm filter, and dried overnight. A $NaNO_3$ solution was made by combining 0.851 g $NaNO_3$ in 100 mL H_2O and the pH was adjusted to 9.55 by adding NaOH. 30 mL of the $NaNO_3$ solution and 0.3 g Mg-LTA are combined in a 45 mL Teflon liner, sonicated with sonication horn for 30 seconds and autoclaved at 160 °C for 12 hours with rotation. The particles were washed with water afterwards.

2.2.4 Characterization

2.2.4.1 X-ray Diffraction

Powder X-ray diffraction (XRD) was carried out with a PAnalytical X'Pert PRO diffractometer operating with Cu Kα radiation and an X'celerator RTMS detector. A step size of 0.002° 2θ and a scan rate of 10 s per step were used.

2.2.4.2 Electron Microscopy

The morphology and composition of bare and surface-modified zeolites were initially characterized using a Hitachi HF-2000 field-emission and JEOL JEM 100CX II TEMs in bright field mode at 200 keV and 100 keV respectively. Samples were prepared by dispersing the particles in isopropanol, sonicating the dispersion, and dropping on a TEM grid.

Scanning electron microscopy (SEM) imaging was done using a Leo 1530 SEM at 5 keV. SEM samples were prepared in the same manner as TEM samples but instead were dropped onto a SEM stub. In order to observe the fine nanostructures, the samples were not gold coated and imaging was done quickly and at a low electron voltage to minimize charging.

High-resolution images of the zeolite structure were recorded at Oak Ridge National Laboratory using a Hitachi HF-3300 TEM-STEM at 300 keV in TEM mode. The samples were embedded in epoxy, microtomed into 50-75 nm slices, and carbon coated to prevent charging.

2.2.4.3 Elemental Composition

Energy dispersive x-ray spectroscopy (EDS) was measured using the Hitachi HF-3300 TEM equipped with a Thermo Scientific EDS system. The spatial resolution of the EDS data was determined by the beam focusing and generally included 3-10 particles. Each measurement was repeated on a second set of particles to confirm the composition. Noran System Six software was used to analyze the data. Samples were prepared by dispersing the particles in isopropanol, sonicating the dispersion, and dropping on a TEM grid.

Elemental analysis by ICP-AES was carried out by Columbia Analytics (Tucson, AZ). X-ray photoelectron spectroscopy (XPS) was performed on a Thermo K-Alpha XPS instrument with Al Kα irradiation via irradiation of powder samples by a flood gun under vacuum.

EDS mapping and line scans were measured in scanning transmission electron microscopy (STEM) mode with an FEI Tecnai F30 HRTEM at 300 keV and an Oxford Inca EDS system. The data was collected and analyzed using the FEI TEM Imaging and Analysis program (TIA).

2.2.4.4 Porosity and Surface Area Measurements

Micropore volume and surface area were determined by nitrogen physisorption using the t-plot and Brunauer-Emmett-Teller (BET) methods respectively. Physisorption measurements were recorded using a Micromeritics TriStar II 3020. The kinetics of N_2 adsorption on Na-LTA were too slow at 77 K to reach equilibrium in a reasonable time scale because of the strong adsorbate-adsorbent polar interactions.[79,80] However, Ca-exchanged LTA has been shown to adsorb nitrogen much faster at 77 K, and hence all samples were Ca-exchanged prior to physisorption measurements.[76,81] Therefore, samples were calcium exchanged by combining 0.15 g functionalized zeolite in 5 mL of a 1M $CaCl_2$ solution and vigorously stirring the mixture while it was heated in a 60°C oven for 5 hours to form Ca-LTA. Ca- LTA samples were filtered, dried, and degassed under vacuum at 120°C for 2 hours before ramping up and holding at 200°C for 8 hours. MFI particles were used as-prepared after being degassed using the same method as above.

2.3 Results and Discussion

2.3.1 Surface Nanostructures on Zeolite LTA

2.3.1.1 Basic Nanostructure Morphology and Crystallinity

Powder XRD patterns of LTA zeolite particles (300 nm) in unmodified and modified forms are shown in **Figure 2-1**. All particles maintained the LTA structure after the four surface-modification treatments. A small peak broadening at approximately 38° 2θ in the solvothermally modified LTA suggests a secondary crystalline phase. This peak suggests the presence of crystalline MgO_xH_y structures such as $Mg(OH)_2$ or MgO that both have an XRD peak in this region.[82] The zeolite LTA treated by the modified solvothermal (**Figure 2-1-D**), Grignard (**Figure 2-1-B**), and ion exchange methods **(Figure 2-1-A**) do not show additional crystalline phases observable by XRD.[83,84] Crystalline nanostructures may still be present for these methods but are not prominent because they occupy only a small volume fraction of the sample.[21,30] Lastly, the ratio between the (2 0 0) and (2 2 0) peak at 7° and 10° 2θ, respectively, varies due to the hydration of the zeolite with a ratio of 1 representing the dehydrated structure and higher values for the hydrated structure.[24]

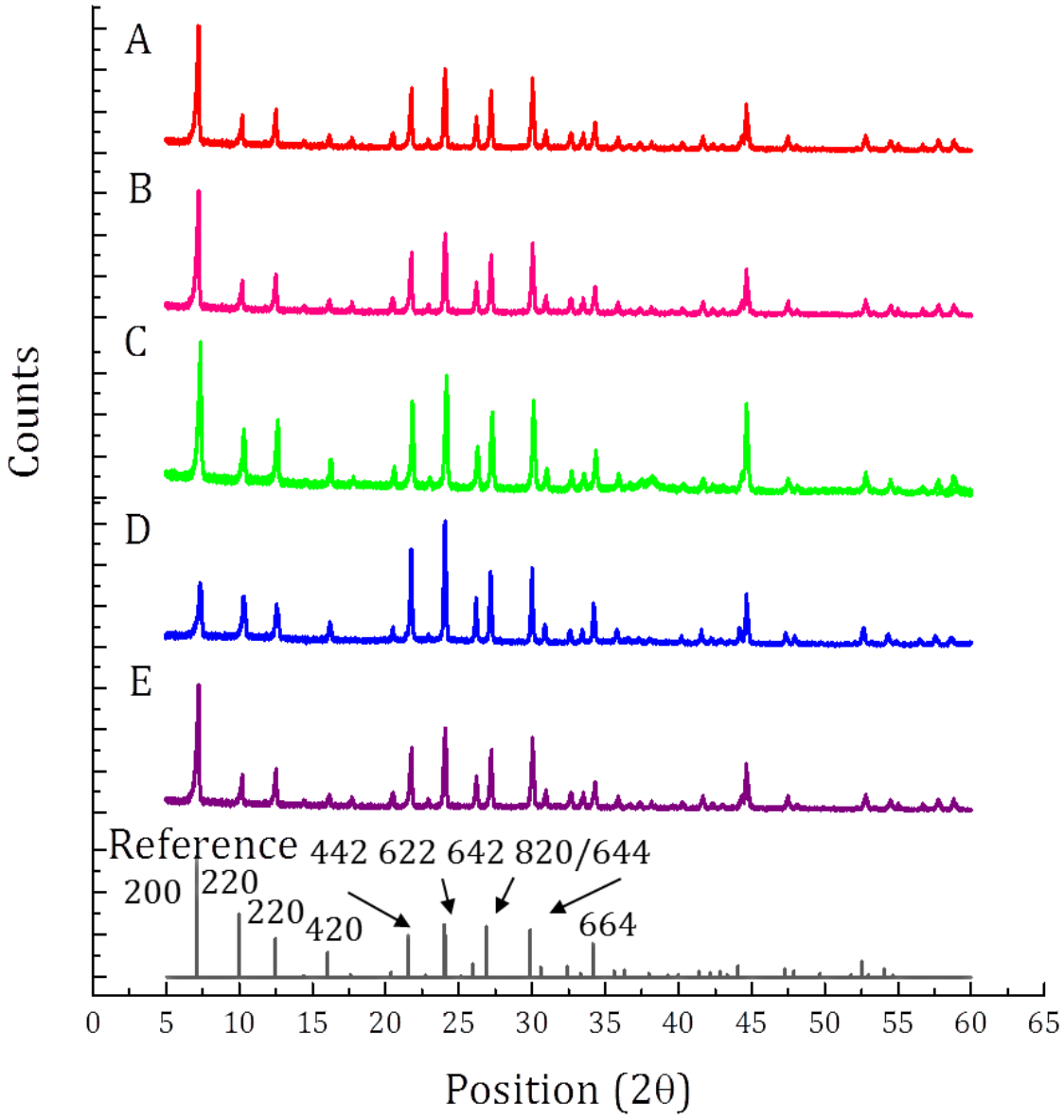

Figure 2-1. X-ray diffraction patterns of (a) unmodified 300 nm LTA particles, and after modification by (b) Grignard, (c) solvothermal, (d) modified solvothermal, and (e) ion exchange methods. The reference peak positions of LTA [83]. The arrow indicates the XRD peak corresponding to crystalline MgO_xH_y structures such as $Mg(OH)_2$ or MgO.[84]

TEM imaging of the modified particles shows the distinctive nanostructure morphology and approximate coverage of the surface structures produced by each functionalization method (**Figure 2-2**). All particles shown in the figure are representative of the samples for each method. The LTA particles modified by the NaCl-seeded Grignard (**Figure 2-2-A**) and solvothermal (**Figure 2-2-B**) methods show loosely-attached surface structures with sparse and uneven coverage. The Grignard method produces straight, nanorod-shaped nanostructures and the solvothermal method produces irregularly shaped nanostructures and a significant amount of unattached materials, thereby creating a mixture with a separate, secondary crystal phase (**Figure 2-3**). In

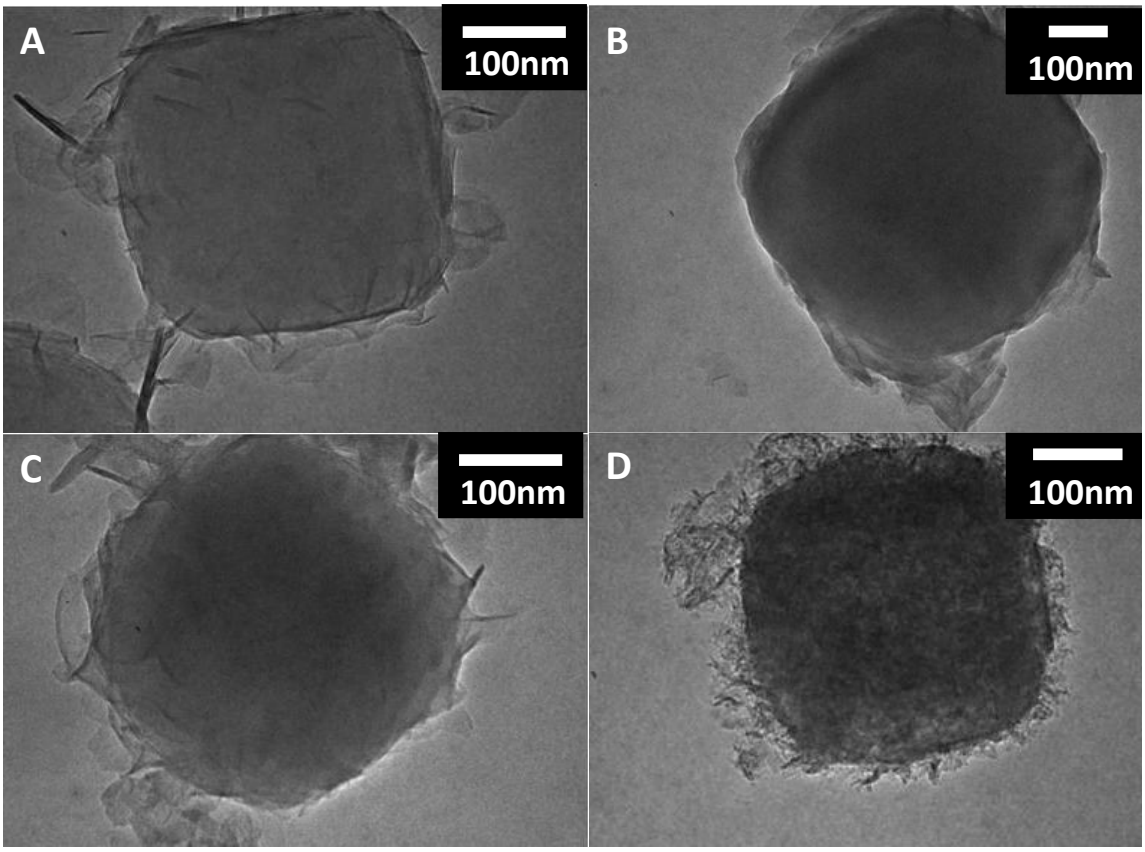

Figure 2-2. Low-magnification TEM images of 300 nm LTA particles modified by A) Grignard, B) Solvothermal, C) Modified solvothermal, and D) Ion exchange functionalization methods. [84]

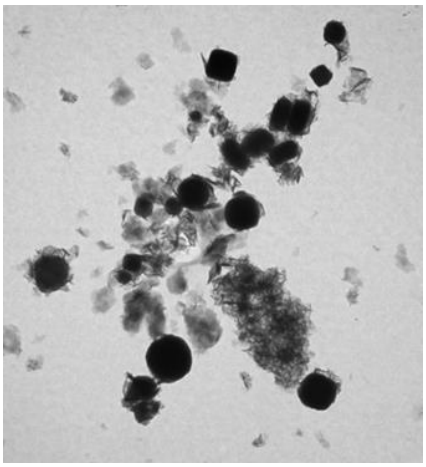

Figure 2-3. TEM image showing existence of secondary phase produced by Solvothermal functionalization of LTA. [84]

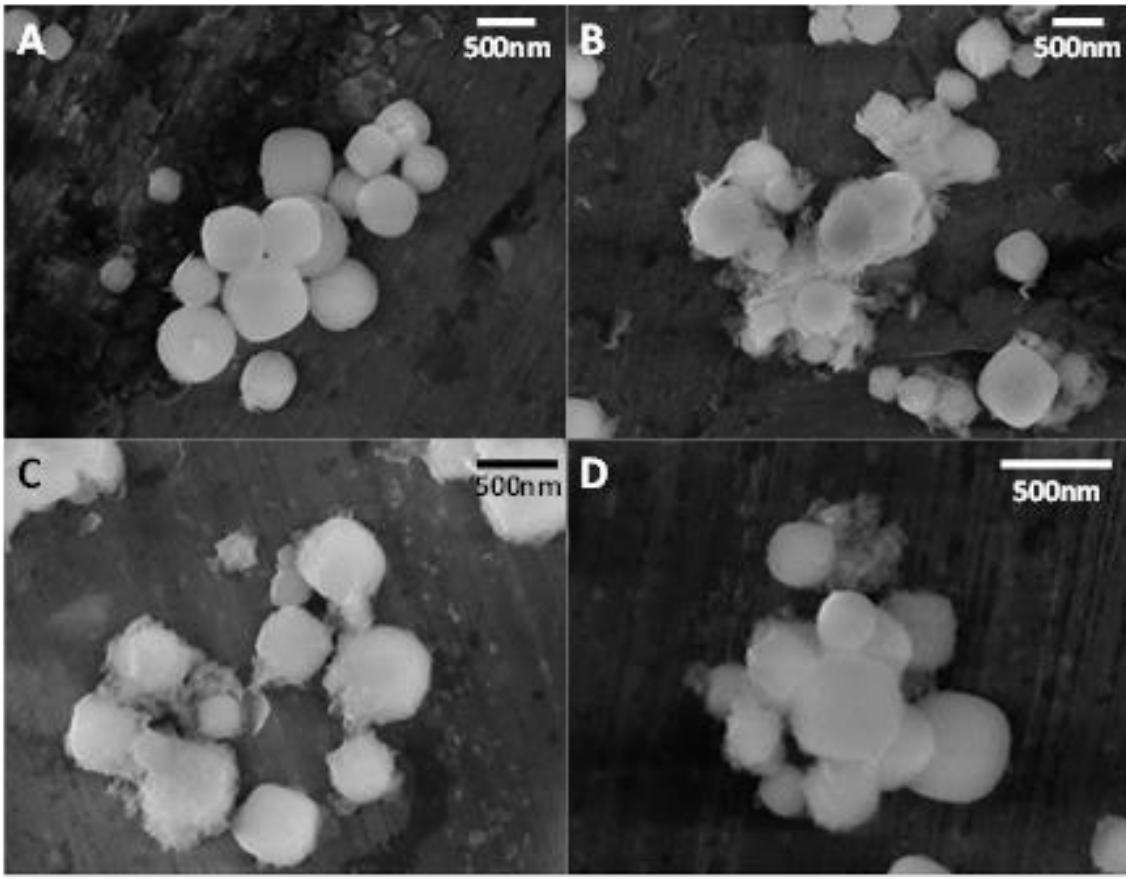

Figure 2-4. SEM images of LTA particles surface-modified by (a) Grignard, (b) Solvothermal, (c) Modified Solvothermal, and (d) Ion Exchange. [84]

contrast, the modified solvothermal and ion exchange methods form nanostructures with much more even coverage on the surface of the LTA particles. The modified solvothermal method produces a sheet-like material encapsulating the zeolite particle, whereas the ion exchange method produces finer nanostructures that extend out from the zeolite surface. These results are also confirmed by SEM imaging included in **Figure 2-4**.

2.3.1.2 Detailed Morphology and Crystallinity

HRTEM imaging was used to observe details of the zeolite-nanostructure interface properties and to obtain a better characterization of the nanostructure crystallinity. HRTEM images of the LTA-MgO_xH_y interface after treatment with each of the four surface modification methods are shown in **Figure 2-5**. The NaCl-seeded Grignard method (**Figure 2-5-A** and **Figure 2-6-A**) produces a layered nanostructure displaying strong lattice fringes and thereby indicating high crystallinity; however, the small quantity of these nanostructures makes them difficult to observe in powder XRD.[85] The solvothermal method (**Figure 2-5-B** and **Figure 2-6-B**) produces crystalline nanostructures that are less well ordered than those produced by the Grignard method, but are observed to be a layered material with 0.72 nm and 1.9 nm spacing between the layers as determined by the Fourier transform (**Figure 2-7**). The nanostructures were imaged as quickly as possible to reduce dehydroxylation under the electron beam; however, some beam damage may have occurred. Grignard and solvothermal modification methods both lead to gaps of several nanometers at the zeolite/metal hydroxide interface. The gap between the nanostructures seen in the TEM images in **Figure 2-5** and the zeolite surface strongly suggests that the nanostructures are nucleated in solution near the zeolite surface and subsequently deposit on the surface of

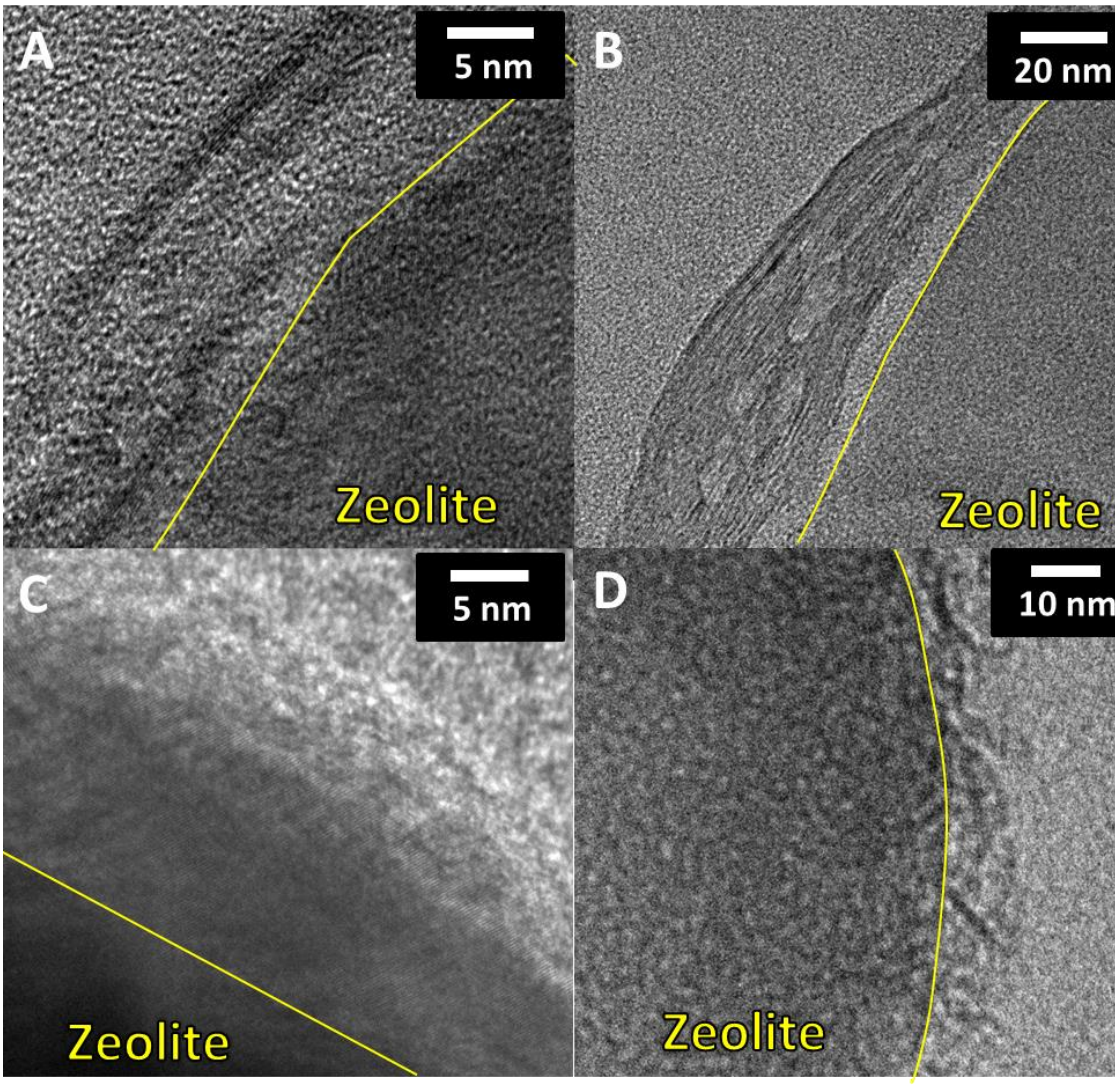

Figure 2-5. Intermediate-resolution transmission electron micrographs of nanostructures produced by a) Grignard, b) solvothermal, c) modified solvothermal, and d) ion exchange methods. The yellow line demarcates the border between zeolite and nanostructures. [84]

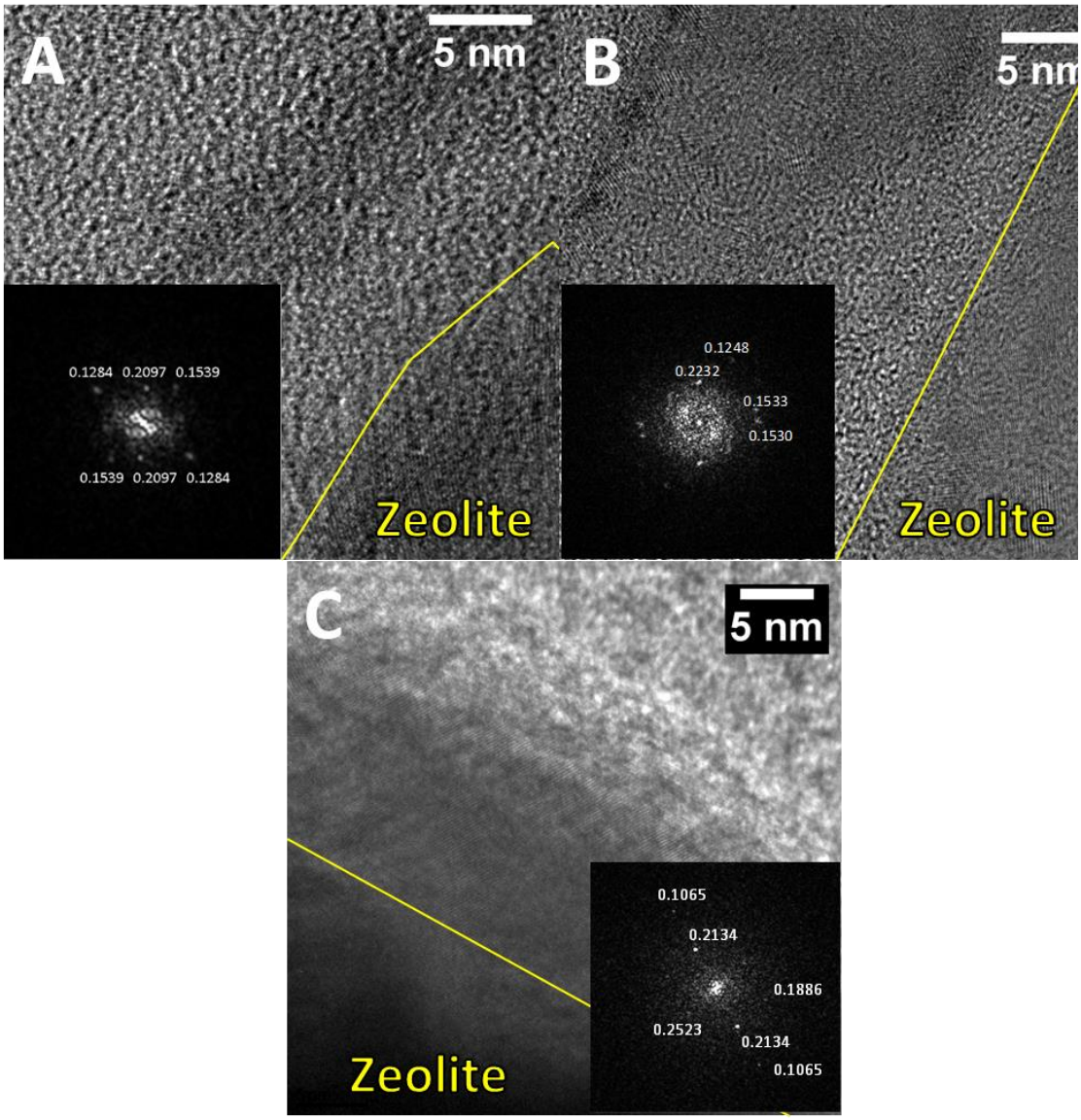

Figure 2-6. HRTEM images of A) Grignard, B) solvothermal, and C) modified solvothermal functionalized LTA and the Fourier transform of the functionalization highlighted by the white rectangle. The text is the corresponding d-spacing for each observable point. The yellow line demarcates the border between zeolite and nanostructures. [84]

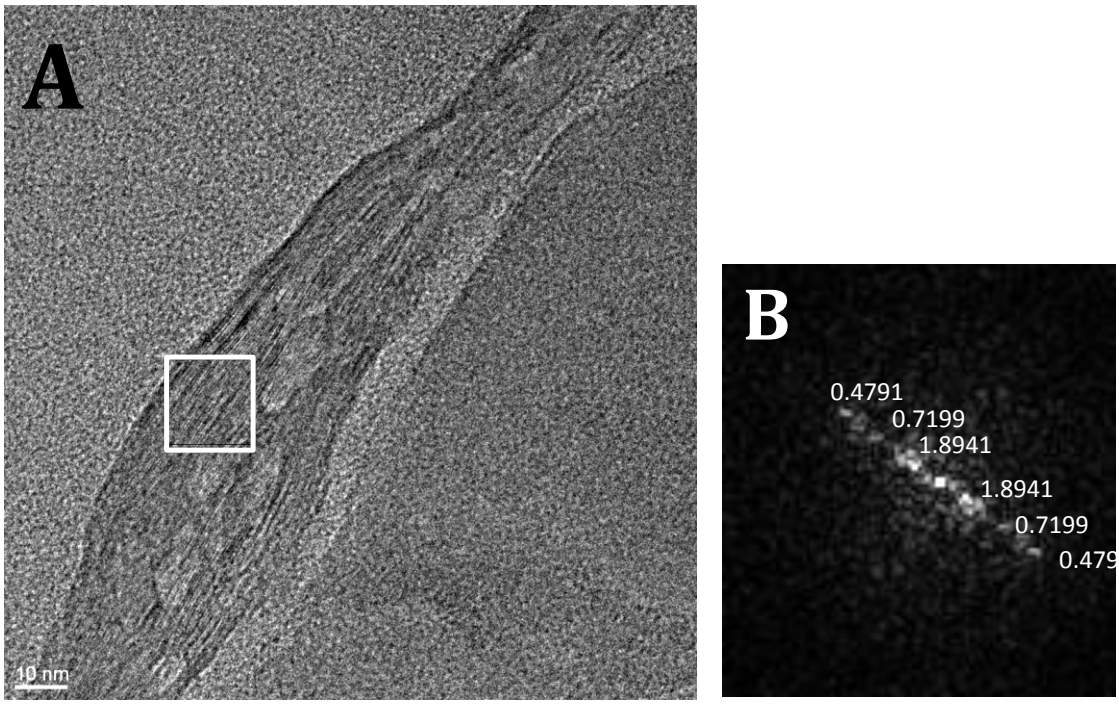

Figure 2-7. (A) HRTEM of Solvothermal functionalized LTA showing layered material (B) Fourier transform of functionalization generated from rectangle on the left image. The text is the corresponding d-spacing for each observable point. [84]

the zeolite, rather than growing directly from the surface. This will likely have an adverse impact on the strength of attachment of the nanostructures to the zeolite surface that may affect subsequent membrane processing steps. Additionally, it may create non-selective paths for molecular diffusion in a membrane and thus, lower its selectivity. The modified solvothermal method forms a relatively thick (10-40 nm) continuous, sheet-like nanostructure **(Figure 2-5-C** and **Figure 2-6-C**) that appears mainly amorphous with small crystalline domains also present. The crystalline areas were not significant enough to be observed clearly in XRD patterns. The ion exchange method produces a fine coverage of surface structures (**Figure 2-5**). No lattice fringes could be detected - even when imaged immediately to preclude any possibility of beam damage - suggesting that this method produced noncrystalline nanostructures. Both the modified solvothermal and

the ion exchange methods exhibited excellent adhesion to the LTA with no gaps at the interface. In fact, nanostructures produced by the ion exchange method penetrated into the LTA **(Figure 2-8**). These observations strongly indicate that these nanostructures were grown directly on the surface, leading to a higher expected strength of attachment between nanostructure and zeolite as well as the need for a substantially smaller quantity of roughening material than in the case of the Grignard and solvothermal methods. The Fourier transforms clearly demonstrated the crystalline nature of the surface materials produced by the solvothermal, modified solvothermal, and Grignard methods. The surface materials produced by the NaCl seeded Grignard and modified solvothermal methods both showed a *d*-spacing of 0.21 nm that is characteristic of MgO and not found in $Mg(OH)_2$ **(Figure 2-6-A**, **Figure 2-6-C**, and **Table 2-1**[86,87]). The crystalline material formed by the solvothermal method indicated two distinct *d*-spacings near 0.15 nm that are characteristic of $Mg(OH)_2$ (**Figure 2-6-B** and **Table 2-1**). The HRTEM

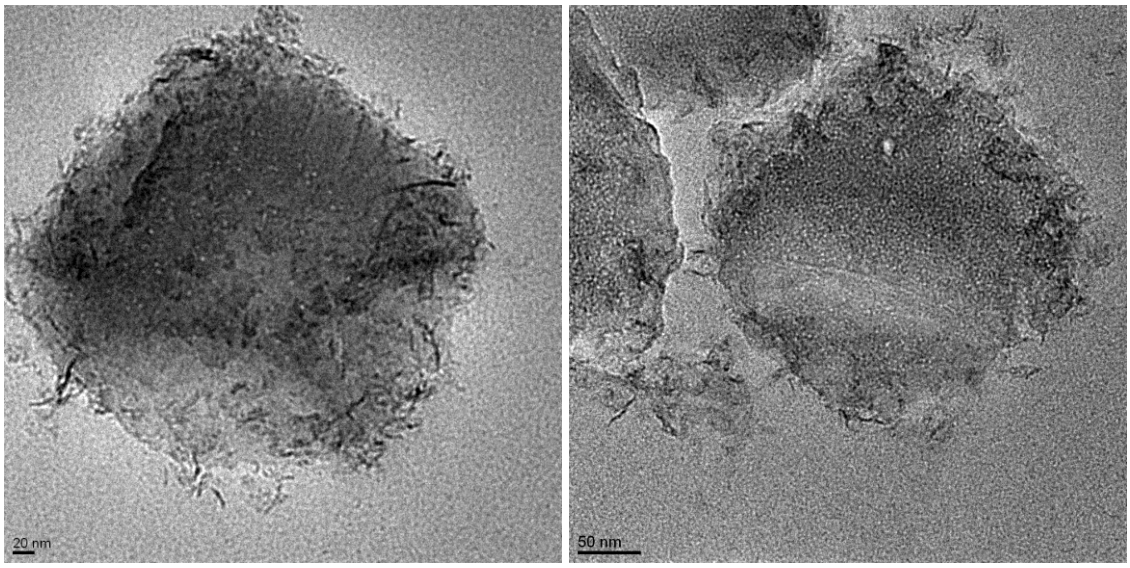

Figure 2-8. TEM images showing example of an ion exchange functionalization penetrating into the zeolite. [84]

findings were, therefore, generally consistent with the powder XRD patterns, but allow a much more detailed and conclusive understanding of the morphology, structure, and attachment of the surface materials produced by the four techniques.

Table 2-1. MgO and $Mg(OH)_2$ properties. [86,87]

$Mg(OH)_2$ [86]				**MgO** [87]			
h	**k**	**l**	**d(Å)**	**h**	**k**	**l**	**d(Å)**
0	0	1	4.77	1	1	1	2.43
1	0	0	2.73	0	0	2	2.11
1	0	1	2.37	0	2	2	1.49
1	0	2	1.79	1	1	3	1.27
1	1	0	1.57	2	2	2	1.21
1	1	1	1.49	0	0	4	1.05
1	0	3	1.37				
2	0	0	1.36				
2	0	1	1.31				
0	0	4	1.19				
2	0	2	1.18				

2.3.1.3 Elemental Composition of Nanostructures

Next, the compositions of the surface nanostructures were studied using three different techniques that probe different length scales: elemental analysis (EA) for bulk analysis, energy dispersive X-ray (EDS) spectroscopy for microscale analysis (based on the μm-mm spread of the beam), and X-ray photoelectron spectroscopy (XPS) for nanoscale analysis (~5-40 Å from the surface[88]). An abridged version of the significant composition analysis data is shown in **Table 2-2**, and the full set of data is presented in **Table A-1.** All three analysis methods showed that the five types of LTA particles (bare and modified) have similar Al/Si ratios, suggesting that no significant change in the

composition of the zeolite (e.g., dealumination) occurs during the surface modification process. The XPS measurements show more variation in Al/Si ratios because of the small integrated peak areas for these two components. The Mg content varies in the order: solvothermal > modified solvothermal > Grignard > ion exchange. The XPS data show the same trend for Mg content as the EA and EDS data. Since XPS is a surface characterization technique, the amount of Mg measured is higher than by EA and EDS, thereby confirming the Mg-rich nature of the surface structures. XPS data also can be used to show the relative 'material efficiency' of the modification methods and assess the economical use of reagents. The solvothermal method used the most Mg **(Table 2-2**) and demonstrated relatively poor nanostructure formation and a secondary phase (**Figure 2-2**

Table 2-2. Atom % values of Ca-exchanged LTA and modified-LTA samples measured EA, EDS, and XPS and normalized to Si value to be compared across methods. XPS values are for Na-exchanged samples.[84]

		EA	EDS	XPS
		Atom % normalized to Si		
LTA	**Mg**	-	0.0	0.0
	O	-	7.8	2.3
	Al	0.9	0.9	0.5
Grignard	**Mg**	0.2	0.1	1.1
	O	-	7.9	4.1
	Al	0.9	0.9	0.8
Solvothermal	**Mg**	0.7	0.9	3.8
	O	-	8.8	9.4
	Al	0.9	1.0	1.3
Modified Solvothermal	**Mg**	0.3	0.3	1.6
	O	-	7.3	6.4
	Al	0.9	0.9	1.1
Ion Exchange	**Mg**	0.1	0.1	0.2
	O	-	7.0	3.5
	Al	0.9	0.9	1.0

and **Figure 2-3**). The ion exchange method used the least amount of Mg, produced no magnesium-containing byproducts in the bulk solution, and formed highly adhered nanostructures (**Figure 2-5-D** and **Figure 2-8**) showing that it is a highly efficient functionalization method. Their composition was probed further using EDS mapping to determine if there could be another elemental component to the nanostructures to justify the nice coverage and low Mg-presence.

In general, the bulk characterization showed no significant dealumination for any functionalization method, although the values are not very precise. Nevertheless, on a local scale, EDS mapping (**Figure 2-9**) revealed that there is dealumination occurring at the edge of the ion exchange functionalized zeolite. This figure shows two things. Firstly, the quantity of alumina goes down before the edge of the zeolite showing dealumination. Secondly, the alumina level is fairly constant from the dealuminated zeolite through the nanostructures. This suggests that the displaced alumina from the zeolite may be combining with the Mg to form an $AlMgO_xH_y$ composite nanostructure rather than the MgO_xH_y nanostructures evident in the other methods. This also provides an explanation for the good coverage of nanostructures with a very low Mg composition.

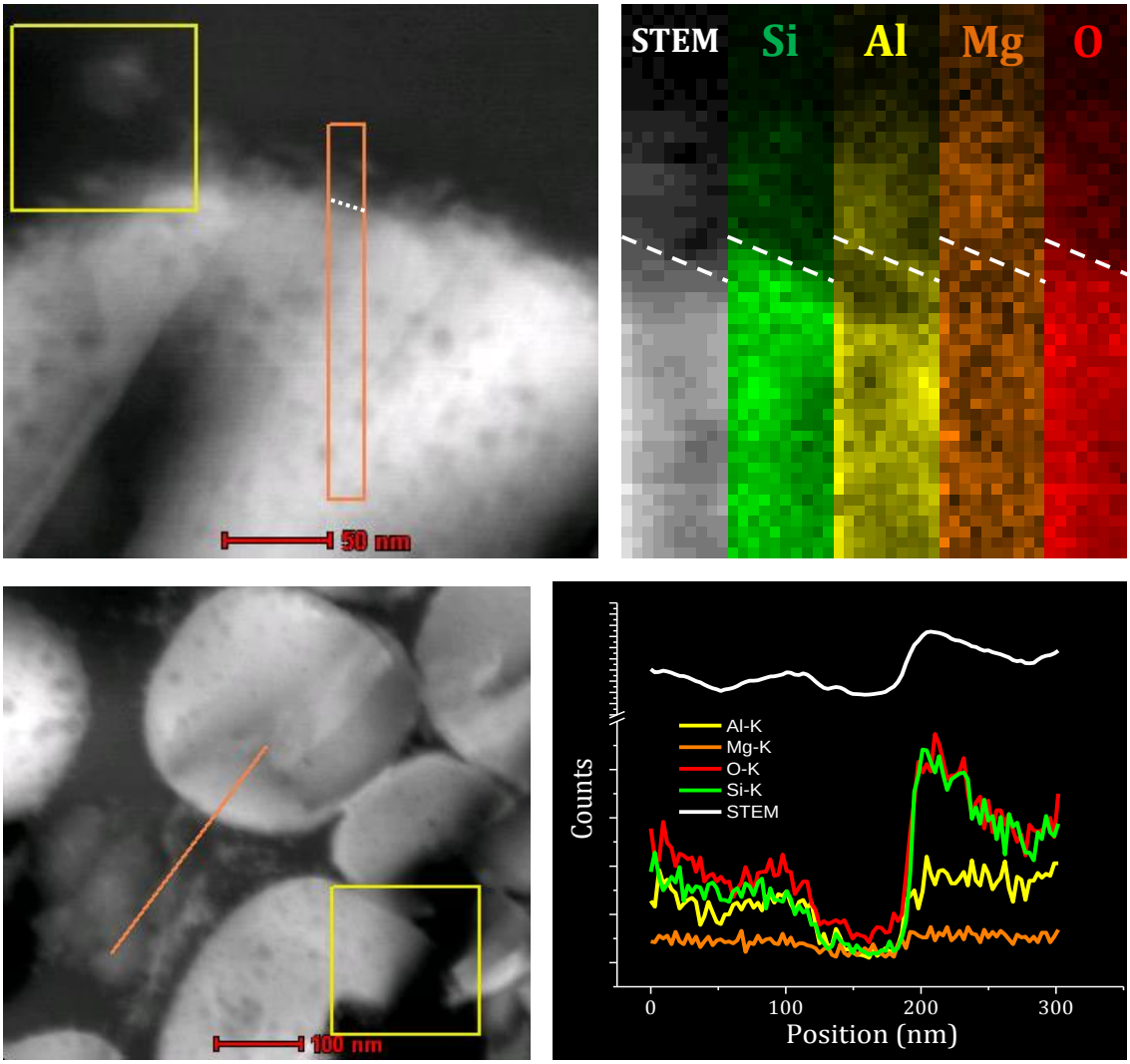

Figure 2-9. EDS mapping and line profiles in STEM mode of the edge of ion exchange functionalized LTA. All measurements represent the K-edge energy.

2.3.1.4 Porosity and Surface Area

To investigate the effect of the surface nanostructures on the accessibility of the zeolite micropores to gas molecules and the surface roughness, nitrogen adsorption isotherms were measured for the bare and surface modified particles. Adsorption data and calculated physical properties were normalized to the Si content (obtained from elemental analysis), and are shown in **Table 2-3** and **Figure 2-10**. The adsorption isotherms are of Type I, representing LTA as a microporous material. The LTA remained microporous after functionalization by all methods. The BET surface area increases in the order of modified solvothermal < solvothermal < ion exchange < Grignard < bare LTA. Since the BET surface area is influenced by any blockage of the pores and has also been shown to be inaccurate for microporous materials,[89] this analysis method is not representative of the actual surface roughening for these materials. The *t*-plot method is more useful in estimating the external surface area and hence the roughness of the surface.[90] Using this method, the external surface area increases in the order of Grignard < bare LTA <

Table 2-3. Surface area and micropore volume of LTA and modified-LTA materials, obtained from nitrogen physisorption isotherms and expressed per gram of Si. These values can be converted to cm^2/g zeolite *via* a conversion factor of ~6.15 g zeolite/g Si. [84]

Sample	BET Surface Area (m^2/g Si)	*t*-plot external Surface Area (m^2/g Si)	*t*-plot Micropore Volume (cm^3/g Si)
Bare LTA	3610	109	1.40
Grignard	3260	102	1.26
Solvothermal	2230	185	0.82
Modified Solvothermal	958	133	0.33
Ion Exchange	3020	191	1.13

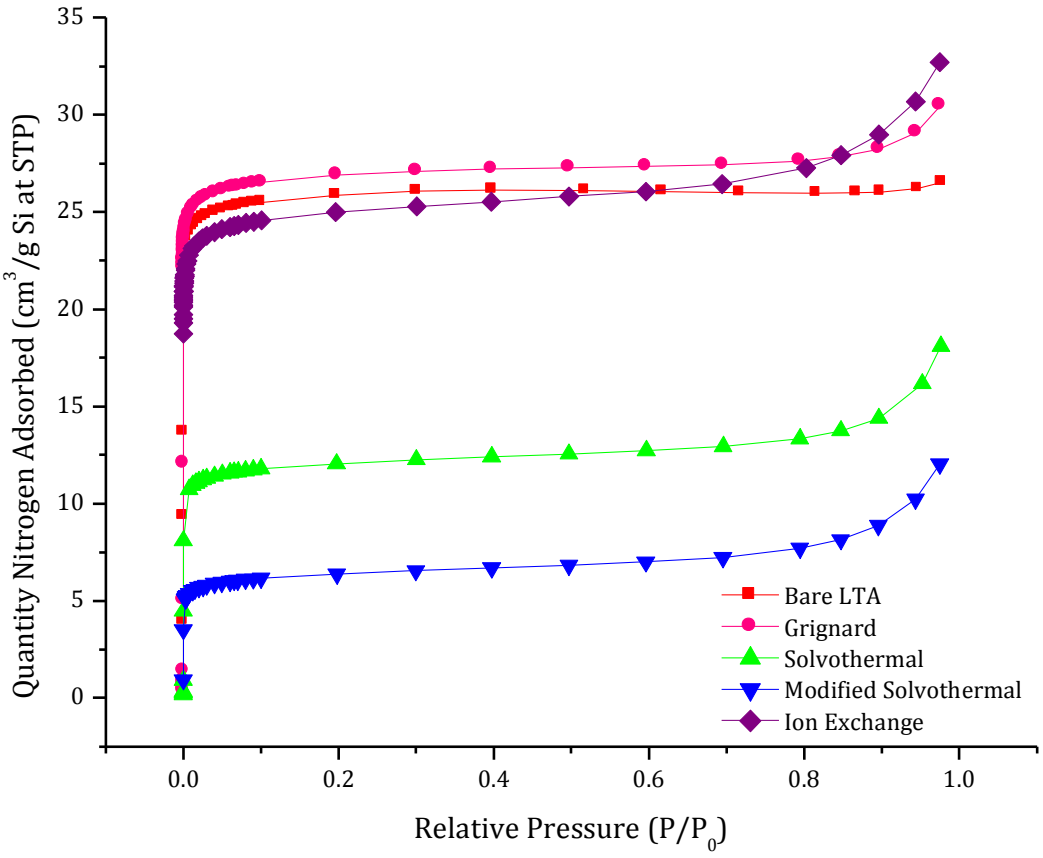

Figure 2-10. Nitrogen adsorption isotherms for 300 nm Ca-exchanged the four functionalized LTA particles; all normalized to the Si content obtained from elemental analysis. These values can be converted to cm^2/g zeolite *via* a conversion factor of ~6.15 g zeolite/g Si. [84]

modified solvothermal < solvothermal < ion exchange method. Since the ion exchange method produces fine, rod-like nanostructures there is significantly more surface roughening than when the other methods are used. The solvothermal method creates the second highest external surface area. However, because of the existence of an impurity (byproduct) phase, the increase in surface area cannot be fully attributed to the roughening of the zeolite surface. In the literature, it is hypothesized that higher roughness leads to better adhesion of the particles with polymers in composite

membranes[26] and therefore the ion exchange method should show the best adhesion properties.

The micropore volumes of the modified LTA materials vary considerably. The solvothermal and modified solvothermal methods cause severe pore blocking effects (**Table 2-3**). The dense layers deposited on the surface, as well as the surface-modification process, may block the diffusion of gases into the pores. The micropore volumes of the materials created by the ion exchange and Grignard methods are somewhat lower than that of bare LTA but do not indicate severe pore blocking. Pore blockage is clearly important in the use of the modified particles for MMM fabrication. Thus, the solvothermal-based methods for modifying LTA are less promising because of the large reduction in micropore accessibility.

2.3.2 Surface Nanostructures on Pure-silica Zeolite MFI

A parallel study was conducted on pure-silica MFI *via* the same functionalization methods as used for LTA with the exception of the ion exchange method, which cannot be carried out on pure-silica zeolites due to the lack of charge-balancing cations in the structure.

2.3.2.1 Nanostructures

X-ray diffraction showed that the MFI structure was also maintained after functionalization (**Figure 2-11**). XRD shows no evidence of a secondary crystal phase after any of the three modification processes. SEM and TEM investigations (summarized in **Figure 2-12** and **Figure 2-13**, respectively) indicated similar structures produced on MFI by the Grignard method as on aluminosilicate LTA. However, the nanostructures

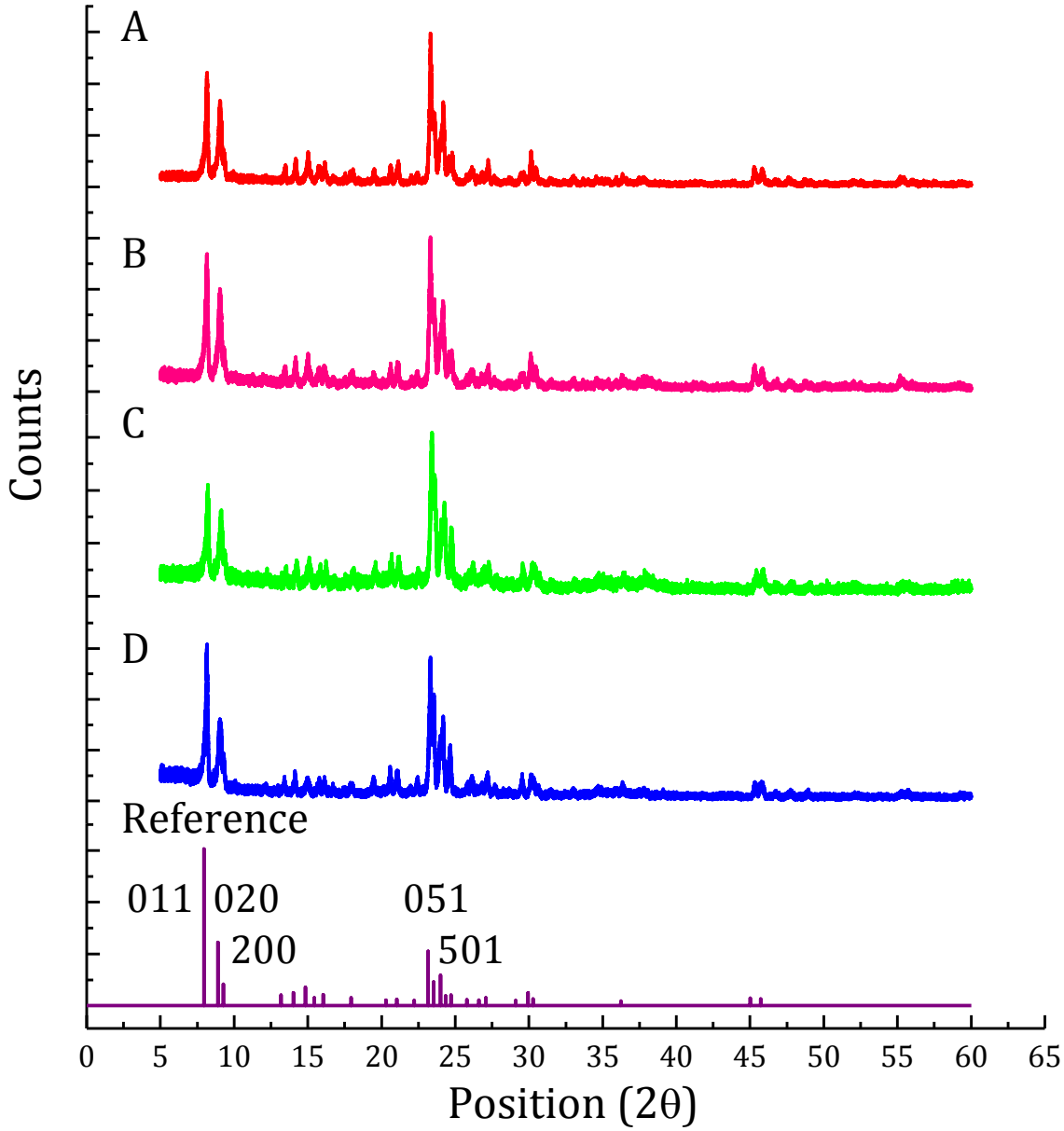

Figure 2-11. X-ray diffraction patterns of (A) unmodified 300 nm MFI particles, and after modification by (B) Grignard, (C) solvothermal, and (D) modified solvothermal methods. [84]

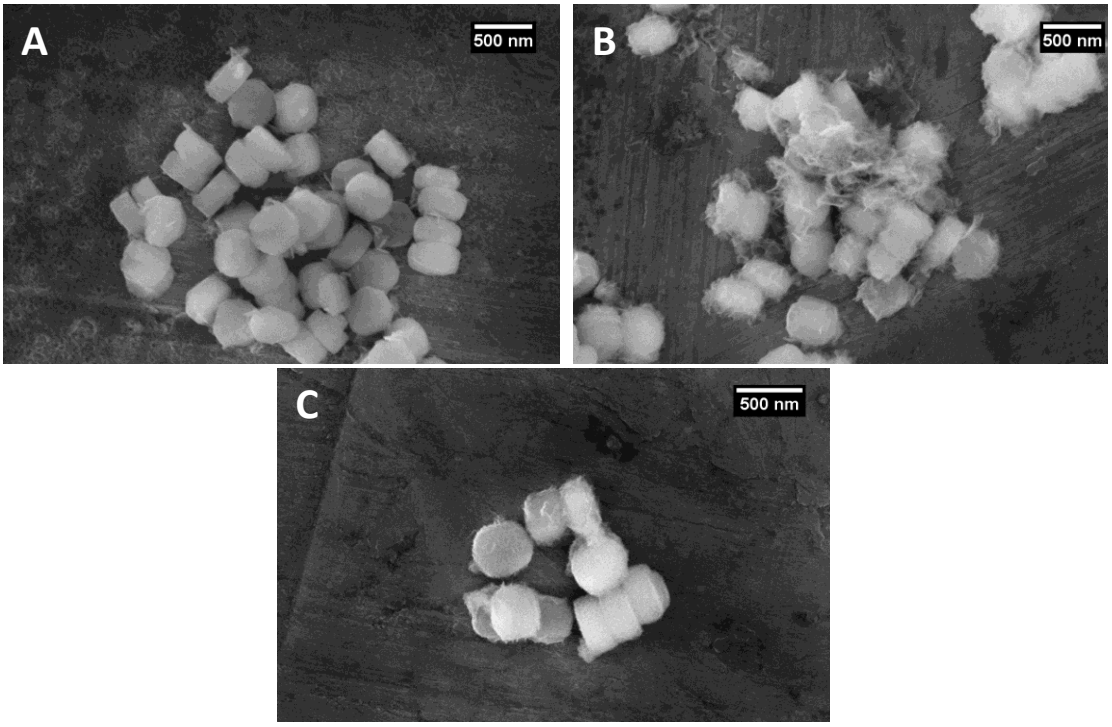

Figure 2-12. Scanning electron microscopy images of (A) Grignard, (B) Solvothermal, and (C) Modified solvothermal functionalized MFI. [84]

formed by the other two methods show slight differences in their appearance on MFI as compared to LTA. As described earlier, the solvothermal method on LTA generated layered nanostructures that are not attached to the zeolite surface. A somewhat different structure was produced on the surface of MFI (**Figure 2-13-B**). Since the surface structure and surface potentials of the aluminosilicate LTA and pure-silica MFI are expected to be quite different,[91,92] the above observations for the solvothermal method indicate that the zeolite surface properties may significantly impact the morphology of nanostructures formed. The different results obtained from the Grignard method after the thionyl chloride pre-treatment method[30,35] compared to the NaCl seeding method may also be explained by the difference in LTA surface characteristics resulting

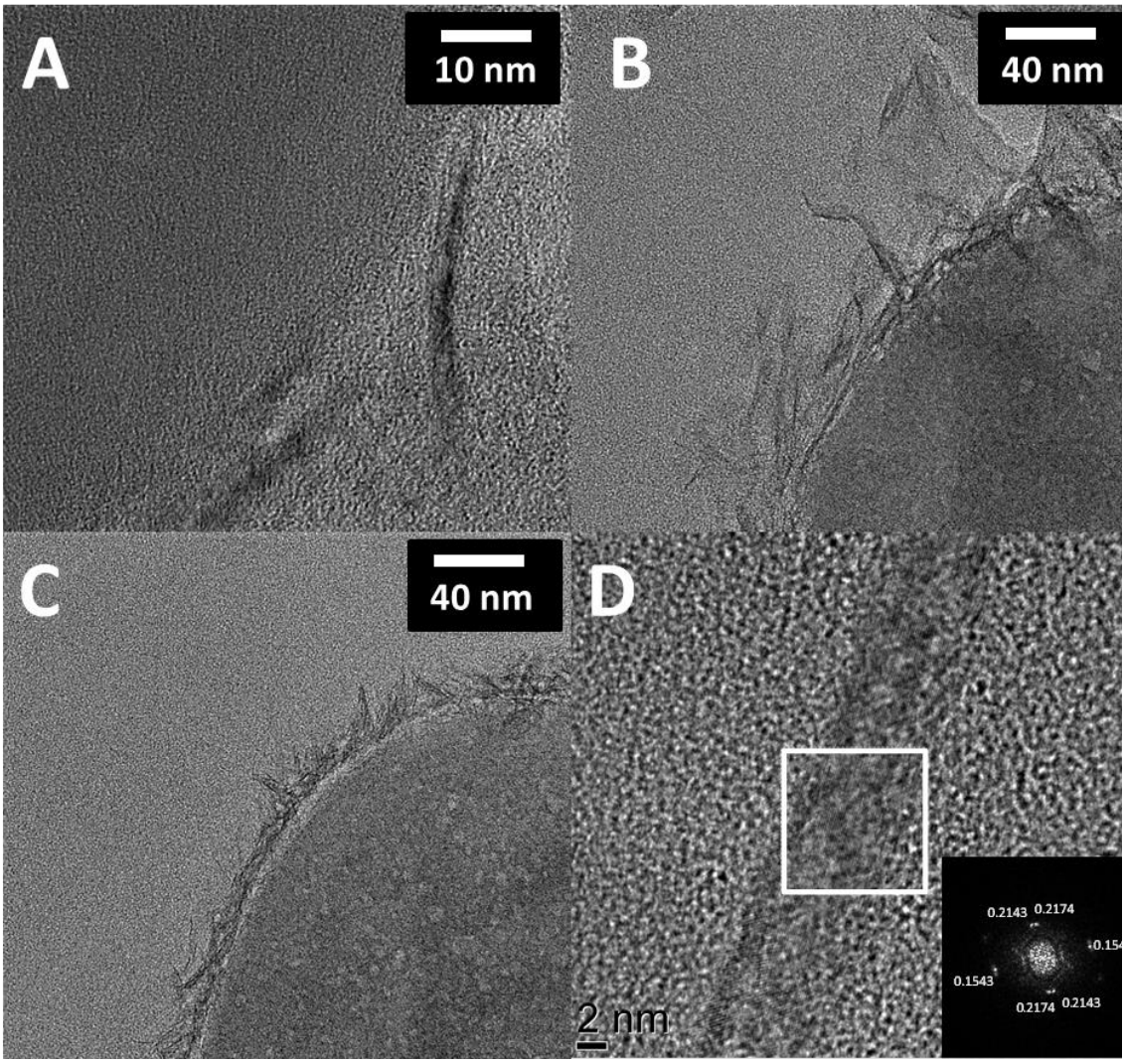

Figure 2-13. TEM images of (A) Grignard, (B) Solvothermal, and (C) Modified-solvothermal functionalized MFI; and (D) HRTEM of Grignard nanostructure on MFI with Fourier transform (inset) of the area in the white rectangle. The corresponding *d*-spacings are shown for each observable point in the Fourier transform. [84]

from pre-treatment conditions. The modified solvothermal method on MFI (**Figure 2-13-C**) produced surface structures similar to those observed on LTA; however, an important difference is the emergence of a larger nanoscopic gap between the surface structures and the zeolite MFI surface as observed by TEM. The substitution of EDA with DETA caused fundamental changes in the nanostructure formation on the zeolite surfaces.

Hence, we refer to the two methods separately throughout this work, although they are both carried out by solvothermal reactions.

2.3.2.2 Elemental Composition of Nanostructures

The elemental composition for MFI functionalization (**Table 2-4**), showed the same trends as LTA where the solvothermal method has the most Mg present in the sample and the Grignard has the least.

Table 2-4. Elemental composition of bare and functionalized MFI samples by EDS and XPS. [84]

		EA	EDS	XPS	EA	EDS	XPS	EA	EDS	XPS	EA	EDS	XPS
			Wt %			Wt % normalized to Si			Atom %			Atom % normalized to Si	
MFI	**Mg**	x	0.1	0.0		0.0	0.0	x	0.0	0.0	x	0.0	0.0
	O	x	74.0	47.7	x	2.8	0.9	x	83.3	17.2	x	5.0	1.6
	Si	34.0	26.0	52.3	1.0	1.0	1.0	94.9	16.7	10.8	1.0	1.0	1.0
Grig.	**Mg**	2.1	2.5	12.7	0.1	0.1	0.3	6.3	1.9	9.4	0.1	0.1	0.4
	O	x	73.3	49.5	x	3.0	1.3	x	82.6	55.9	x	5.3	2.3
	Si	35.3	24.2	37.8	1.0	1.0	1.0	89.2	15.5	24.3	1.0	1.0	1.0
Solvo.	**Mg**	6.4	7.9	32.9	0.3	0.4	1.5	21.4	5.9	24.0	0.3	0.4	1.7
	O	x	70.7	44.6	x	3.3	2.0	x	80.2	49.4	x	5.8	3.5
	Si	25.3	21.3	22.5	1.0	1.0	1.0	73.3	13.8	14.2	1.0	1.0	1.0
Mod. Solvo.	**Mg**	3.5	5.9	43.2	0.1	0.2	2.1	11.5	4.5	37.2	0.1	0.3	2.5
	O	x	68.4	36.5	x	2.7	1.8	x	78.7	47.7	x	4.7	3.2
	Si	29.5	25.7	20.3	1.0	1.0	1.0	83.4	16.8	15.1	1.0	1.0	1.0

2.3.2.3 Porosity and Surface Area

Nitrogen physisorption analysis (**Table 2-5** and **Figure 2-14**) displayed similar overall trends in the degree of pore blocking using the various methods on MFI, in comparison to the modified-LTA samples. Both solvothermal methods show less

nitrogen adsorption in cm^3/g Si in the isotherms (**Figure 2-14**) and over 30% reduction in

Table 2-5. Surface area and micropore volume of MFI and modified-MFI materials, obtained from nitrogen physisorption isotherms and expressed per gram of Si. These values can be converted to cm^2/g zeolite *via* a conversion factor of 2.14 g zeolite/g Si. [84]

Sample	BET Surface Area (m^2/g Si)	*t*-plot external Surface Area (m^2/g Si)	*t*-plot Micropore Volume (cm^3/g Si)
Bare MFI	1430	306	0.45
Grignard	1510	344	0.47
Solvothermal	1100	340	0.31
Modified solvothermal	966	447	0.21

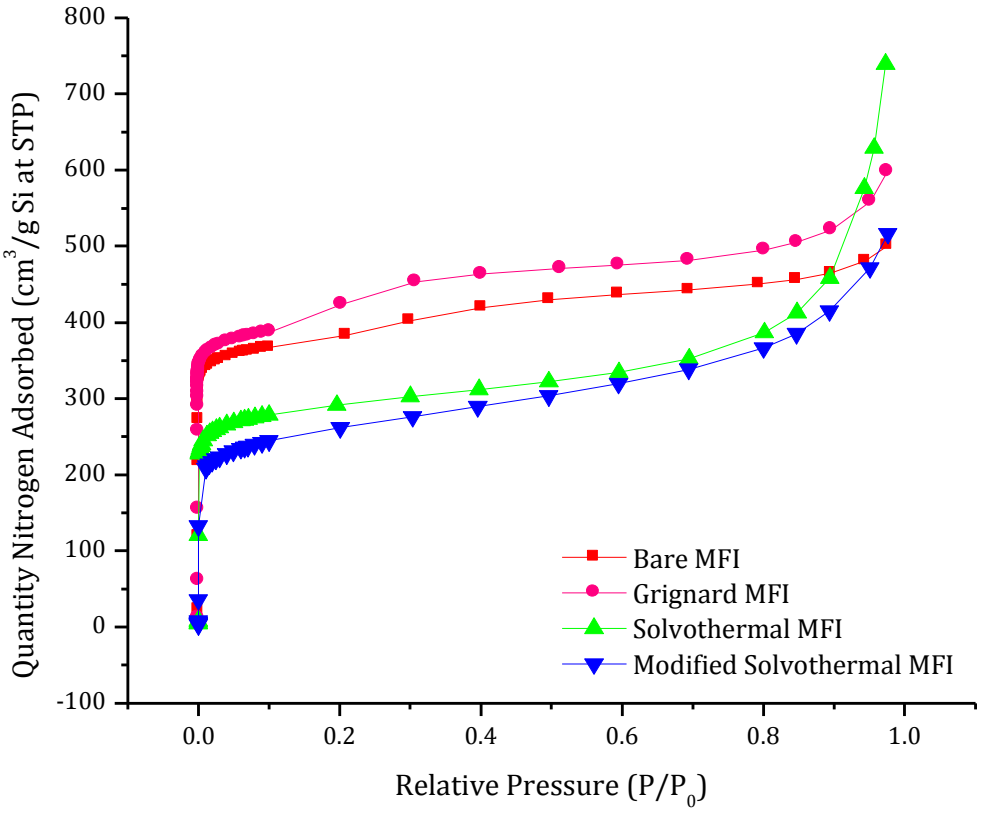

Figure 2-14. Nitrogen physisorption isotherms of bare and functionalized MFI normalized to the weight% of Si by EDX. These values can be converted to cm^2/g zeolite *via* a conversion factor of 2.14 g zeolite/g Si. [84]

t-plot micropore volumes. The modified solvothermal method created roughened MFI particles with the highest external surface area, as evaluated from the *t*-plot method.

Pore blocking of particles caused by the modified solvothermal method was studied further to understand the mechanism of blocking and whether the solvent or the nanostructures were the primary cause. The modified solvothermal functionalization, which showed the most pore blocking of the methods, was carried out on LTA and MFI zeolites with and without magnesium. In LTA, pore blocking occurred as a combined effect due to the solvent and nanostructures where the pores were blocked about equally by each component (**Table 2-6**). MFI showed significant pore blocking due to the solvent, but no additional pore blocking after functionalization with Mg **(Table 2-7**). This difference in pore blocking behavior is due to the pore size of the zeolites, with LTA

Table 2-6. T-plot porosity and surface area of LTA functionalized with the modified solvothermal method with and without Mg.

	Micropore volume (cm^3/g)	**T-plot surface area (m^2/g)**
Ca ex. LTA	0.21	12.8
Ca. ex. Mod. Solvo. LTA without Mg.	0.16	10.7
Ca ex. Mod. Solvo. LTA	0.09	50.1

Table 2-7. T-plot porosity and surface area of MFI functionalized with the modified solvothermal method with and without Mg.

	Micropore volume (cm^3/g)	**T-plot surface area (m^2/g)**
MFI	0.20	16.8
Mod. Solvo. MFI without Mg.	0.12	18.6
Mod. Solvo. MFI	0.13	26.7

having a smaller pore size of 4 Å than MFI (5.5 Å).[24] The probing molecule in this measurement is N_2 which has a kinetic diameter of ~3.6.[80] Because the LTA pore size is much closer to the N_2 diameter, the amount of pore blocking necessary to render the micropore inaccessible is much less than in MFI, which has a large enough pore diameter that the Mg nanostructures are less likely to block the accessibility. Furthermore, because of the charged and hydrophilic nature of LTA, Mg^{2+} cations or small, charged MgO_xH_y intermediates may adsorb to the framework and inside the pores causing additional pore blocking. This last factor also contributes to the difference in surface structure adhesion to the zeolite that was shown previously: the LTA has nanostructures that are closer to the zeolite than in the MFI where it appears that there is a gap between the materials.

2.4 Conclusions

A multiscale experimental study of the structural, compositional, and morphological characteristics of MgO_xH_y-modified zeolite materials has been presented, and the value of this characterization in assessing the suitability of such materials in the fabrication of mixed-matrix membranes (MMMs). The four functionalization methods studied in this work produce surface nanostructures that may appear superficially similar under SEM observation, but in fact differ considerably in shape, size, surface coverage, surface area/roughness, degree of attachment to the zeolite surface, and degree of zeolite pore blocking. The evaluation of these characteristics by the use of multiple techniques is summarized – both quantitatively and qualitatively – in **Table 2-8** (for LTA) and **Table 2-9** (for MFI) and allows for a rational selection of the method expected to result in the best enhancement of the desired properties. As indicated by **Table 2-8**, the ion exchange method shows the most promise for use in MMMs because of its increase in surface area,

lack of pore blocking, and well-attached nanostructures. Oppositely, the solvothermal methods do not appear to be very promising because of their significant pore blocking - rendering them inappropriate for use in MMMs.

Table 2-8. Summary of properties of surface nanostructures produced by four different surface modification methods on LTA. *All scale bars represent 100 nm except bare LTA which is 500. [84]

	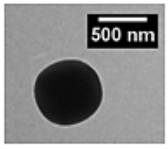 **Bare LTA**	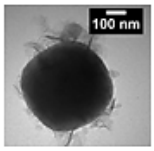 **Grignard**	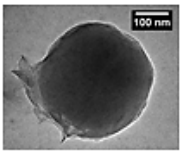 **Solvothermal**	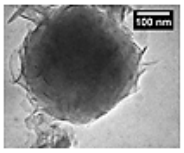 **Modified Solvothermal**	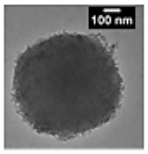 **Ion Exchange**
Thickness (nm)	N/A	0-120	0-100	10-40	20
T-Plot External Surface Area (m^2/g Si)	109	102	185	133	191
Micropore Volume (cm^3/g Si)	1.40	1.26	0.82	0.33	1.13
Mg Content	N/A	Low	High	High	Low
Crystallinity	N/A	Crystalline	Crystalline	Partial Crystallinity	Non-Crystalline
Attachment	N/A	Not attached to surface	Not attached to surface	Attached	Attached
Secondary Phase	N/A	No	Yes	No	No

Table 2-9. Summary of properties of surface nanostructures produced by three different surface modification methods on MFI. [84]

	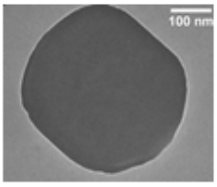	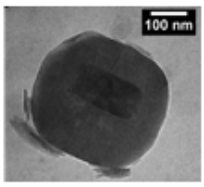	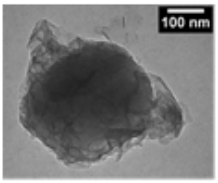	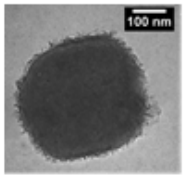
	MFI	**Grignard**	**Solvothermal**	**Modified Solvothermal**
Thickness (nm)	N/A	50-100	0-100	5-20
T-Plot External Surface Area (m^2/g Si)	306	344	340	447
Micropore Volume (cm^3/g Si)	0.45	0.47	0.31	0.21
Mg Content	N/A	Low	High	Moderate
Crystallinity	N/A	Crystalline	Non-crystalline	Non-crystalline
Attachment	N/A	Not attached to surface	Attached	Attached

3 Chapter 3: Morphological, mechanical, and natural gas separation properties of polyimide-based nanocomposite membranes containing functionalized LTA

3.1 Introduction

Mixed matrix membranes, consisting of an inorganic particulate phase dispersed in a polymer membrane matrix, have been identified as a potential route towards high-efficiency gas separations. They are able to combine the high selectivity of inorganic (*e.g.*, zeolite) materials with the processability of polymeric membrane materials.[6,12,18,20–22] However, during the fabrication of mixed matrix membranes (MMMs), poor adhesion between zeolite particles and the polymer matrix often occurs leading to a decrease in membrane performance.[28,29] It has been suggested that roughening the zeolite surface *via* deposition of inorganic nanostructures can improve zeolite-polymer adhesion. It was hypothesized that the roughened surface provides a larger area for polymer-zeolite interactions and reduces the need for polymer deformation to adhere to the zeolite surface.[26] To this end, four surface roughening methods have been developed including Grignard,[30,36] solvothermal and modified solvothermal,[21,22] and ion exchange[34,84] methods. A systematic characterization study of these four methods to determine their unique morphologies, nanostructure crystallinities, surface areas, porosities, and elemental compositions has been conducted and explained in Chapter 2.[84] This study allowed for a rational selection of the best functionalization method for use in this particular separations application based on the

consideration of several quantitative and qualitative structural and morphological parameters determined through experimental characterization.

The particle dispersion characteristics and mechanical properties of these membranes can have a significant influence on the stability and technological application of mixed matrix membranes but have received little attention in the literature and have previously been addressed in a qualitative fashion. This chapter will expand the knowledge of these properties and how they correlate to each other and the nanostructures used. Additionally, the CO_2/CH_4 gas permeation is measured as an industrially important application of these membranes. This data is used to probe the impact of functionalization on the membrane-zeolite interface and is compared with the dispersion and mechanical properties.

3.2 Methodology

3.2.1 Membrane Fabrication

Thoroughly characterized, Ca-exchanged functionalized zeolites were used from the previous chapter. These particles and Matrimid 5218® (Vantico) were dried in an oven prior to use. Chloroform (Sigma Aldrich) was chosen as the best solvent for this system based on DLS measurements and observation of flocculation of particles and polymer in a dilute solvent solution. These experiments will be expanded upon in section 3.3.1. Next, 0.05 g (0.1 g for 30 w/w%) dried zeolite was dispersed in chloroform using a sonication horn. The particles were primed by adding a dilute 10% w/w solution of 0.05 g Matrimid® in chloroform and the solution was sonicated again. The remaining polymer, 0.28 g, was added to the primed solution with stirring. The solution was stirred slowly overnight and chloroform was evaporated to produce a viscous polymer solution. The

membranes were cast using a 200 µm (prior to solvent evaporation) doctor's knife on a glass plate that had initially been treated with Glassclad®-18. The casting was done in a nitrogen-filled, chloroform-saturated glovebag to ensure a lack of moisture and slow solvent evaporation. The membranes were left in the bag overnight for the solvent to evaporate. The membranes were removed from the glass plate after drying by dropping DI water at the edges of the membrane which separates the membrane from the glass. The membranes were dried again overnight and annealed at 230°C for 16 hours to remove excess solvent in a vacuum oven.

3.2.2 Dynamic Light Scattering

Dynamic light scattering (DLS) samples were made by dispersing 0.05 g LTA in 10 mL of chloroform, dichloromethane (DCM), or tetrahydrofuran (THF). One set of samples was made with zeolite and solvent only and a second was made with zeolite, solvent, and 0.06 g Matrimid. The samples were sonicated with a sonication horn to disperse the particles in the solvent initially, and then resonicated in a sonication bath for ten minutes immediately prior to DLS measurement. The light scattering was measured using a Zetasizer Nano instrument and a quartz sample cuvette. The measurements were repeated three times per sample at room temperature.

3.2.3 Membrane Imaging

To make scanning electron microscopy (SEM) samples, the LTA-Matrimid® membranes were cryogenically fractured in liquid nitrogen, mounted vertically on a stub, gold coated for 60 s, and imaged using a LEO 1530 SEM. Transmission electron microscopy (TEM) samples were prepared by embedding the LTA-Matrimid® composite membranes in SPI-PON™ 812 epoxy in a BEEM capsule. The sharp point of the epoxy

capsule was microtomed into 70 nm slices using a Leica EM UC6 Ultramicrotome and a Diatome Ultra 35° diamond knife. 70 nm appeared to be the thinnest the samples were able to be sliced without causing significant damage to the integrity of the composite. The microtomed samples were caught in deionized water and adsorbed onto a carbon coated-copper grid. Extra water was wicked off with a paper towel and the samples were dried in a vacuum chamber. The samples were plasma treated under vacuum to remove surface contaminants and excess adsorbed water prior to use. TEM imaging was done using a FEI Tecnai F30 high resolution TEM at 300 kV.

3.2.4 Dispersion

A series of SEM images were taken from adjacent areas of the same mixed matrix membrane sample, and arranged together into images of dimensions of approximately 30 μm × 50 μm. This method allows observation of the fine detail of the particle dispersion while ensuring a large enough membrane image area to obtain a macroscopically reliable characterization of the particle dispersion. An example image is shown in **Figure 3-1-A**. Because of the presence of agglomerates and the lack of discrete contrast between the polymer and the particles, there was no possibility of automatic particle filtering or counting via an automated program. Therefore, the location of each particle had to be identified in the image and digitally marked with a black dot as shown in **Figure 3-1-B**. The SEM image was then converted into a binary image showing the spatial position of each particle by adjusting the contrast in the picture, applying a threshold filter to separate the particles from the other membrane features as shown in **Figure 3-1-C**, and images were saved in the .BMP form. All image manipulation was done using the program *ImageJ*.[93] The particle dispersion was assessed using a method (and

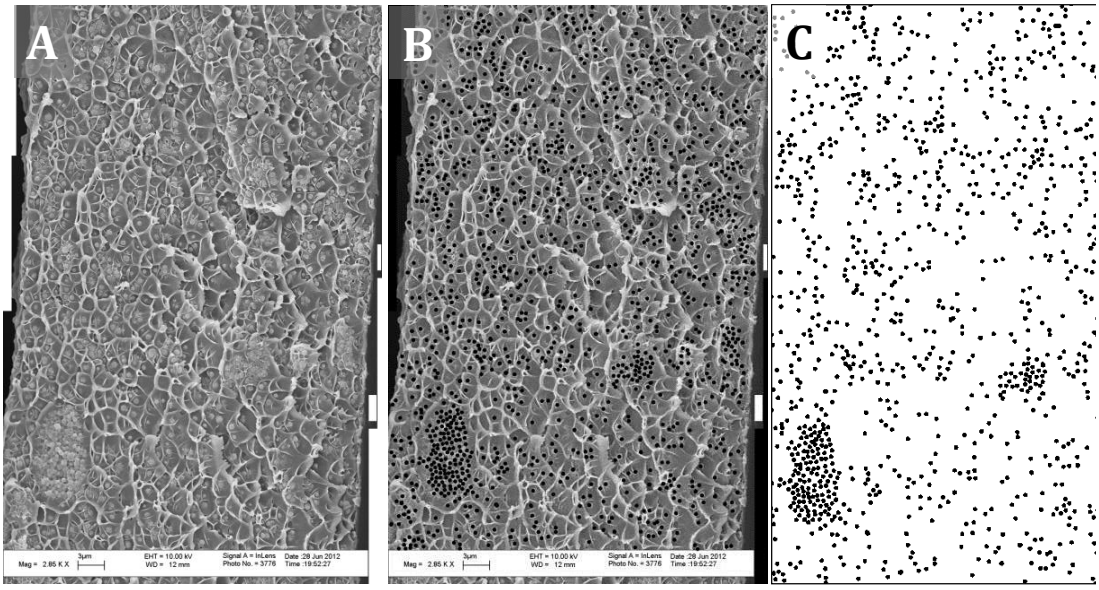

Figure 3-1. Process of marking particle location on the composite membranes.

corresponding Matlab code) developed by Khare and Burris[94] to determine the free space length (L_f) value of the membrane. The program was run with an initial characteristic square size guess of 10 microns and was performed with 10,000 iterations. This procedure was repeated ten times on each membrane to determine the computational error bars in the L_f assessment.

The free space length value, L_f, represents the largest square size where the statistical mode of the particle occurrence histogram equals to zero or, more simply, the largest square with the probability that there are no particles in a randomly placed square. Examples of the histogram produced by counting the particles present in each square for each iteration are shown in **Figure 3-2** from Khare and Burris.[94] Since the zeolite particle size is the same in all membranes and the weight loading is the same within each set of membranes (15 and 30 w/w%), larger (L_f) values correspond to a more aggregated

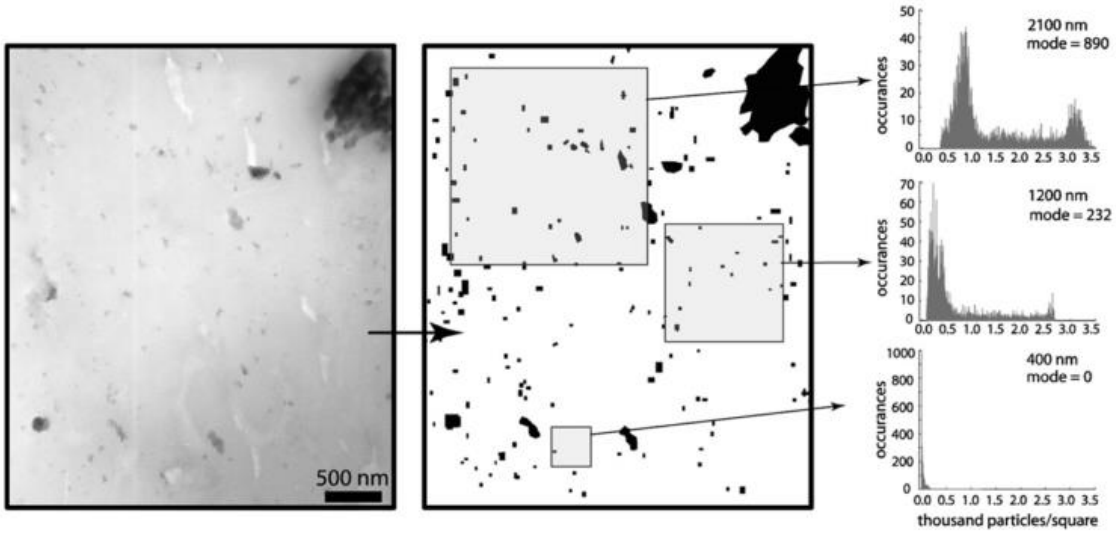

Figure 3-2. Illustration of the particle distribution histograms produced during each step of the Khare and Burris method.[94] The bottom histogram represents the final L_f size with a mode of 0.

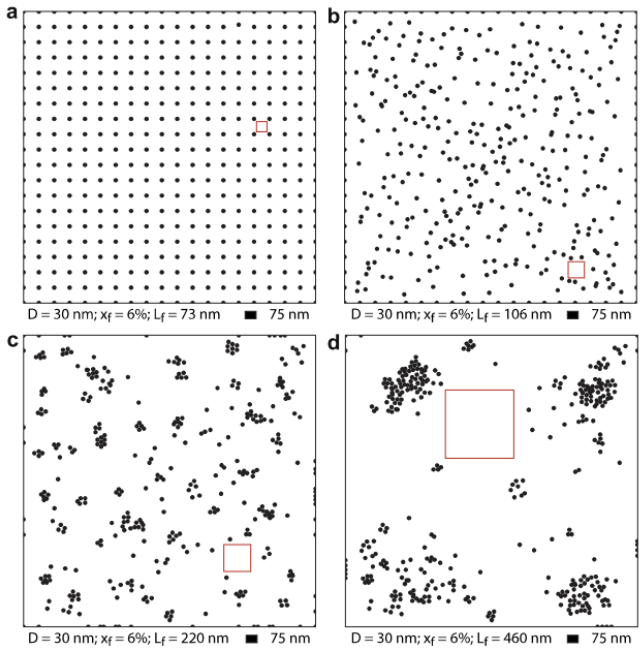

Figure 3-3. An illustration of L_f values (sizes) for several different levels of distribution/ agglomeration.[94]

and less well-dispersed zeolite phase and smaller values represent better particle distribution throughout the membrane as shown in the cartoon in **Figure 3-3**.[94]

3.2.5 Mechanical Properties

Nanoindentation samples for mechanical property measurements were made by fixing a 1 cm^2 section of the mixed matrix membrane (used in the gas permeation measurements) to a glass slide with a thin layer of Superglue and drying the sample overnight. In order to ensure the accuracy of the nanoindentation calculations of elastic modulus and hardness, the membranes had to be smooth relative to the size of the nanoindentation tip. Thus, before detailed measurement of the sample with nanoindentation, the sample roughness was determined using scanning probe microscopy (SPM). SPM measurements were conducted on a Dimension 3100 instrument equipped with an Arrow–NCR silicon cantilever that had a tetrahedral tip with a height of 10 - 15 μm and typical tip radius of curvature < 10 nm.[95] The surface roughness (R_q) was determined from the SPM height images. Only samples with R_q < 20 nm were used for nanoindentation measurements. Initially the MMMs had a surface roughness significantly higher than this threshold value ranging from R_q= 50-130 nm with the exception of the pure polymer that was smooth enough to use as made. The samples were polished using Ted Pella diamond pastes in the following order of grain sizes: 3 μm, 1 μm, and 0.25 μm for approximately 10 minutes each to smooth the surface and the sample was reimaged by SPM. This procedure was repeated until the samples met the criteria of R_q < 20 nm. SPM images of the as made membranes and the final polished membranes are shown in **Figure 3-4**.

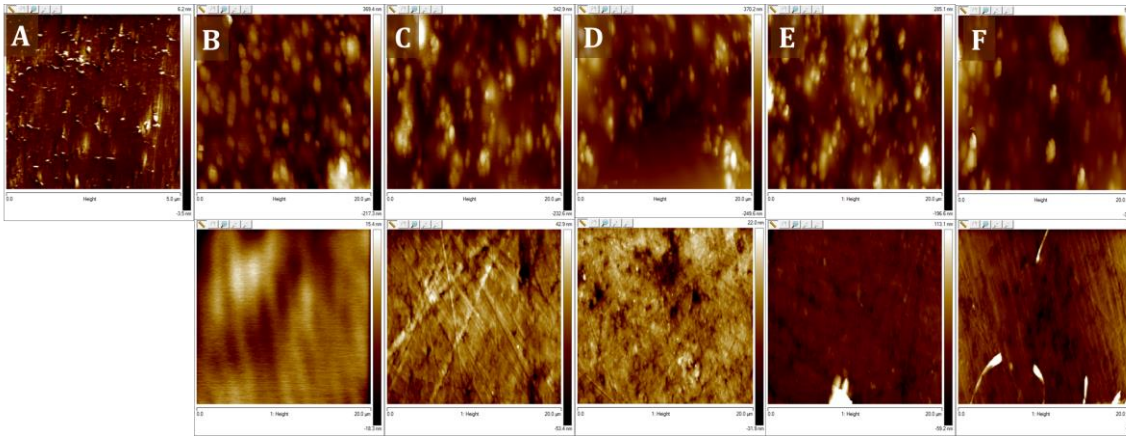

Figure 3-4. Scanning probe microscopy images of the surface roughness before polishing (top row) and after polishing (bottom row) of composite membranes fabricated with A) no filler, B) bare LTA, and LTA functionalized with the C) ion exchange, D) modified solvothermal, E) original solvothermal, and F) grignard methods.

The reduced elastic modulus and hardness were measured using a Hysitron TI 900 Triboindenter with a Berkovich pyramidal tip (approximate tip curvature of 100-200 nm and a total included angle of 142.3° [96]) and calculated according to the Oliver and Pharr method for nanoindentation.[97] The basic mechanism of nanoindentation involves applying a force to a probe and indenting a sample where the sample undergoes elastic and plastic deformations. The nanoindentation measurement indents into the sample to a depth of h under an applied load. After nanoindentation, the tip is pulled away to leave a residual imprint of h_f that indicates the plastic deformation. h_c represents the elastic deformation where $h_c = h - h_f$. This indentation motion and the resulting variables are illustrated in **Figure 3-5**. The data measured during the experiment takes the form of a force-depth curve shown in **Figure 3-6**. Parameters extracted from

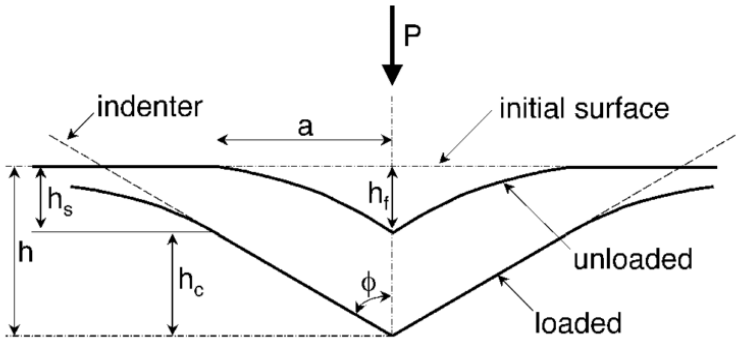

Figure 3-5. Diagram of parameters during a nanoindentation experiment.[97]

this curve are used to calculate the reduced elastic modulus of the membrane samples by **equation (4.1)**:

$$E_r = \frac{S\sqrt{\pi}}{2\sqrt{A}} \tag{4.1}$$

where S is the stiffness or the rate of change in the load over the change in height ($S = \frac{dP}{dh}$) during tip withdrawal and A is the contact area of the tip. The contact area is obtained by the area function calibration equation explained in the next paragraph. The hardness was determined by **equation (4.2)**:

$$H = \frac{P_{max}}{A} \tag{4.2}$$

where P_{max} is the maximum applied load and A is the contact area.[97]

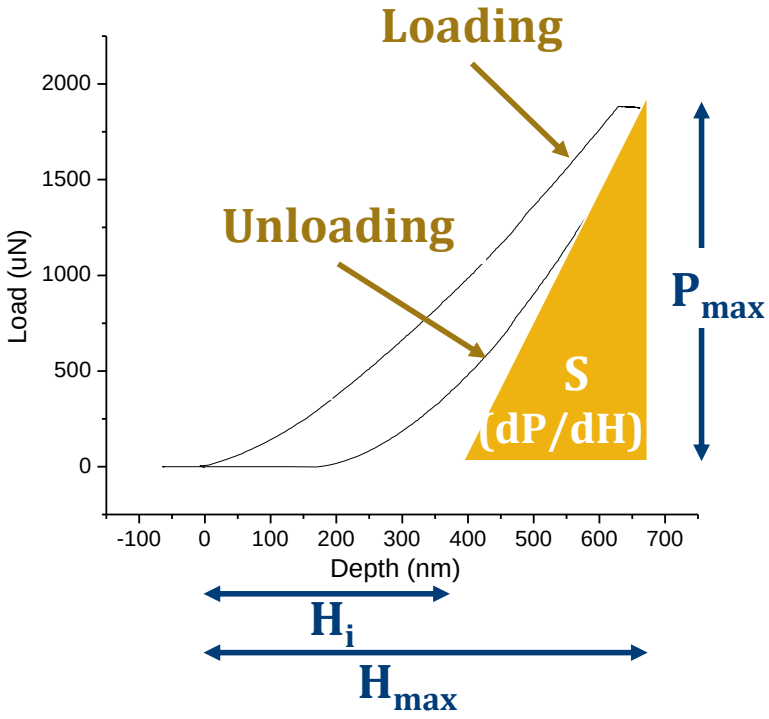

Figure 3-6. Anatomy of a nanoindentation measurement and illustration of important parameters of the Oliver and Pharr method.

Nanoindentation and calibration indents were done with a 10 second loading and unloading time and 20 second holding time at the peak applied force as illustrated in **Figure 3-7-A**. The holding step was included to compensate for polymer creep and will be explained later. The area function is the initial calibration curve that is used to correlate the indentation depth to the amount of area of the sample in contact with the indentation tip. This contact area is dependent on the shape of the indenter. This function was built by carrying out 18 measurements on a poly(carbonate) standard with a maximum applied load of 1500-3000 μN. The curve was standardized to the elastic

modulus specified by the poly(carbonate) manufacturer using the fitting equation suggested by Oliver and Pharr[98] in **equation (4.3)**:

$$A(h_c) = C_0 h_c^2 + C_1 h_c + C_2 h_c^{1/2} + C_3 h_c^{1/4} + C_4 h_c^{1/8} + C_5 h_c^{1/16} \quad (4.3)$$

where C_0 is 24.5 for a Berkovich tip, and h_c is the contact depth.[98] Poly(carbonate) was used for the calibration because it has an elastic modulus (3.10 GPa) close to that of the mixed matrix membranes and has been shown to be a more appropriate standard for polymer-based materials than the traditional quartz standard (69.6 GPa).[99] Measurements were taken of a 3 x 3 array of indentations representing a 150 ×150 μm^2 area as illustrated in **Figure 3-7-B**. For each membrane sample, five arrays were measured at randomly chosen points on the sample with an applied load of 2000-3000 μN and the same loading function as the calibration measurement. The loading times were kept constant causing the rates of indentation to vary according to peak load.

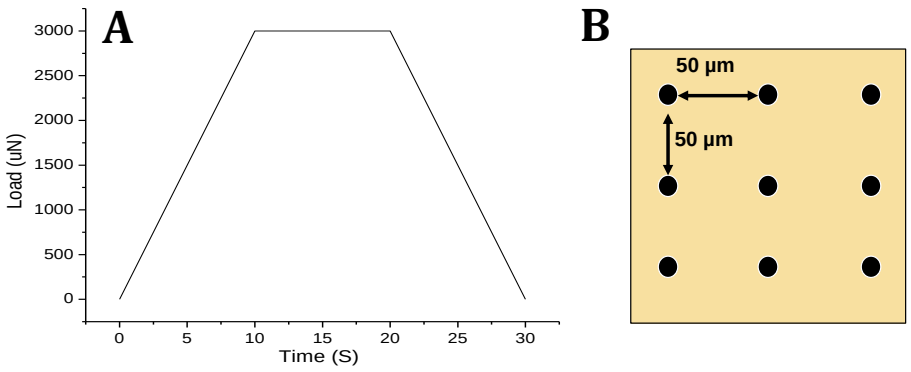

Figure 3-7. A) Loading function on nanoindentation measurement and B) spatial arrangement of indentation points per data set.

3.2.6 Gas Permeation Measurements

The single-gas CO_2 and CH_4 permeation properties were measured with an upstream pressure of 65 psia at 35°C using a permeation apparatus described in the

literature.[100–102] An in-tact portion of the membrane fabricated with bare or functionalized Ca-exchanged LTA was cut to approximately 1 cm^2. The membrane was masked by aluminum tape on both sides with a center hole diameter of 3/8-5/8," and attached to the cell using a larger circle of aluminum tape as described by Moore et al.[100] Epoxy was used to seal the gap between the membrane and the aluminum tape. Once the permeation cell was inserted into the gas permeation apparatus, vacuum was pulled on the downstream volume for 15 min to pull epoxy into the gaps between the membrane and mask. The epoxy set overnight at 35°C without a downstream vacuum. The system was degassed for 24 hours or longer until the leak rate was on the order of 10^{-6} torr/s or lower. The downstream leak rate was measured prior to the permeation measurement for each single gas and typical values ranged from 5×10^{-6} to 7×10^{-8} torr/s. To perform a permeation measurement, the downstream was isolated from the vacuum and the rise in downstream pressure was recorded as a function of time. An example downstream gas pressure measurement versus time curve is shown in **Figure 3-8**. The

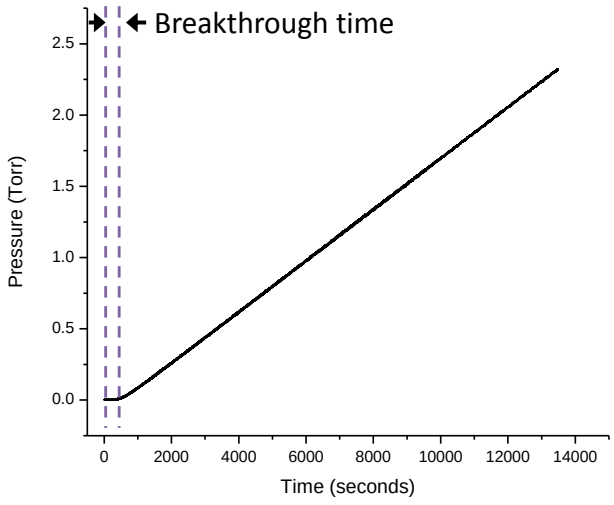

Figure 3-8. Gas permeation measurement through a Matrimid-LTA composite membrane. The 'breakthrough time' is highlighted by the purple dashed lines.

membrane flux (dp/dt) was obtained from the derivative of the linear region of the curve at steady state, or approximately ten times the duration of the breakthrough time, and the permeability (P) was calculated with **equation (4.4)** and **(4.5)**:

$$\frac{dn}{dt} = \frac{\frac{dp}{dt} \times V}{R \times T} \times C \tag{4.4}$$

$$P = \frac{\frac{dn}{dt} \times t}{A \times p_i} \times 10^{-10} \tag{4.5}$$

where t is the membrane thickness (cm), A is the membrane area (cm^2), p_i is the initial pressure (cmHg), dp/dt is the change in pressure over time (Pa/s), V is the volume of the final reservoir (m^3), R is the ideal gas constant (8.314 (Pa•m^3)/(mol•K)), T is the temperature (K), and C is a conversion factor of 22,412. The selectivity was calculated according to **equation (1.2)** and is a ratio of the CO_2 to CH_4 permeability. The film thickness was measured using a micrometer and ranged from 45-65 μm for the membranes in this work. Gas permeation measurements were repeated with a fresh section of the same membrane film to obtain replicate measurements.

3.3 Results and Discussion

3.3.1 Solvent choice

Dynamic light scattering measurements were done on solutions of zeolites in pure solvent and polymer-solvent solutions to determine the particle size in solution and how addition of polymer impacts the measured size. Measurements of the particle size in **Table 3-1** show that in the two chlorinated solvents, the measured particle size decreased and the polydispersity index increased when polymer was added to the solution. This suggests that the polymer may stabilize the smaller zeolites in solution. By keeping

smaller particles in solution, the average size decreases and there is a greater measured size variation of the particles (PdI). The tetrahydrofuran showed the opposite trend where the measured size increased when polymer was added to the solution. Additionally, it had the greatest increase in polydispersity for all the solvents after adding polymer. Upon visual inspection of the solution, it appeared that the polymer was not mixing into the solution and the added size most likely came from solid blocks of polymer in addition to the zeolite.

Table 3-1. Size and polydispersity (PdI) for zeolite/solvent solutions (particle only) and zeolite/polymer/solvent solutions (Matrimid).

		Chloroform		**THF**		**DCM**	
			stdev		**stdev**		**stdev**
Size (nm)	**Particle only**	586	97	479	17	482	93
	Matrimid	531	32	530	66	352	37
PdI	**Particle only**	0.13	0.10	0.06	0.02	0.22	0.09
	Matrimid	0.30	0.08	0.42	0.43	0.39	0.10

3.3.2 Membrane imaging

SEM images are shown in **Figure 3-9.** The bare LTA composite membranes show evidence of voids between the zeolite and polymer phases at both weight loadings. Whereas all surface functionalization methods appear to improve adhesion between the polymer and zeolite compared to the bare zeolite at the scale observable in SEM. TEM cross-sectional images of the composite membranes in **Figure 3-10** also confirm the

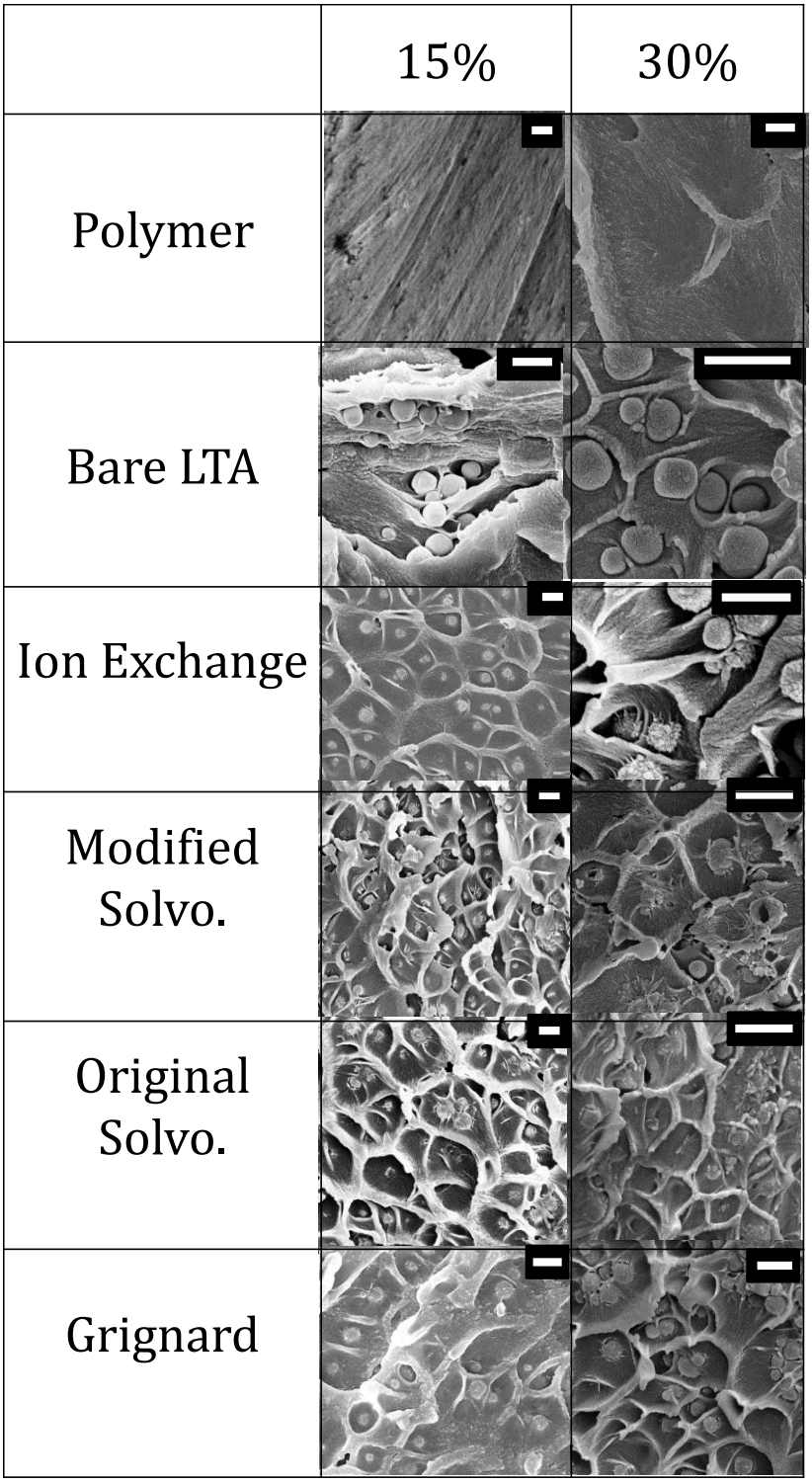

Figure 3-9. SEM images of membranes made with pure polymer, bare LTA, and LTA functionalized with four different methods at 15 and 30 wt.% loadings. Scale bars represent 1 μm.

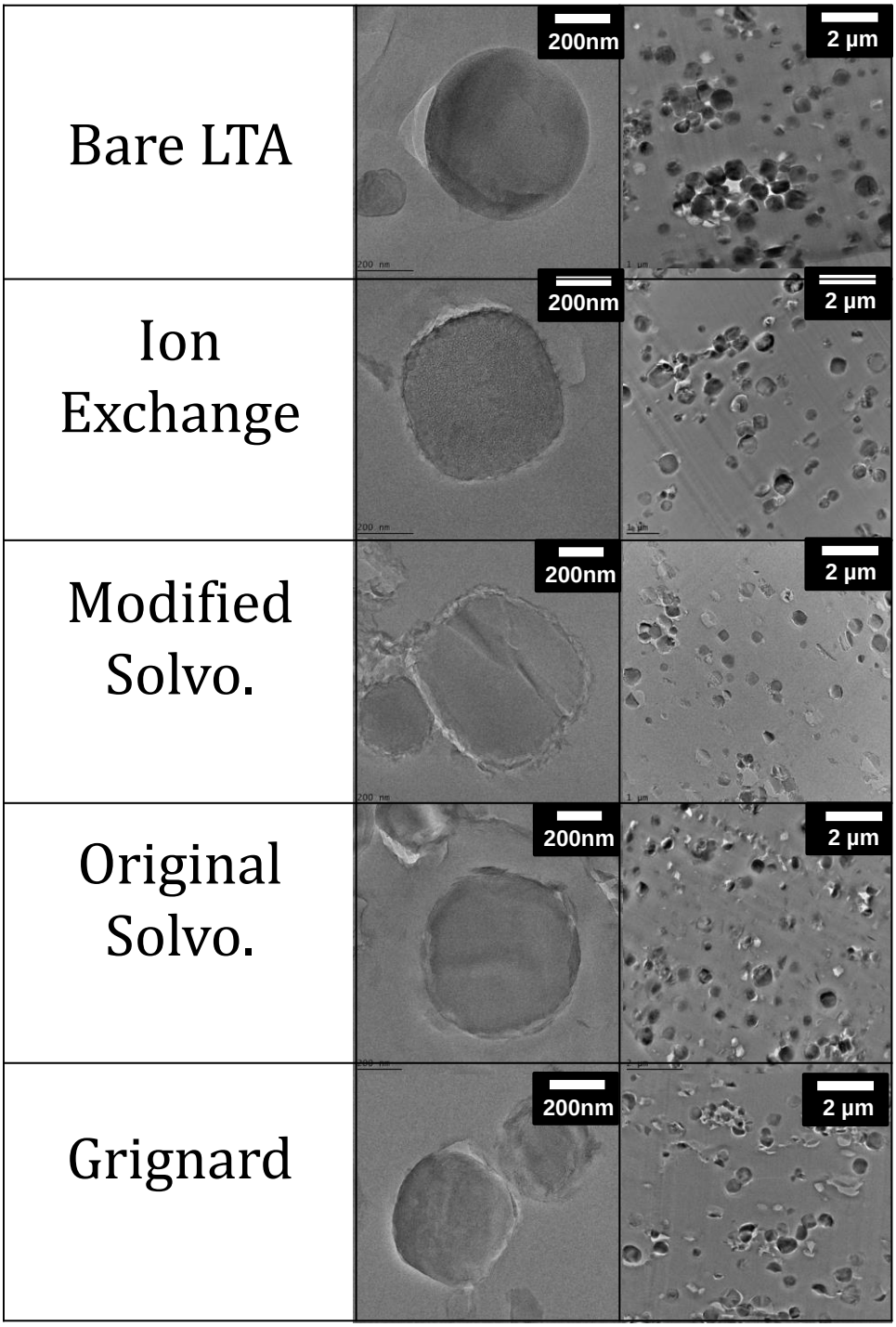

Figure 3-10. High (left panel) and low (right panel) magnification TEM images of composite membranes made with functionalized nanoparticles.

presence of voids (of width approximately 50 nm) between the bare LTA particles and the Matrimid polymer. However, even though the nanostructures appeared to remove the gap in SEM, in TEM cross sectional images smaller voids of 5-30 nm in width can be observed even between the functionalized materials and the polymer. This shows that functionalization minimizes, but does not eliminate, the void between the phases. From these images, it is also apparent that excess surface modification can create new void spaces which may impact the integrity of the membrane, such as those observed in the modified solvothermal and solvothermal MMMs. Furthermore, more particle aggregation is present in the low magnification image of the bare LTA than the functionalized samples. Lastly, the functionalization of the zeolite also has the potential to create a new void between the zeolite and functionalization because the polymer cannot fully penetrate into the nanostructures, as seen in the modified solvothermal sample. The two different types of void spaces are not differentiated in this chapter.

3.3.3 Assessment of Composite Membrane Dispersion

The results for the dispersion assessment of all composite membranes are shown in **Table 3-2**. Membranes made with bare LTA generally have a high L_f, indicating poor dispersion and high aggregation of particles. It can be observed that all functionalization methods generally improve dispersion of particles in the membrane compared to bare zeolite. The degree of particle dispersion was found to be Grignard < ion exchange < solvothermal < modified solvothermal at 15 wt% loading and Grignard < solvothermal < ion exchange < modified solvothermal at 30 wt% loading. Since the Grignard method resulted in uneven and inconsistent nanostructure coverage of zeolites, it is understandable that the resulting dispersion is only slightly better than the bare LTA and

the poorest of the functionalization methods at both weight loadings. The modified solvothermal method, with uniform and full coverage of nanostructures on the zeolite surface, consistently showed the best dispersion at both weight loadings. The ion exchange and original solvothermal methods had intermediate dispersion that varied based on the loading of zeolite particles in the composite membrane. This shows that even minor changes in the particle surface area and surface chemistry from functionalization lead to improved particle dispersion compared to the unfunctionalized zeolite.

Table 3-2. Free space length of the composite LTA/Matrimid® membranes.

Particle	**15 wt% loading Free Space Length (L_f)**	**30 wt% loading Free Space Length (L_f)**
Bare LTA	11.5 ± 0.2 µm	1.42 ± 0.04 µm
Ion Exchange	7.2 ± 0.2 µm	1.22 ± 0.04 µm
Modified Solvothermal	5.1 ± 0.1 µm	0.54 ± 0.01 µm
Solvothermal	5.7 ± 0.4 µm	1.5 ± 0.1 µm
Grignard	9.9 ± 0.4 µm	1.3 ± 0.1 µm

3.3.4 Membrane Mechanical Properties

Each mechanical measurement included 9 points of indentation and resulted in the typical load-displacement curves shown in **Figure 3-11** for MMMs made with each functionalization method. The Matrimid membrane displays a uniform load-displacement curve in all nanoindentation locations (**Figure 3-11-A**). When bare or functionalized zeolite LTA is introduced into the membrane, there was typically greater variation in the displacement depth of the curve (**Figure 3-11-B-F**) and shallower penetration depth as

compared to the pure polymer membrane. These variations correspond to a greater inhomogeneity of elastic modulus and hardness (with respect to location) due to the two-phase nature of the mixed matrix membranes. For example, the blue curve in **Figure 3-11**-**B** represents a location in in the sample with greater hardness and stiffness than the

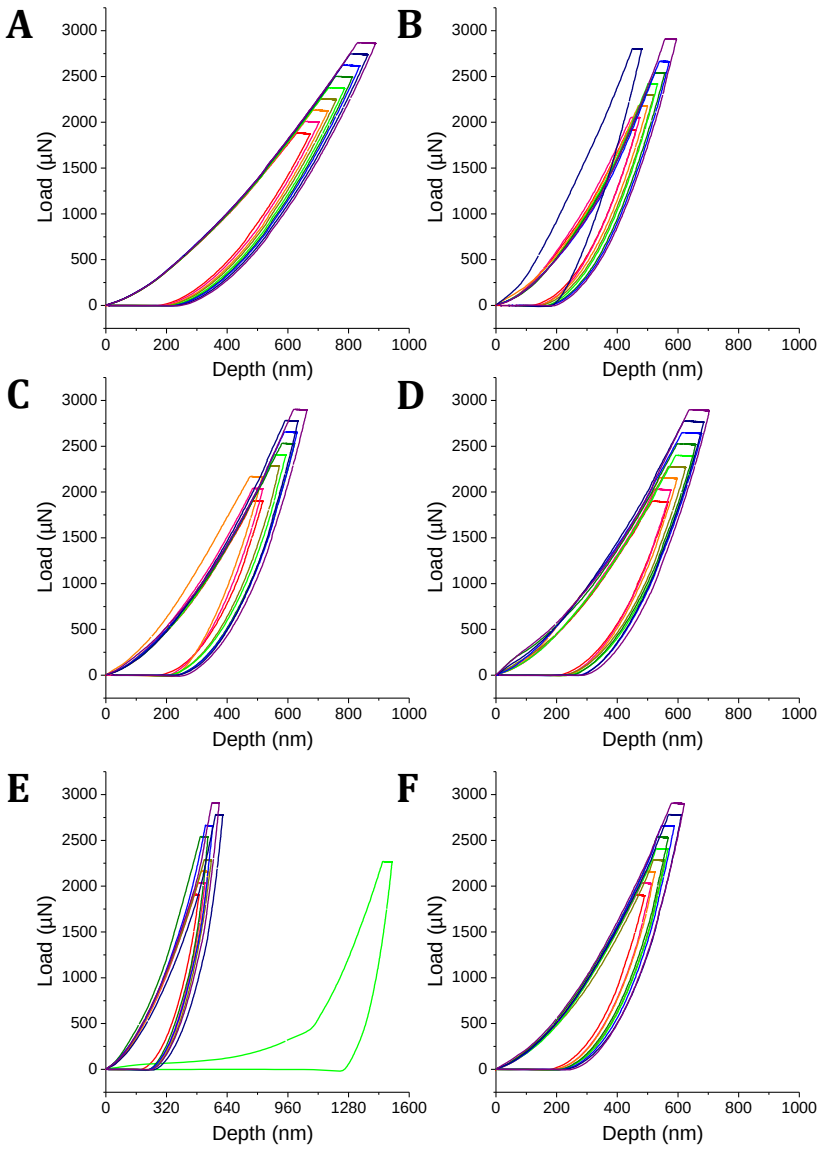

Figure 3-11. Example nanoindentation measurement force vs. depth curve for A) pure Matrimid® polymer and Matrimid® mixed matrix membranes with B) bare LTA, C) ion exchange D) modified solvothermal, E) original solvothermal, and F) Grignard functionalized LTA.

rest of the sample. Occasionally (about 1 out of 250 individual measurements), an unusually deep penetration depth was observed (e.g. the outlier curve in **Figure 3-11-E**) that likely resulted from a concentration of local stress and resultant slipping of aggregated particles past each other under the applied load.[103–105] These measurements were atypical and were not used in the quantification of the average elastic modulus and hardness. The pure polymer (**Figure 3-11-A**) and modified solvothermal MMM (**Figure 3-11-D**) showed a nearly linear relationship between maximum applied load and indentation depth. This near-linear relationship for the modified solvothermal sample is due to a narrower distribution of mechanical properties and indicates greater homogeneity of the composite membrane. A comparison is the original solvothermal method (**Figure 3-11-E**) which, even without the aggregate curve, shows a deviation from a consistent load versus depth. Lastly, none of the load-displacement curves show evidence of a 'forward nose.' This indicated that the holding time is sufficient to minimize the impact of polymer creep. The 'forward nose' phenomenon occurs when the viscoelastic material shows a change in strain rate with a constant applied stress and can lead to an incorrect modulus measurement.[106,107] Creep tends to be higher in rubbery polymers and it has been noted that if the holding time is extended, the polymer can come to an equilibrium, and creep effects on the modulus measurement can be minimized.[107]

Since the composite is inherently heterogeneous, the mechanical property results are displayed statistically based on a series of 45 individual measurements for each membrane type. The reduced elastic moduli (**Figure 3-12**) show that all the mixed matrix membranes, whether prepared with bare or functionalized LTA, have a higher elastic modulus than the pure polymer membrane. This result is consistent with the theory of

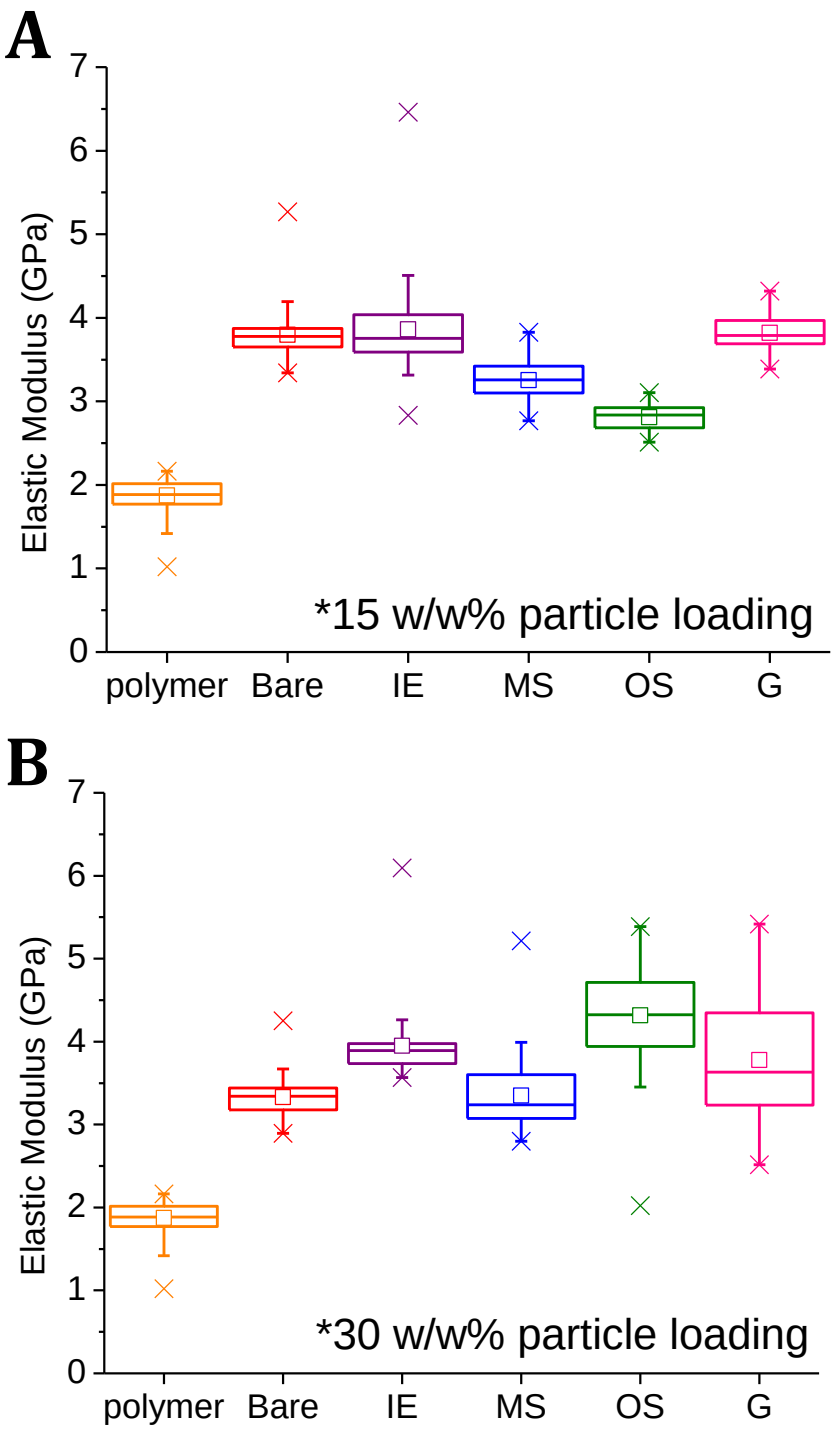

Figure 3-12. The reduced elastic modulus determined by nanoindentation for membranes with (A) 15 wt.% and (B) 30 wt.% zeolite loading. The divided box represents the 25th, 50th, and 75th percentile values, the whiskers represent the statistical outliers, the X represents the maximum and minimum values in the data set, and the square represents the average value.

mechanical properties of composites, which suggests that the mechanical properties of composite membranes (regardless of functionalization) should improve in relation to the pure polymer.[108,109] The rule of mixtures can be used to predict the Voigt (volume-averaged stress treatment) and Reuss (volume-averaged strain treatment) bounds for the elastic modulus in composites.[110,111] The theoretical and actual values for the mixed matrix membranes are shown in **Figure 3-13.** From this information, it is seen that at 15% loading the composite membranes are closer to the upper (Voigt) bound of volume averaged stress treatment. However, at 30% loading membranes are much closer to the lower (Reuss) bound and the realm of equal strain treatment. This shows that there are greater non-idealities (e.g., poor adhesion) at the interface between the particles and

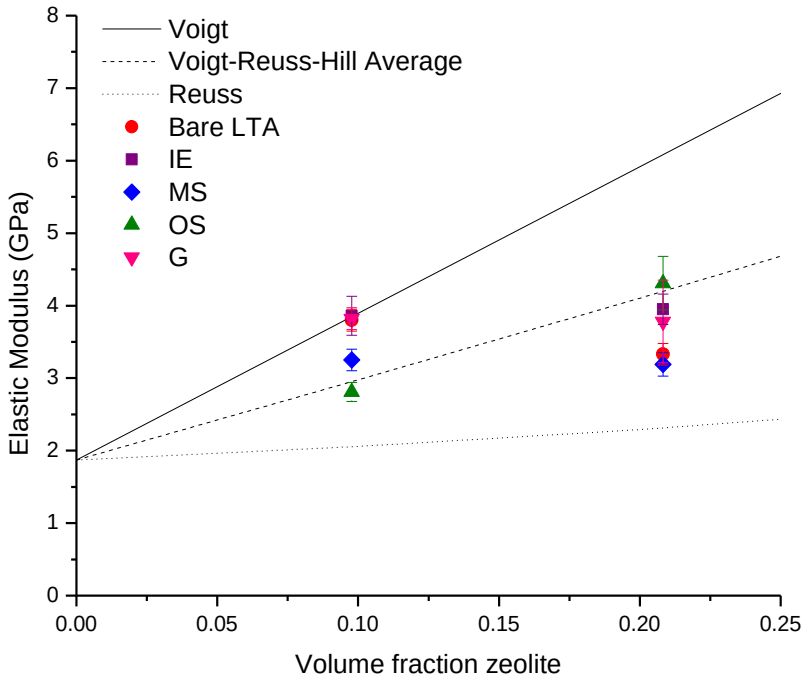

Figure 3-13. The measured average elastic moduli versus predicted Voigt and Reuss bounds.

matrix or the occurrence of slipping between adjacent particles at higher particle loadings that minimize the improvement in mechanical properties at higher loadings. Additionally, our results are consistent with examples in the literature that show improved elastic modulus upon incorporation of a filler (e.g., Guo et al. with 30 nm alumina nanoparticles in a vinyl ester resin [112] matrix, and Musto et al.with micron sized silica particles in a poly(imide) matrix).[113] The improvement in elastic modulus is attributed to a combination of good adhesion between the two phases which allows the absorption of more energy through local plastic deformation, microcracking, elastic deformation, crack deflection, and transfer of stress from the weaker polymer material to the stronger zeolite material [103,105,112,114,115] and the formation of a rigidified polymer layer near the interface with different properties than the bulk polymer.[103,105,116]

The data in **Figure 3-12** show slight variations between the functionalization methods; however, the functionalization method does not seem to have a significant or reproducible trend in improving the membrane mechanical properties. However, zeolite loading does have an impact on the mechanical measurements. At 15 wt% loading, the spread of measured elastic moduli is much narrower than for the 30 wt% loading case, thus confirming that the membranes are more mechanically homogenous at lower loadings. Since data with large aggregates (as shown in **Figure 3-11-E**) were not used in the averaging, the slipping phenomenon occurring in aggregated regions was largely removed; however, minor slipping between particles in smaller aggregates may lead to weaker sections of the membrane than would be expected without any aggregation.[105,114,117,118] Additionally, clusters of particles can reduce the interfacial area between the two phases (that normally may contribute to polymer

stiffening) which may also lead to lower than expected mechanical properties. [116,119,120]

The hardness (**Figure 3-14**) shows similar trends to the elastic modulus. The hardness is considered to be representative of both plastic and elastic deformation, while the elastic modulus represents only the elastic deformation properties.[97] In metals, the elastic component of hardness may be negligible and the hardness can be considered independent of the elastic modulus. However, in polymers the elasticity is not negligible and hence the hardness is not entirely independent of the elastic modulus.[116,121,122] Thus, it is not surprising that the elastic modulus and hardness results show similar trends in the polymer composite membranes. However, since hardness is the response of the material to an applied force whereas the elastic modulus is the response of the material after withdrawing the applied force, useful information can still be obtained by comparing data from these two measurements (**Figure 3-12** and **Figure 3-14**). First, the composite hardness is always equal to or greater than that of the pure polymer, meaning that incorporation of bare or functionalized LTA has a neutral or positive impact on the mechanical properties of the membrane. Additionally, the hardness increased from 0-25% and the elastic modulus from 35-100% for the composite materials in comparison to the pure polymer. As seen previously in the literature, the filler influences the elastic modulus of the material significantly more than it does the hardness. [116]

Figure 3-15 shows plots of the two mechanical properties (elastic modulus and hardness) versus the particle dispersion property (free space length). Interestingly, improvements in mechanical properties do not show any strong correlation with particle dispersion, in contrast with some of the literature mentioned previously. [114,120] For

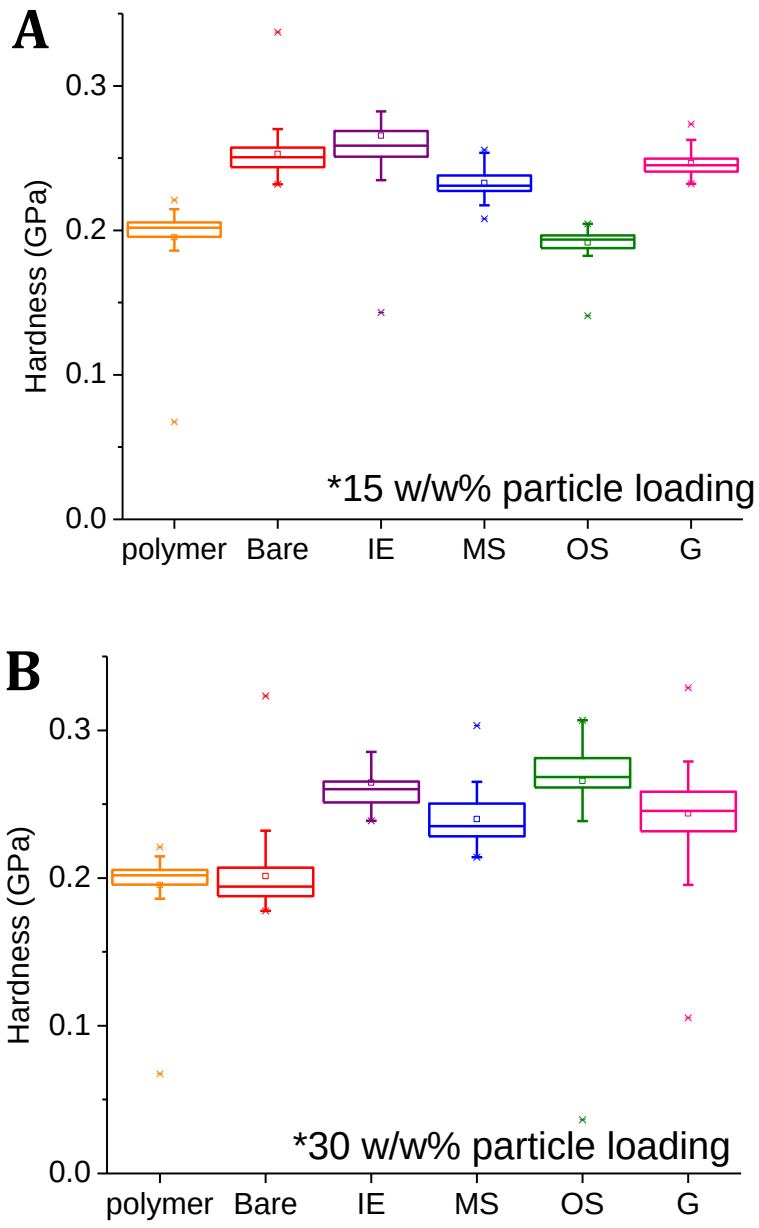

Figure 3-14. Hardness determined by nanoindentation for A) 15 w/w% loading and B) 30 w/w% loading membranes. The divided box represents the 25th, 50th, and 75th percentile values, the whiskers represent the statistical outliers, the X represents the maximum and minimum values in the data set, and the square represents the average value.

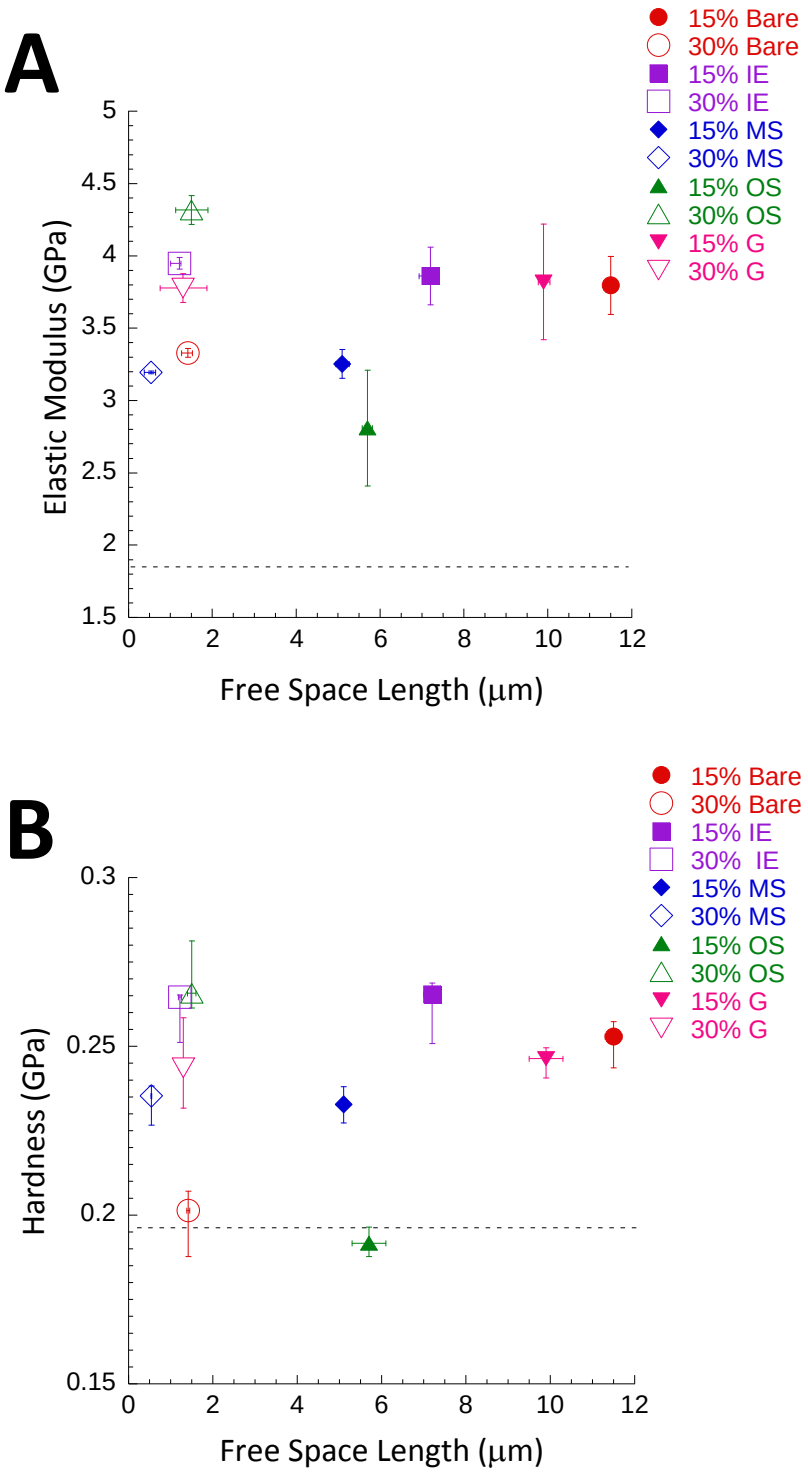

Figure 3-15. (A) Free space length versus elastic modulus, and (B) free space length versus hardness.

example, the Grignard method resulted poorer dispersion but better mechanical properties compared to the other functionalization methods. The modified solvothermal method, with the best dispersion at both weight loadings, showed relatively poor mechanical properties versus the other functionalization methods. These results indicate that the mechanical properties of these mixed matrix membranes are more dependent on the strength of the specific interface interactions between the polymer and the surface nanostructures (which differ for each type of surface-modified particle) than the dispersion.

3.3.5 CO_2/CH_4 Gas Permeation Measurements

CO_2 and CH_4 permeation measurements were conducted on the pure polymer and functionalized mixed matrix membranes samples that have been used throughout this chapter and the results are shown in **Figure 3-16**. All membranes were made with Ca-exchanged LTA. Neither the bare LTA MMM, nor the MMMs made with either form of solvothermally-modified and Grignard-modified LTA, showed improvement of permeation properties from those of pure polymer membrane. On the other hand, the MMMs made with ion-exchange-modified LTA demonstrated a substantial CO_2/CH_4 selectivity increase without loss of CO_2 permeability. Thus, the ion exchange modified particles show the greatest potential of all the functionalization methods summarized in Chapter 2 for use in the fabrication of mixed matrix membranes. This supports the hypothesis from Chapter 2 and illustrating the impact functionalization may have on MMMs performance and suggests intimate contact and good adhesion between the polymer and zeolite.[84]

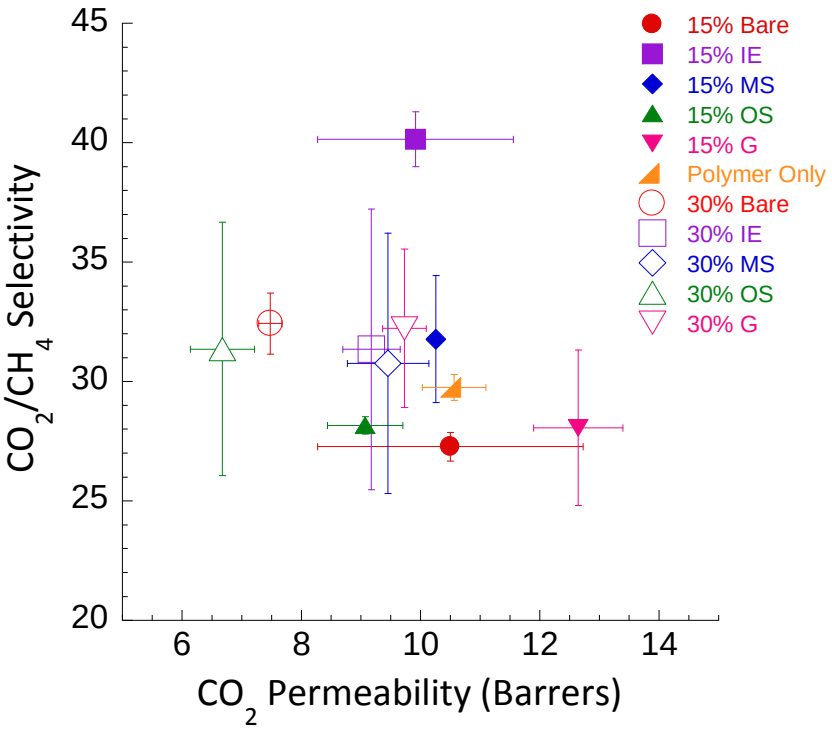

Figure 3-16. Gas permeation properties of 15 wt.% membranes and 30 wt.% zeolite loaded membranes. [84]

The 30 wt% membranes do not appear to have further improved selectivity compared to the 15 wt% membranes and actually slightly decreased permeability which is a phenomenon that has been seen before in LTA-based MMMs for gas separations.[19,27,75] These results show that effects such as increase in particle aggregation, increased interfacial rigidification, and greater incidence of interfacial defects (i.e. voids) have a significant impact on the performance of membranes at higher particle loading. When comparing gas permeation properties with elastic modulus, hardness, and dispersion, we found no direct correlations between these characteristics (**Figure 3-17** and **Figure 3-18**). The overall lack of apparent trends in the data highlights

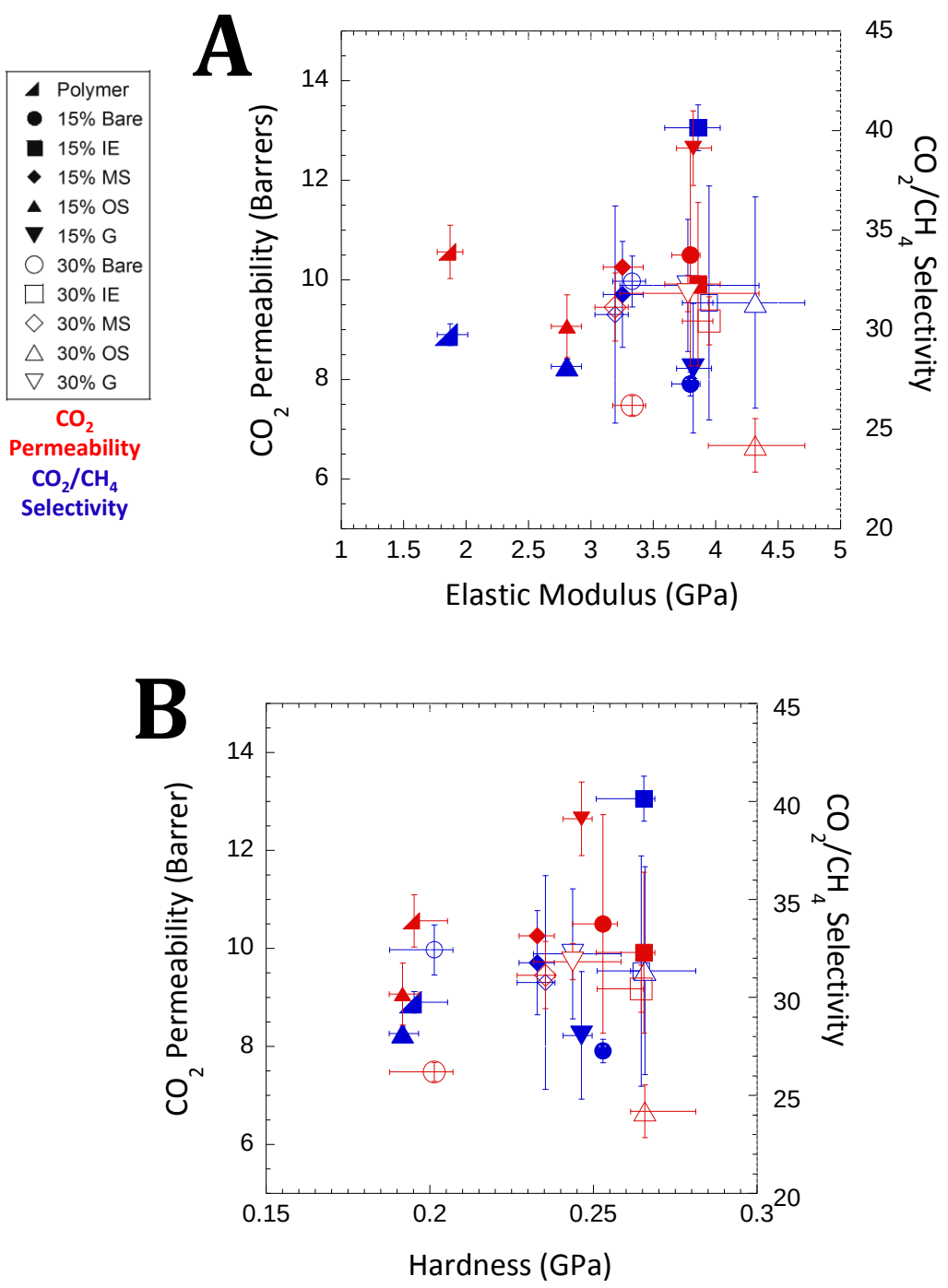

Figure 3-17. (A) Elastic modulus versus CO_2 permeability and CO_2/CH_4 selectivity and (B) Hardness versus CO_2 permeability and CO_2/CH_4 selectivity.

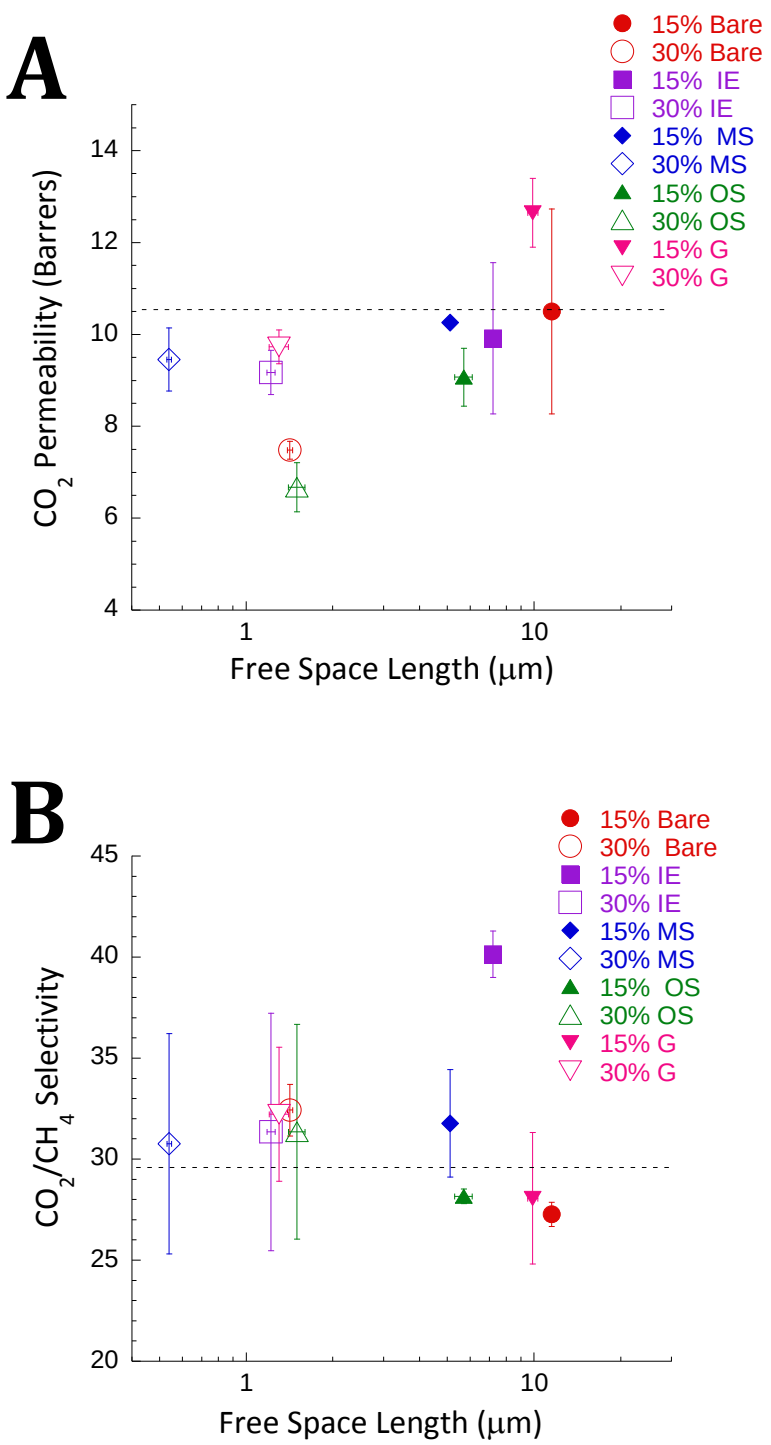

Figure 3-18. (A) Free space length versus CO_2 permeability and (B) Free space length versus CO_2/CH_4 selectivity. The pure polymer value is represented by the dashed line.

the

fact that the morphology and structure of the surface features formed by each functionalization method, changes in the porosity of the zeolites, and the specific interfacial bonding interactions between the particles and the polymer can significantly impact the dispersion, mechanical, and gas permeation properties of MMMs in a complicated way that may not generalize to the bulk properties of the membrane.

3.4 Conclusions

This chapter has examined the impact of different functionalization methods on the mechanical, dispersion, and gas separation properties of zeolite/polymer composite membranes - specifically the quantification of mechanical and dispersion properties which have only been assessed qualitatively (or not at all) in the literature and previous work in this field. All surface functionalization methods studied led to quantifiably improved particle dispersion as compared to bare LTA membranes and all composite membranes show better elastic moduli and hardness than the pure polymer membranes. However, there was no evidence that a specific functionalization method produces superior mechanical properties. The elastic moduli and hardness values were found to be comparable at the two weight loadings but showed a greater heterogeneity of membrane at higher loading. The gas permeation properties of the membranes do not significantly increase with higher particle loading, thereby indicating the effects of aggregation and interface modification override the increased particle loading. Lastly, the membrane gas permeation, mechanical and dispersion properties are not significantly correlated, thus showing the importance of the specific surface nanostructure-polymer interfacial interactions and pore blocking effects existing in the membranes made with each type of particle.

4 Chapter 4: Characterization of the Zeolite/Polymer Interface in LTA/Polyimide MMMs

4.1 Introduction

The previous chapters have explained the thorough characterization of inorganic MgO_xH_y nanostructures deposited on zeolites and the use and characterization of these functionalized zeolites in 'bulk' mixed matrix membrane applications. However, the interfacial region between the two phases is of the utmost interest to understand the performance of nanostructured zeolites in MMMs and has been poorly characterized in the past. This chapter will give a theoretical overview of the interactions between the two different phases and an experimental investigation into the polymer mobility and constraints at the interfacial region.

The adhesion between poly(imide)-ceramic systems has been of interest, particularly for its use in the microelectronics industry, yet a true knowledge of the type of adhesion at this interface is still unknown.[123] The interface between the materials in the composite of interest, poly(imide) MMMs with surface roughened LTA as a filler, has primarily been probed via gas permeation. The degree of adhesion is roughly estimated based on the size of the probing molecule; however, this neglects to account for many other contributing factors. Thus, a more direct probe of the interface is desired. The goal of the work in this chapter was to determine the local polymer environment at the interface of the two materials. Additionally, if possible, the nanostructure properties are correlated to the properties of the polymer at the interface to better understand how the nanostructure morphologies elucidated in Chapter 2 impact MMMs.

Because of the small scale interaction, direct adhesion measurements would be difficult to do. Atomic force microscopy (AFM) has been used to determine the attraction between a polymer and zeolite by Lee et al.[124] However, this experiment does not account for vertical and horizontal forces as might be present in a MMM and therefore is not a true representation of a MMM interface. In this work, nuclear magnetic resonance (NMR) is able to probe the local characteristics of a bulk material and can reveal the small changes in dynamics that may occur in the interfacial region. Specifically, NMR spin-spin (transverse) relaxation was used as a representation of polymer mobility and to elucidate the motion of the polymer in the sample. This method allows observation of the effects of deposition of nanostructures on the amount and degree of stiffness of the polymer at the interface. When used in addition to tests on pure zeolite and $Mg(OH)_2$ MMMs, the origin of the observed changes in the polymer mobility can be attributed to the chemical nature or steric disruptions of the polymer packing. Additionally, HarmoniX mode AFM of a membrane cross section allows simultaneous topographical imaging while measuring and mapping the mechanical properties. This method shows whether the molecular scale trends observed in NMR are observable on a larger scale and provide a better understanding of how the nanostructures may impact the polymer region surrounding the zeolite.

4.2 Chemistry at Oxide-Poly(imide) Interfaces

4.2.1 Mechanisms of Adhesion

Several mechanisms can contribute to adhesion between two materials including: mechanical interlocking; surface energy, wetting and adsorption; diffusion; electronics and electrostatics; and chemical bonding.[125,126] The electronic mechanism from an

electrostatic double layer is not of concern in polymer-inorganic oxide interfaces when used for non-semiconductor applications due to the insulating nature of the oxide.[126] Diffusion theory consists of the two components blending together by diffusion of at least one component into the other. This is a more significant adhesion mechanism in other types of interfaces such as between two polymers. What might be considered diffusion in solid-polymer interfaces, is better classified under the mechanical interlocking theory, thus, the diffusion mechanism of adhesion is not used to classify oxide-polymer regions in this work.[125,126] The next adhesion mechanism, the free energy of the interacting species, determines the wetting of the inorganic surface during processing.[125,126] Proper wetting of the mineral material is important to facilitate the initial contact between the two phases. Since the surface free-energies of the inorganic materials are significantly higher than the polymer solution, proper wetting should not be a problem between oxides and polymer solutions.[126] However, a highly viscous solution may prevent proper surface wetting especially in the case of the highly nanostructured materials because it is unable to penetrate into the small gaps.[108,127] The wettability of the oxide surface is an important first step to adhesion, but does not necessarily correlate to the strength of adhesion between the two layers.[126] The two remaining mechanisms (mechanical interlocking and chemical bonding) are the most important for determining the adhesion in metal oxide-polymer composite materials.

Mechanical interlocking theory suggests the interfacial joint between the two materials is strengthened by roughening the mineral surface.[125,126] The surface roughness promotes wetting of the mineral by addition of surface defects contributing to the initial bond, and then provides mechanical overlap between the two phases.[126]

Chemical bonding is the strongest mechanism of adhesion between phases and includes primary (ionic, covalent, or metallic bonds) and secondary interactions (Van der Waals (VDW) and H-bonding). Donor-acceptor, or Lewis and Brönsted acid-base interactions, are also included in this adhesion mechanism but their classification falls between primary and secondary.[125,126] Chemical bonding also represents a very small length scale of adhesion of no more than a few nanometers rather than long range interactions as would be seen with mechanical interlocking.[126]

The interaction between the polymer and zeolite/nanostructure is initially determined by adhesion in a dilute polymer-solvent solution and can be represented by the general **equation (4.1)**:

$$W_A = -\Delta G = \gamma_L + \gamma_S - \gamma_{SL} \tag{4.1}$$

where W_A is the thermodynamic work of adhesion, γ_L is the surface free energy of the liquid (polymer-solvent solution), γ_S is the surface free energy of the solid (zeolite or nanostructure), and γ_{SL} is the interfacial free energy of the solid-liquid interface.[124,126] This represents a reversible process.[126] A more specific version of this equation includes the specific types of interactions present by including van Oss and Good's Lifshitz-van der Waals acid-base theory (or the three liquid acid-base method). This is shown in **equation (4.2)**:

$$W_{SL} = 2(\gamma_S{}^{vW}\,\gamma_L{}^{vW})^{1/2} + 2(\gamma_S{}^{+}\,\gamma_L{}^{-})^{1/2} + 2(\gamma_S{}^{-}\,\gamma_L{}^{+})^{1/2} \tag{4.2}$$

where γ^{vW} represents the Van Der Waals, γ^{+}, the electron acceptor (Lewis acid), and γ^{-}, the electron donor (Lewis base) components of surface energy.[124] An important note is

that the revised equation neglects shrinkage stresses, assumes constant polymer free energy before and after solidification, and does not include primary type interactions (such as ionic or covalent bonding). [126] If shrinkage stresses occur, the adhesion joint may behave very differently after polymer solidification than predicted in **equation (4.2)**.[126]

The functionalized zeolite-polymer system in this thesis has three relationships that combine to form the interfaces in MMMs: the aluminosilicate or silicate zeolite-polymer interface, the MgO_xH_y surface nanostructure-polymer interface, and the zeolite-nanostructure interface. It is difficult to directly measure the aluminosilicate-MgO_xH_y interface and it will not be explained further than in Chapter 2. It will be assumed to be stronger than the polymer-nanostructure or polymer-zeolite interactions in this work. Of course, if this is not true, the nanostructure can detach causing another deviation from expected behavior.

4.2.2 Zeolite-Polymer Interface

The zeolite-polymer interaction is important in the unfunctionalized zeolite MMM. Additionally, this type of interface may contribute in the functionalized zeolite MMMs as well, but is expected to be a minor influence due to its smaller proportion of surface area. Since the zeolite surface is relatively smooth and devoid of significant surface roughening, interactions between the polymer and zeolite are attributed to chemical bonding interactions rather than mechanical interlocking. Thus, the surface properties of the zeolite are important to determine the specific type of chemical bonding that occurs at the interface. Both silica and alumina based solids possess surface hydroxyl groups that can function as Brönsted and Lewis acids.[128] It has been suggested that the

hydroxyl goups on silica-alumina compounds are unique from those on either alumina or silica ceramics.[128] Aluminosilicates can have Al^- sites in the framework. When these sites are adjacent to a Brönsted acid site, the oxygen (of the Brönsted acid site) can act as a Lewis acid by removing its hydrogen, or as a Lewis base by coordinating with the charged alumina site as illustrated in **Figure 4-1**. Because the acid site can tetrahedrally coordinate it is distinctive from other Brönsted acid sites.[128] Furthermore, undercoordinated surface sites (that are more prevalent in aluminosilicates and at defects) are more reactive.[129,130] This suggests both zeolites will be capable of H-bonding because of the silanol groups and VDW forces, but the aluminosilicate LTA may be more likely to show other acid-base type interactions with the polymer.

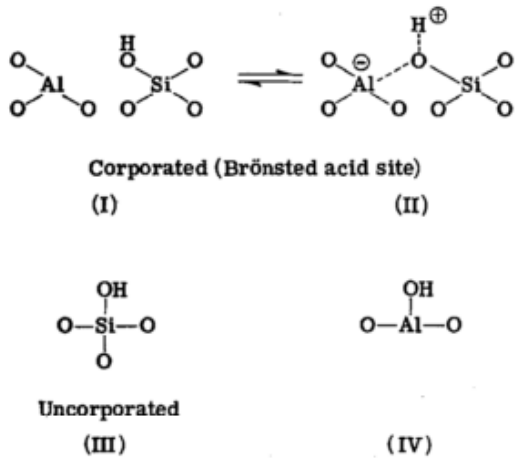

Figure 4-1. Bronsted acid sites in aluminosilicates (II), silicate (III), and aluminate (IV) materials.[128]

The primary interaction in the poly(imide)-zeolite interface is H-bonding between the acidic (e^- accepting group) of the zeolite such as its silanol groups or defect sites and the basic (e^- donating groups) of the polymer surface.[124] Previous characterization of the Matrimid polymer surface has determined that it has a slight e^- donating character due

to its carbonyl groups, and a negligible e^- accepting character.[124] In poly(imide)-pure silica MFI bonding, the Lewis acid/base interaction has been estimated to be about 6 times more important than VDW forces in contributing to adhesion strength.[124] Since acid/base bonding is not a primary interaction, these bonds are easily overcome by tensile stresses in the polymer during solvent evaporation, which leads to the voids mentioned previously.

In the literature, when poly(imides) were attached to a silica or alumina substrate, they were determined to form a "weak boundary layer" between the polymer adsorbed to the ceramic surface and the bulk polymer (**Figure 4-2**).[123,125] The evidence for this layer was residual polymer present on the ceramic after an adhesion peel test where the peel test evaluates the strength of secondary bonds and steric (from polymer chain entanglement) components of adhesion.[123,125] The main cause of the weak boundary layer is hypothesized to be due to polymer alignment. The polymer aligns itself parallel to the ceramic surface during drying.[125] The bulk polymer, meanwhile, has more three dimensional mixing and positioning of the polymer chains. The aligned polymer does not blend into the bulk polymer very well forming the weak region between aligned

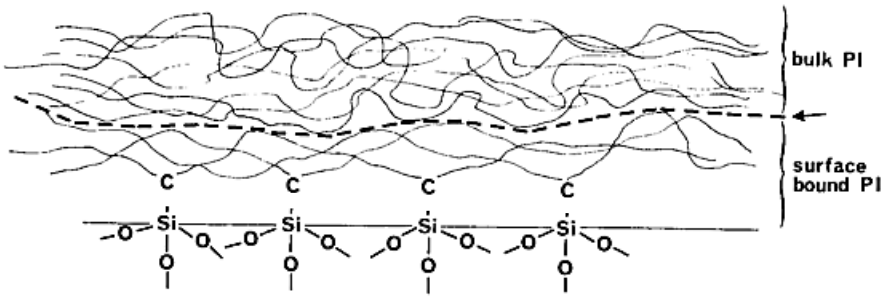

Figure 4-2. Schematic of surface bound polyimide as the "weak boundary layer" and the bulk polyimide as a method of attachment between the two phases.[123,125]

two dimensional polymer conformations and the three dimensional bulk polymer. It has also been noticed that functionalization via organic surface modification (without causing covalent linking between the two phases) eliminates the boundary layer phenomenon. This occurs because the organic chains disrupt polymer alignment with the surface and cause chains near the surface to maintain their natural three dimensional conformation.[125]

4.2.3 MgO_xH_y-Polymer Interface

The nanostructure interaction with Matrimid can be approximated by previous studies on MgO-poly(imide) interactions. The MgO structure is particularly insulating and the [100] plane is inert to molecular adsorption at room temperatures.[129] The [111] surface, on the other hand, is polar and thus may be able to interact more strongly with the poly(imide) material.[130] Experimentally, MgO has shown a different type of interfacial interaction with the poly(imide)s than alumina or silica surfaces.[123] Firstly, the peel strength was much lower between MgO and the poly(imide) than silica or alumina materials (that have approximately the same peel strength) indicating a weaker attraction for MgO.[123] Secondly, residual MgO was attached to the polymer after the peel test indicating the crystal was destroyed during the test.[123] Since MgO mechanical properties are similar to those of alumina and silica, which did not exhibit this feature, the failure was not due to the MgO mechanical strength. Instead, it was attributed to the isoelectric point of the surface of the mineral. A table of isoelectric points for the various substrates is shown in **Table 4-1**.[125,131,132] In poly(imides) formed by carboxylic

Table 4-1. Isoelectric points of various mineral oxide materials. [125,131,132]

Species	Isoelectric point	Comment
MgO	12.1-12.7	Basic
$Mg(OH)_2$	~12	
Al_2O_3	7.5-9.5	
SiO_2	1.5-2.7	Acidic
Al_2O_3*	9.2	*hydrated oxide

acid precursors, the extremely strong acid-base interactions between the MgO, poly(imide), and trace carboxylic acid precursors resulted in a chemical attack that destroyed the MgO structure.[123,125] This reaction was actually determined a priori for a pyromellitic dianhidride-oxydianiline (PMDA-ODA) derived poly(imide) by Bolger's interaction parameters defined in **equations (4.3) and (4.4)**:[133]

$$\Delta_A = \text{IEPS (B)} - \text{pKa(A)} \tag{4.3}$$

$$\Delta_B = \text{pKa(B)} - \text{IEPS (A)} \tag{4.4}$$

where Δ_A and Δ_B are the acidic and basic interaction parameters and IEPS is the isoelectric point. When $\Delta<<0$ there are very weak acid base reactions, when $\Delta=0$, the acid-base interactions are on the order of dispersion forces, and when $\Delta>>0$, there are strong acid-base interactions that can actually cause the chemical attack.[133] The Bolger parameters were predicted to be Δ_A = 7.3 and Δ_B = -1.4 for the MgO-poly(imide) system with carboxylic acid precursors.[134] Thus, the basic character of MgO (and $Mg(OH)_2$) does not adhere as well to polyimides as silica or alumina materials.

4.3 Analysis of Interfacial Polymer Properties Using NMR

4.3.1 NMR Theory

Nuclear magnetic resonance (NMR) is a technique for characterizing a molecule or material based on its nuclear spin properties. Certain nuclei have their own local magnetic field, dependent on their spin characteristics, that can absorb a photon at their Larmor frequency (ν) when placed in an externally applied magnetic field.[135,136] The ν is dependent on the ratio of the magnetic dipole to its angular momentum, or the gyromagnetic ratio of the particle.[136] The important properties of the ^{1}H nucleus (used in the NMR studies described in this chapter) are shown in **Table 4-2**.[136] A magnetic moment is introduced when the ground state of the nucleus mixes with the paramagnetic excited state as a response to an applied radio frequency (RF) pulse.[135] The NMR experiment detects the precession of this magnetic moment.[135] NMR is often used to characterize the chemical environment of atomic components of a molecule by describing their chemical shifts (structure) or relaxation properties (dynamics).

Table 4-2. Spin properties of ^{1}H atom.[136]

Nuclei	Unpaired Protons	Unpaired Neutrons	Net Spin	γ (MHz/T)
^{1}H	1	0	1/2	42.58

4.3.2 Spin-Spin Relaxation

Spin-spin or T_2 relaxation is the recovery of transversal magnetization.[137] For the case of ^{1}H solid state NMR, the spin-spin relaxation is dominated by dipolar interaction between individual protons.[138,139] After a pulse is applied to a molecule in

a magnetic field, the spin will relax back to its ground state. The spin-spin relaxation refers to the relaxation in the XY plane and is also often called the transverse NMR decay. Conceptually, the simplest way to detect spin-spin relaxation is by observing the magnetization decay observed after a single radiofrequency pulse (Bloch decay). The observed magnetization decay can be analyzed by direct fitting to a suitable relaxation function or through Fourier transformation into an NMR spectrum. The relaxation time of the Bloch decay, T_2*, is inversely proportional to the line width of the spectrum, therefore a faster spin-spin relaxation leads to a broader line width and vice versa as shown in **Figure 4-3**.[136,137] Broader peaks (T_2* on the order of μs corresponding to a spectrum with a linewidth of 50 kHz) are characteristic of rigid molecules (i.e. crystallites, or glasses) while narrow peaks (T_2* on the order of ms) often result from mobile molecules/segments in fluids or soft solids (i.e. elastomers). The peak narrowing in mobile or flexible materials comes from an averaging of the quantum chemical

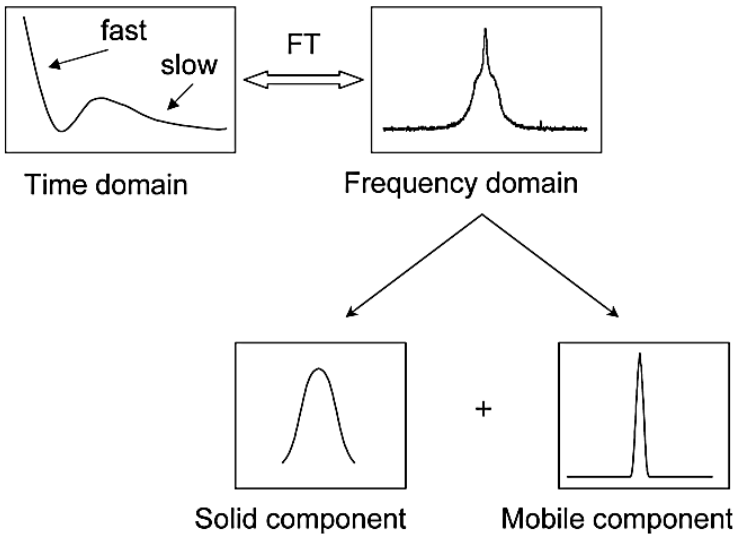

Figure 4-3. Comparison of the ^{1}H NMR spectral motions in the frequency and time domains.[168]

interactions with increased molecular motion especially the dipolar couplings and chemical shift contributions.[139] The curve shape can be deconvoluted into a contribution from a solid component with a fast relaxation and a mobile component with a slow relaxation that can be studied independently.

In practice, after applying a radio frequency pulse the signal (S) is a function of the data acquisition time (t) as shown in **equation (4.5)**:

$$S(t) \propto \{\cos[(\omega - \omega_0)t] + i \sin[(\omega - \omega_0)t]\}\exp\left\{-\frac{t}{T_2^*}\right\} \quad (4.5)$$

where ω is the receiver frequency, ω_0 is the nuclear resonance frequency dependent on the applied magnetic field strength and T_2^* is the magnetization decay due to spin-spin relaxation time constant, field magnetic inhomogeneities such as the shim or distortions from filler particles.[136,139–141] However, the field inhomogeneities play a more important role in the measurement of the mobile relaxation times (which are largely neglected in this work). In rigid materials, the relaxation is largely caused by strong dipolar couplings. Therefore T_2* can be considered to be entirely a measurement of these dipolar couplings despite including other contributing processes.[141,142]

4.3.2.1 Hahn Spin Echo Experiment and Theory[135,143]

The Hahn spin-echo experiment involves applying a $\pi/2$ and a π radio frequency pulse with a given time, τ, between the pulses. The 90° pulse flips the magnetization of the spin, and the spin decays as described in the previous section. After a time τ, a second 180° pulse is applied in the x- or y- direction and the spins are inverted.[136] This step ensures that the slowly revolving and faster spins will realign. After a second period of τ, the spins realign to form an echo time (TE) that has a maximum amplitude at 2τ after the

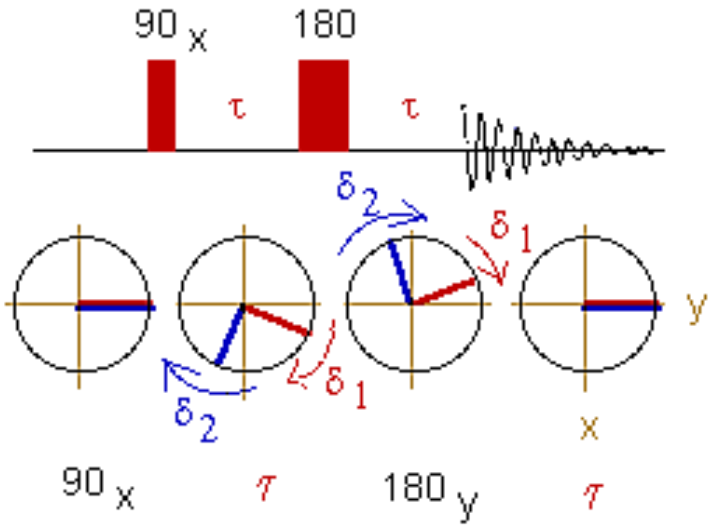

Figure 4-4. Cartoon of the pulse sequence, timing, and echo response of the Hahn spin-echo experiment where δ_1 represents the slower and δ_2 the faster spin.[144]

first applied pulse.[135,139] This sequence is depicted in the diagram of **Figure 4-4**.[144] The Hahn echo measurements also show unique relaxation measurements for each mobility domain; however, while the FID can show an increase in signal, the relaxation decay is monotonically decreasing.

The advantage of using the spin-echo pulse sequence is that it refocuses the dephasing of magnetization caused by the chemical shift and by magnetic field inhomogeneities. Therefore, the spin-echo provides a more reliable way to measure the dipolar coupling of components with longer relaxation times. It is also important to note that it is not possible to measure very short relaxation processes in the order of a few microseconds with the spin-echo sequence, because of the duration of the rf-pulses and associated switching times.

4.3.2.2 Relaxation Theory Applied to Polymers and Composite Systems

Polymeric materials are rarely found to be perfectly homogeneous, and often have motional or structural inhomogeneities on the order of nm to μm in scale.[137] Because of this, NMR is an ideal probe for examining the characteristics of polymer and composite systems since it is based on short range interactions and measuring properties on the molecular scale.[137] Previous work in the literature has used spin relaxations to study the dispersion of clays in polymer-clay nanocomposites,[145,146] the size of crystalline domains in semicrystalline polymers,[147] and ^{1}H residual dipolar couplings have been used to characterize anisotropic motion and crosslinking densities.[139,148]

Specifically, T_2 or transverse relaxation measurements are able to probe changes in the type and magnitude of nuclear dipolar interactions that occur with molecular motion.[137,149] ^{1}H-NMR is sensitive to the dipolar magnetic interactions of protons, the local fields from residual susceptibility, and chemical shift of the atoms that are dependent on the position of the polymer and functional groups in relation to each other. Therefore, T_2 relaxation is strongly influenced by the mobility of the polymer chain.[138,149,150] When the polymer is in a constrained environment, the dipolar interactions are more significant, and there is a shorter timescale of spin relaxation.[137,151] Oppositely, when a polymer is more flexible, the increase in motion causes atoms to interact less frequently and spin-spin relaxation occurs at a longer timescale.[137]

4.3.2.3 Model Systems

It has been proposed that composite systems can be approximated by three types of polymer environments: a rigid (possibly crystalline), intermediate, and mobile polymer

environment.[137,141,150] Since NMR can observe changes in motion on local spatial scales, the properties of these regions can be resolved on a very small scale. Three commonly studied systems will be briefly reviewed below for a background on the specific polymer interactions that might be present in MMM systems: cross-linked polymer systems, rubbery composite systems, and semicrystalline polymers.

Crosslinked polymers

Cross-linked, elastomeric polymer systems have been studied with NMR to further understand the effects of polymer anisotropy and constraint on relaxation time. In crosslinked polymers, relaxations that occur within the first millisecond typically come from interconnected, crosslinked sections, while the relaxations beyond that time are attributed to uncrosslinked sections.[139] The different polymer mobilities and anisotropies within the crosslinked polymer can be further broken down into the polymer chain segments shown in **Figure 4-5** that relax at different time scales. Intercrosslink chains (1 on **Figure 4-5**) show rapid, small anisotropic motions with spin relaxations on the order of 10^{-8} s and slow isotropic motion of 10^{-3} s, the framework polymer (3 on **Figure 4-5**) on the order of 10^{-4} s, and dangling chains (2 on **Figure 4-5**) have isotropic

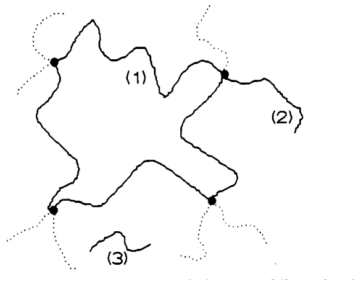

Figure 4-5. Diagram of possible mobile molecular parts of a crosslinked polymer system where: 1) inter-crosslink chains, 2) dangling chain ends, and 3) sol molecules. [138]

motions and time scales greater than 10^{-3} s.[138] It is important to note that the molecular/segmental motion of the polymer is also highly dependent on the temperature. More motion, and therefore a longer relaxation time, occurs in polymers at higher temperatures. Additionally, longer T_2 values are seen above the glass transition (T_g) temperature of the polymer (such as elastomers at room temperature) because the polymer exhibits the most flexibility above the glass transition.

Filled rubbers

When rubbery polymers are filled with a filler material, such as the ethylene propylene diene monomer (EPDM)/ carbon black composite system, the polymer shows a unique set of constricted or immobilized polymer domains that might not be present in the unfilled system. These regions are approximated as a rigid boundary region, an intermediate environment attributed to the interfacial region between the bulk polymer and bound rubber, and the mobile, bulk region. Each unique type of polymer conformation involved in forming these different polymer regions is noted and shown in **Figure 4-6**.[137,150] The observed NMR signal of the composite material

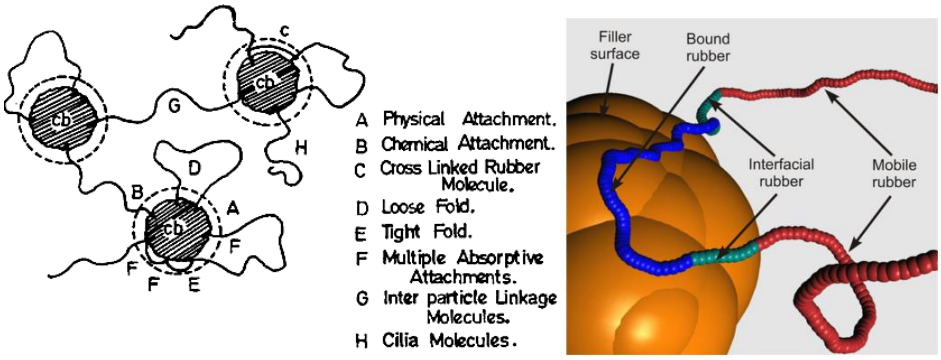

Figure 4-6. Illustrations of bound, interfacial, and mobile polymer segments in a rubbery composite material.[137,150]

represents a sum of the three components and the ratio of these three elements is highly dependent on the temperature of the system, polymer Tg, and nature of the polymer filler interaction.[141,150]

The rigid layer at the surface of the filler is attributed to highly adsorbed or immobilized polymer chains that have a reduced mobility compared to the bulk rubber.[137,150,152] The "bound rubber" region consists of an inner layer of approximately 1/5th of the total constrained layer thickness and "intermediate boundary" region that represents the balance.[137,141] The tighter the polymer is bound and the lesser mobility it shows, the faster the T_2 relaxation occurs. Thus, it has also been shown that the proportion of highly bound material increases with filler content as detected by T_2 intensities.[149] The "intermediate boundary" layer is the classification for the polymer that connects the bulk, mobile rubber region to the polymer tightly bound to the filler. The properties of this region are notably unique from the other regions because the polymer is more constrained than the bulk polymer material, while being significantly looser bound than the rigid boundary region. The rubbery region shows significant polymer motion and a ^1H spectral linewidth that is Lorentzian rather than Gaussian in shape.[137]

Crystalline polymers

The three component classification of polymer properties can also be applied to semi-crystalline polymers; however, the meaning of these three sections is markedly different than in a filled rubber system. Crystalline polymers consist of highly ordered and packed polymer chains. However, these features are often restricted to smaller domains of crystallinity that are connected by amorphous regions where the polymer is disrupted and

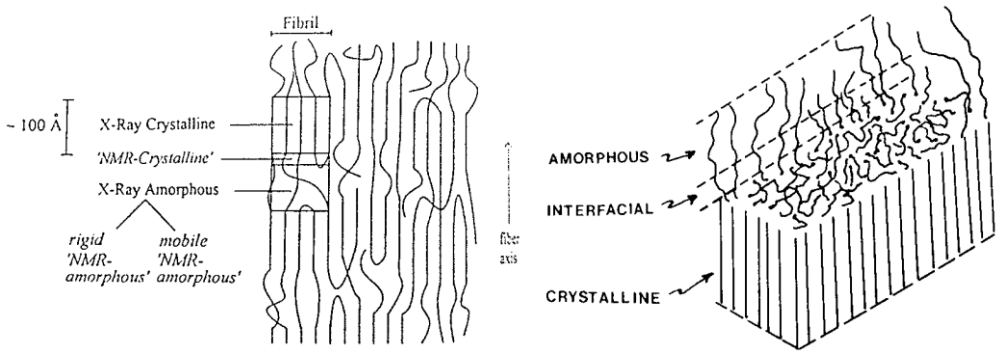

Figure 4-7. Figure of the type of crystalline domains in a crystalline polymer material.[153,154]

less tightly packed. A diagram of this is shown in **Figure 4-7** that emphasizes that amorphous regions can be broken down into different amorphous environments: rigid and mobile on the NMR scale.[153,154] The rigid amorphous comes from the boundary layer between the crystalline and mobile amorphous regions. This region shows greater polymer anisotropy due to folded chains and cilia anchored to the crystalline region that cause constrained polymer movement.[137] This example also demonstrates an advantage of NMR in probing crystallinity because it is able to probe crystalline regions that are less ordered than can be detected with XRD.

4.3.3 Methods and Results

Solid state relaxation time measurements were carried out using a 300 MHz Bruker DSX-300 NMR spectrometer operating at a magnetic field of 7.05 T and a static probehead. 30 wt. % loaded MMMs and pure polymer membrane (used in the gas permeation measurements in Chapter 3) were cut into small pieces and packed into a 7 mm (outside diameter) ceramic rotor. Single pulse ^{1}H NMR spectra were recorded at increasing temperatures from 23-190°C. 190°C was the maximum temperature of the instrument. During this heating process water was evaporating from the sample. This was

obvious from the loss of a highly mobile component attributed to H_2O, evident in the NMR spectra of Matrimid presented in **Figure 4-8**. The addition of a filler did not noticeably change the ^1H spectra. The ^1H spectra are included in the **Appendix B** for all membranes tested. Hahn spin echo data were taken while ramping down the temperature (after the water was removed) at 4 different temperatures of 190°C, 180°C, 100°C, and 30°C. Spin echo data were recorded at 32 echo times between 10 μs and 1 ms with an applied pulse length of 3.6 μs for the π/2 and 7 μs for the π pulse, 8 scans at each echo time, and a recycle delay of 5 seconds between scans. Data were analyzed using Bruker Topspin 1.3 software.

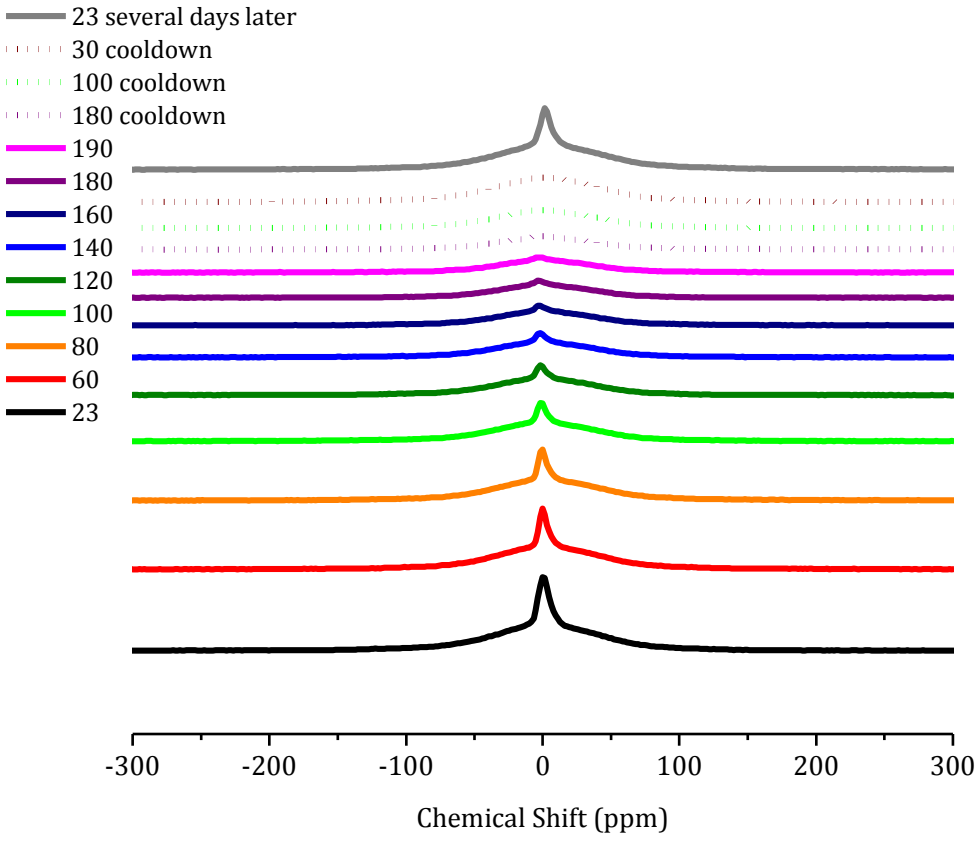

Figure 4-8. ^1H NMR spectra of Matrimid at increasing temperatures and cooling.

The T_2 relaxation curves are traditionally fitted with a Weibull function (**equation (4.6)**):

$$\exp\left(-\frac{t^{\alpha}}{T_2}\right) \tag{4.6}$$

where α=1 for a Lorentzian and 2 for a Gaussian fit of the NMR spectra.[149] However, upon examination of our data, it was determined that more than one fitting function was necessary. The specific fitting function for the initial relaxation data in this study includes both Lorentzian and Gaussian fits as shown in **equation (4.7)**: [149]

$$I = A_1 \exp\left(-\frac{(\tau)}{T_{2-1}}\right) + A_2 \exp\left(-\frac{(\tau)^2}{T_{2-2}}\right) + Y_0 \tag{4.7}$$

where I is the signal integral, τ is the decay time, and A represents the quantity of that component.

^{1}H spin-spin relaxation curves were measured for pure Matrimid polymer, a bare LTA MMM, and MMMs with all four functionalized LTA particles. A mixed matrix membrane fabricated with commercially available $Mg(OH)_2$ crystals and Matrimid was also tested to provide a comparison with the functionalized zeolite materials. Free induction decays (FIDs) were measured starting at the maximum of the spin-echo. Data were then Fourier transformed to obtain a series of spectra as a function of echo time TE (2τ). An example relaxation series is shown in **Figure 4-9.** The spectra were integrated over the entire spectral range observed and τ times to yield the relaxation curves shown in **Figure 4-9** and **Figure 4-11** for the six membranes at each temperature. A comparison

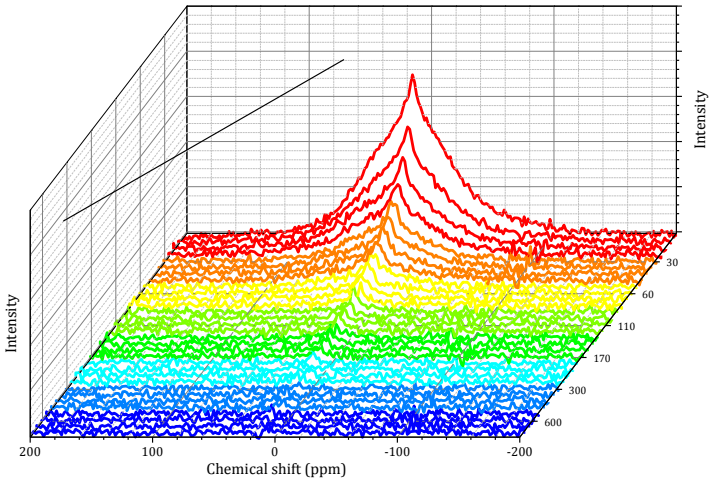

Figure 4-9. ^{1}H spectra at different τ times of a pure Matrimid membrane for calculating relaxation curves.

of the data for each membrane at 190°C is shown in **Figure 4-12** for a clearer comparison of the different types of membranes.

This data shows many interesting features that will be addressed in detail later in this chapter. Firstly, all membranes show an initial rapid relaxation rate that is complete by τ of 100-300 μs. This rapid relaxation corresponds to rigid molecules that do not undergo large-angle motion. This behavior is expected as the temperature is well below the polymer T_g of 310-315 °C.[155] Secondly, most of the relaxation curves show a variation in relaxation curve slope and shape with changes in temperature. An increase in temperature has the potential to make the polymer more mobile and thus cause the spin-spin relaxation properties of the polymer to change. Specifically, it can be seen that the pure Matrimid, ion exchange, and Grignard MMMs show the largest variation in relaxation properties with temperature over all measured τ times. Lastly, all functionalized LTA particles and the $Mg(OH)_2$-Matrimid MMMs show an inflection point (i.e. a change in slope indicated by an arrow on the figures) in the relaxation curve at a τ ~50 μs, a feature that is not present in the pure polymer or the bare LTA MMM.

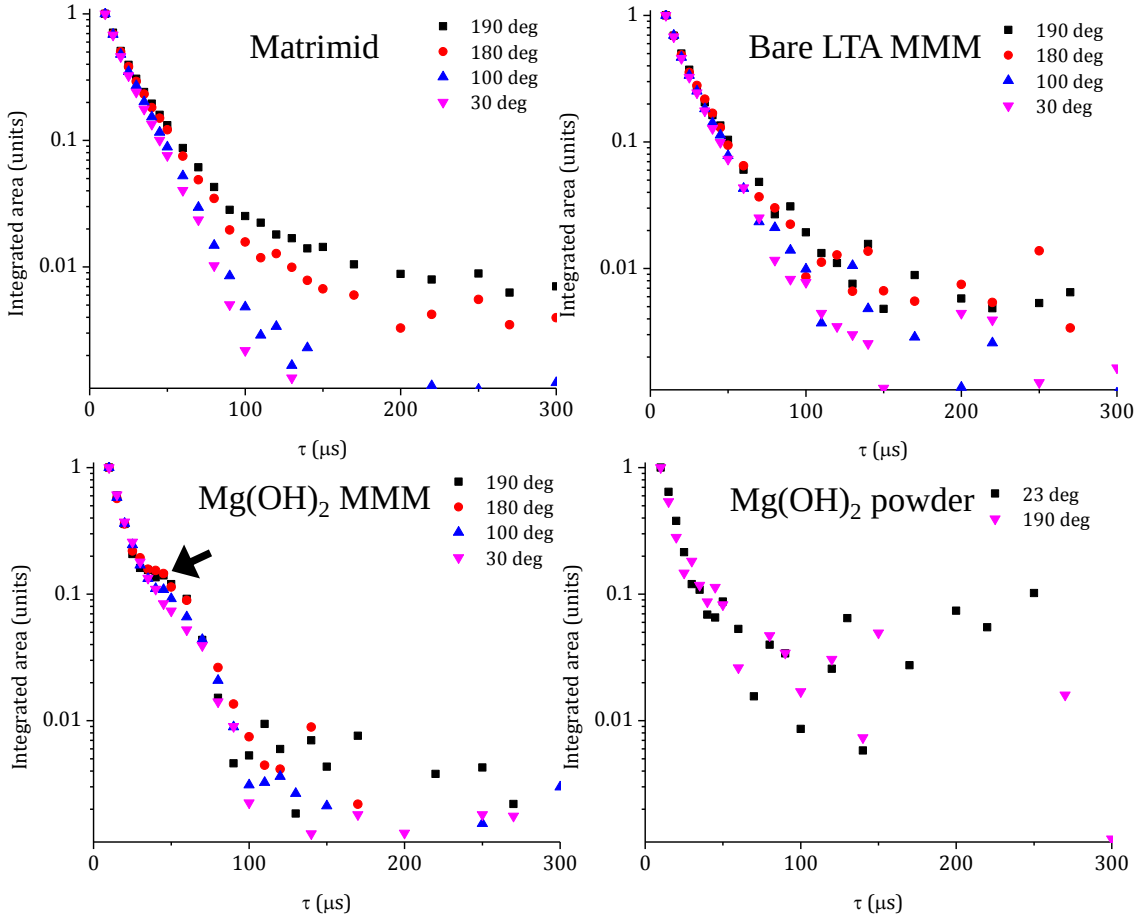

Figure 4-10. T_2 relaxation curve for Matrimid, bare LTA MMM, $Mg(OH)_2$ MMM, and pure $Mg(OH)_2$. The arrow indicates a unique inflection point present only in Mg-containing samples.

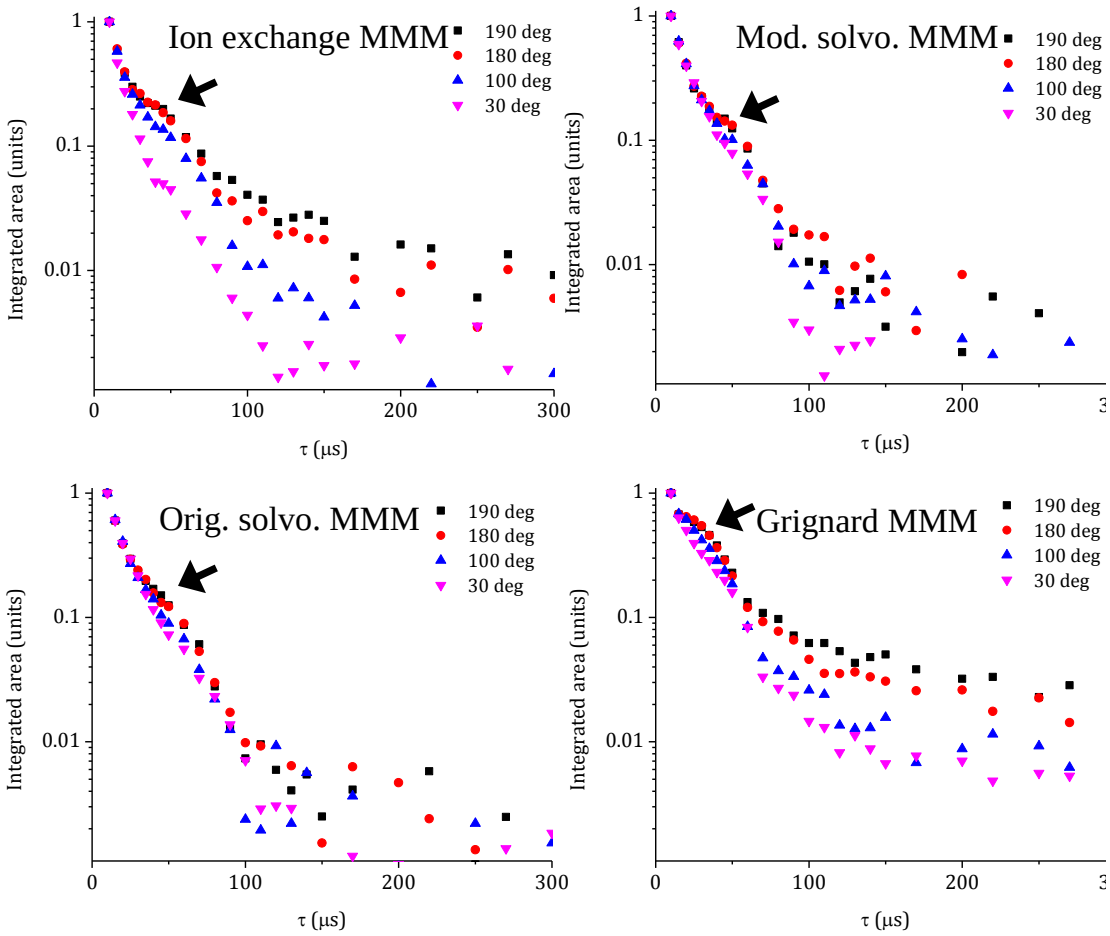

Figure 4-11. T_2 relaxation curve for MMMs made with ion exchange, modified solvothermal, original solvothermal, and Grignard functionalized LTA. The arrow indicates a unique inflection point present only in Mg- containing samples.

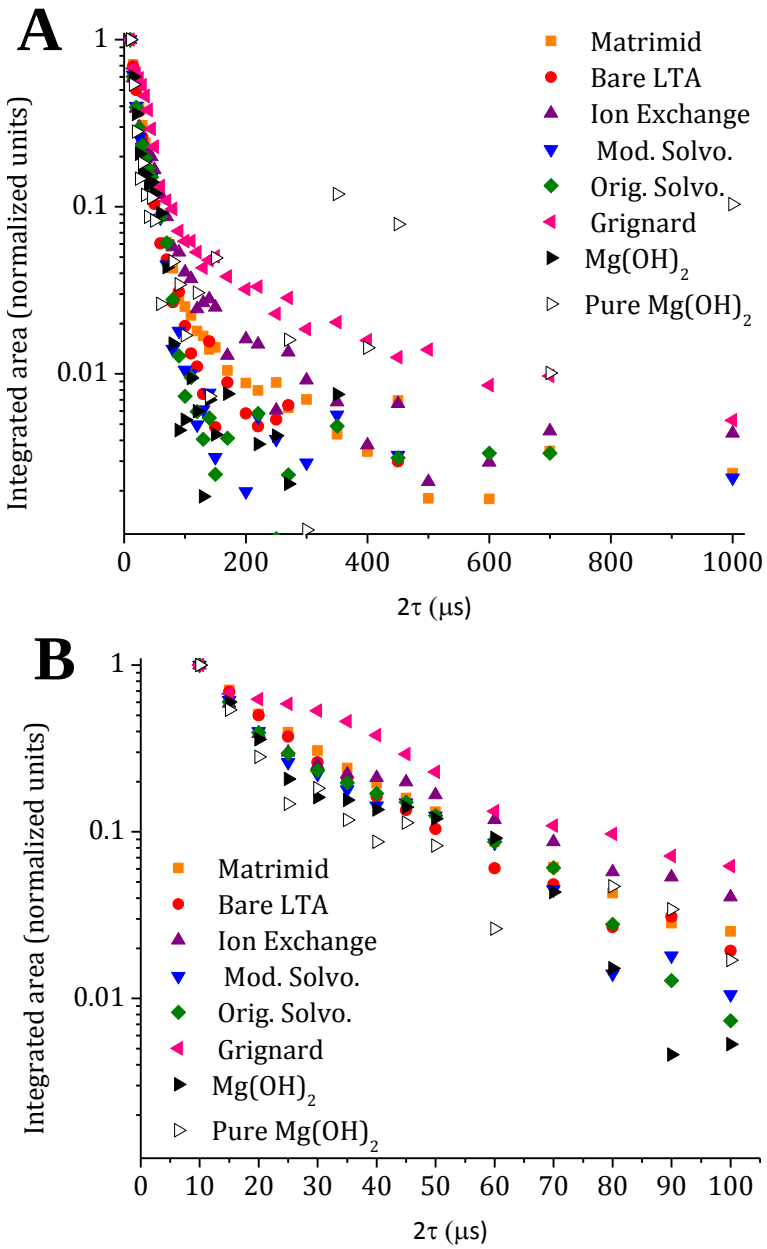

Figure 4-12. Spin-spin relaxation curve for all MMMs at 190°C. A) Full dataset B) emphasis on the early relaxation behavior.

The initial part of each relaxation curve is fitted with **equation (4.7)** up to τ ~100 µs. The polymer beyond this point is considered to be the mobile fraction (as will be defined later in the section), but is not specifically fitted because of the scatter in some of the measurements. Within 100 µs, all relaxation curves fit well and converged to **equation (4.7)** except for the Grignard MMM where the relaxation curves at 100, 180 and 190°C were too different to be fit with this model. The calculated spin-spin relaxation times ($T_{2\text{-}1}$ and $T_{2\text{-}2}$) and the ratio of quantities of each T_2 component representing the rigid to intermediate components (A_1/A_2 values from **equation (4.7)**) are plotted in **Figure 4-13** and **Figure 4-14**, and the specific values are in the appendix in **Table B-2**.

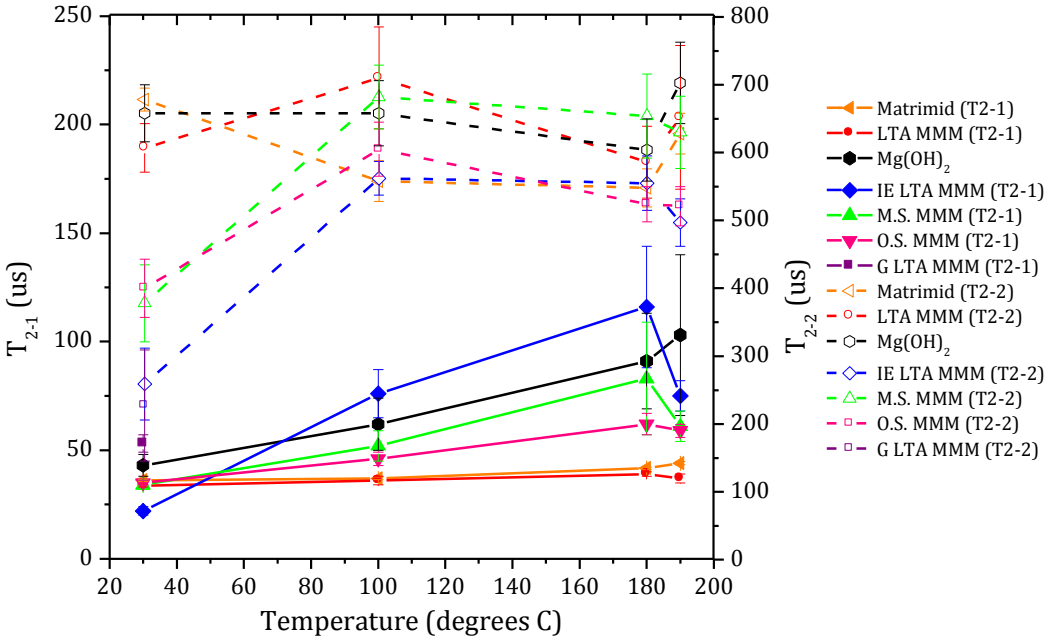

Figure 4-13. The fitted $T_{2\text{-}1}$ and $T_{2\text{-}2}$ relaxation times for all membranes at the four temperatures. The solid lines/markers correspond to $T_{2\text{-}1}$ and dashed lines/open markers correspond to $T_{2\text{-}2}$.

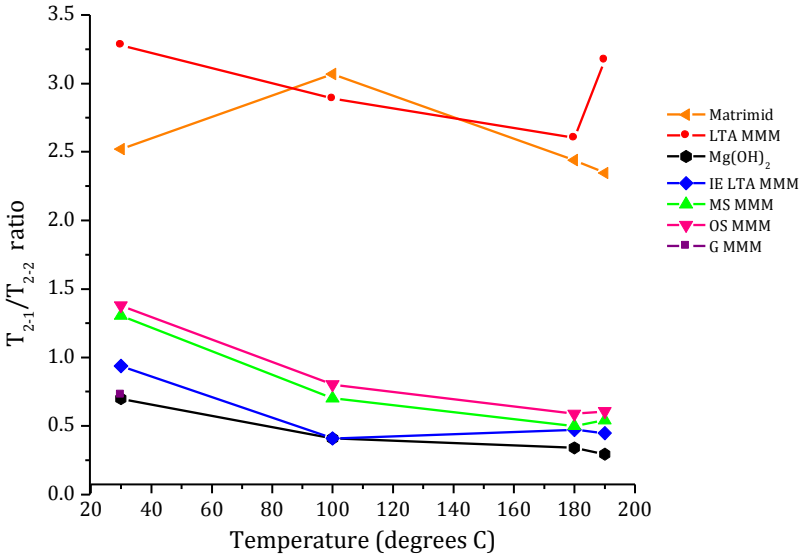

Figure 4-14. The ratio of $T_{2\text{-}1}/T_{2\text{-}2}$ components determined by A_1 and A_2 in equation (4.7) for all membranes at the four temperatures. These values represent the rigid/ intermediate portion.

The activation energy (ΔE*) of the polymer can be estimated by **equation (4.8)**:

$$\Delta E^{*} = -R\left[\frac{\delta \ln(T_2)}{\delta 1/T}\right]_1 \qquad (4.8)$$

where T_2 is the spin-spin relaxation time, T is the temperature in Kelvin, and R is the ideal gas constant of 8.314 K/mol•K.[156,157] The use of this equation is based on the assumption that the correlation time (τ_c) << $(\gamma\langle\Delta H^2\rangle)^{-1/2} \cong 10^{-5} sec$ where γ is the gyromagnetic ratio and $\langle\Delta H^2\rangle$ is the second moment of absorption. Correlation times were not directly measured for this polymer but were on the order of 10^{-11} seconds for the main chain movement of poly(ketone-imide) and poly(ether-imide) which are similar in structure to Matrimid.[158] An Arrhenius plot of the relaxation data is shown in

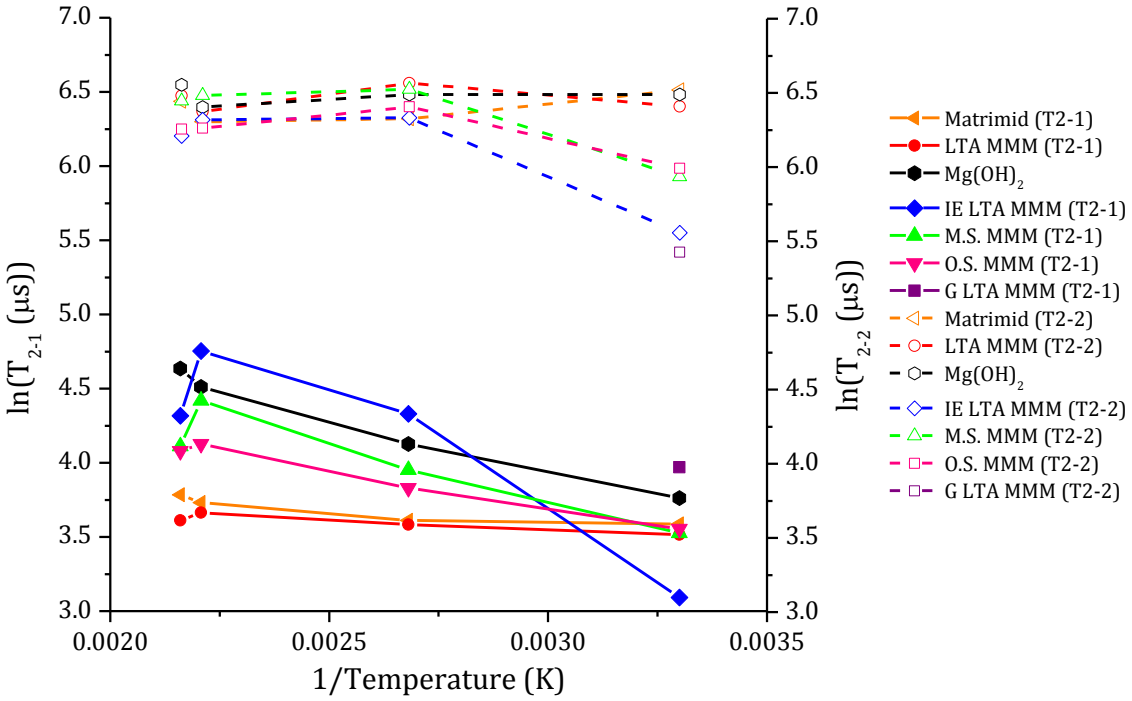

Figure 4-15. Arrhenius plot of T_2 relaxation data.

Table 4-3. The activation energies (ΔE*) of the two fitted regions in each membrane material.

	ΔE, T_{2-1} (KJ/mol)	**ΔE, T_{2-2}** (KJ/mol)
Matrimid	1.3	-1.7
LTA MMM	0.9	-0.1
$Mg(OH)_2$ MMM	6.1	-0.6
Ion exchange MMM	10.2	6.0
Modified solvothermal MMM	5.4	4.3
Original solvothermal MMM	4.1	2.2
Grignard MMM	X	X

Figure 4-15. This data was fitted with a line from 30-180°C. The 190° points were not included because they were not continuous. The resulting activation energies are shown in **Table 4-3**.

4.3.4 Discussion

The glassy polymer used in this work, Matrimid, is an amorphous poly(imide) with a T_g well outside the temperatures used in this experiment. The polymer consists of domains of chains that are packed in a tight, linear fashion and do not exhibit large angle motions.[137,139] The polymer exhibits π-stacking properties due to its aromatic character. Different functional groups on the polymer result in electron donating or withdrawing character of π-stacking interaction as illustrated in **Figure 4-16**. This leads to a region with a high packing density, a low free volume (void spaces) region, and a rigid and oriented, but non-crystalline, conformation.[155] This region is illustrated in **Figure 4-17** as the *R* domain. If the stacking interaction between the polymer chains is disrupted, the regions will exhibit poor packing and a high free volume. In the disrupted domains, the polymer is not restricted and can move as freely as the intrinsic

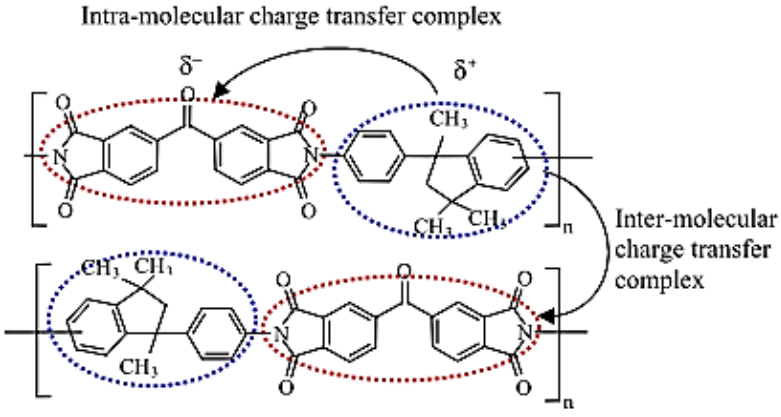

Figure 4-16. Schematic of Matrimid polymer's electron donating and withdrawing groups forming inter- and intra-molecular charge transfer complexes.[155]

chemical structure of the polymer allows to form the 'mobile' component of the polymer (**Figure 4-17)**. However, due to the high ratio of aromatic and heterocyclic imide groups, the chain is not highly flexible. These 'mobile' domains are analogous to, but more rigid than, rubbery polymers at room temperature (which have a T_2 relaxation time on the order of 10^3-10^4 μs, or 10-100 times slower than the Matrimid rigid domains).[149] The mobile water was removed during heating as it is no longer evident in the ^{1}H spectra; however, a less mobile, physisorbed water phase may still be present and contribute to the mobile component. The mobile component is not explicitly fitted in this work because there is a lot of noise for several of the membranes in that section of the relaxation curve, thus effects from adsorbed water were negligible on the fitted parameters. Lastly, there is evidence of an intermediate region that shows relaxation characteristics distinct from both the mobile and rigid environments. This region represents a partially hindered

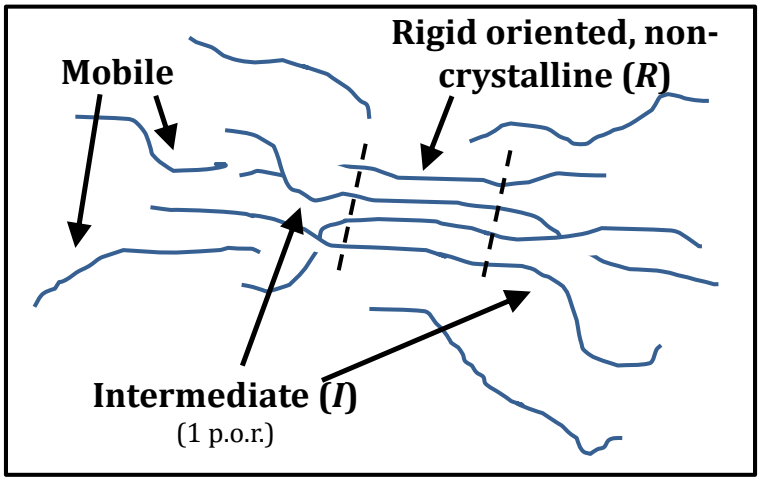

Figure 4-17. Illustration of three domains present in pure glassy polymer system. The glassy region is the ordered section of the polymer between the two lines, while the intermediate region consists of the polymers outside the dashed lines.

polymer with anisotropic motion and can include the remaining loose section of a polymer chain that forms a rigid ordered domain (**Figure 4-17-*I***).[137] In this work, only the rigid and intermediate domains were characterized in the early portion of the relaxation curve due to noise in the mobile component.

In the pure polymer, as well as the bare LTA and $Mg(OH)_2$ MMMs, the relaxation of the polymer occurred with a T_2 of ~40 μs and an intermediate relaxation time of ~600 μs (the remaining mobile component was not fitted). The pure polymer and bare LTA MMM show the same relaxation properties, with the same decay times, and a rigid/ intermediate ratio of 2.5-3.5. The $Mg(OH)_2$ MMM shows similar initial relaxation times to the pure polymer and bare LTA MMM at 30 °C. However, at 190°C, the relaxation time of its rigid section increases from 43 to 103 μs, and the intensity ratio of rigid to intermediate components decreases from 0.7 to 0.3. The $Mg(OH)_2$ MMM also has a smaller rigid: intermediate fraction compared to the pure polymer and the bare LTA MMM. Lastly, the rigid ΔE^* is 6.1 kJ/mol compared to 1.3 kJ/mol for the pure polymer. These four observations indicate that when $Mg(OH)_2$ is present, the polymer becomes more mobile and plasticizes more easily with increasing temperature. This plasticized region can also be observed qualitatively by the inflection point in **Figure 4-10** mentioned previously. The relaxation curve for $Mg(OH)_2$ powder in **Figure 4-10** does not show an inflection point similar to that seen in the $Mg(OH)_2$ MMM though there is a slight inflection point at approximately 90 μs. The relaxation for the pure zeolite LTA (appendix **Figure B-9**) also does not show this unique inflection point present in the nanocomposite membranes, nor does it show any other inflection point. This rules out the possibility of the $Mg(OH)_2$ protons causing the inflection through additive effects. This

suggests that the interactions due to the chemical nature of $Mg(OH)_2$ have a direct impact on the polymer properties, especially at higher temperatures. In Section 4.2.3, the basicity of MgO had a strongly negative impact on the quality of adhesion between the two phases. Since $Mg(OH)_2$ shows the same basic character as MgO, a lack of interactions between the basic mineral and slightly basic polymer lead to a weak interface. At higher temperatures, enough energy is put into the system to overcome the H^- and VDW bonding without additional strength from acid-base interactions.

The $Mg(OH)_2$-Matrimid membrane was used to determine how the chemical nature of the filler material can impact the polymer properties. Qualitatively, the functionalized LTA MMM systems show behavior much more similar to the $Mg(OH)_2$ MMM than to the bare LTA MMM (**Figure 4-11** and **Figure 4-12**). This suggests that the presence of the surface nanostructures impact the polymer properties beyond the previous hypothesis of simple physical entanglement and dispersion forces This interaction can be broken down further into: (1) steric interruptions of polymer packing due to the shape of the nanostructures and the additional surface area they provide, and (2) changes in polymer mobility or conformation likely due to the chemical interactions between the nanostructure and the polymer. Each of these interactions will be further explained in the following sections.

The largest change in polymer packing (upon incorporation of nanostructures) occurs in the intermediate region. At 30 °C, the intermediate region shows a steep decrease in relaxation time ($T_{2\text{-}2}$) with respect to the bare LTA or $Mg(OH)_2$ MMM $T_{2\text{-}2}$ times. This shows that at this temperature, the unique interactions between $Mg(OH)_2$ and the polymer due to the chemical nature of the interacting species are not significant.

Instead, the shape and coverage of the nanostructures contributes more to packing and confinement of the polymers because the relaxation curves do not resemble the $Mg(OH)_2$ MMM. This confinement occurs by 1) packing the intermediate domain tighter due to a physical obstruction, and 2) increased immobilization of the mobile or intermediate regions through physical adsorption of the polymer as illustrated in **Figure 4-18**. This also causes more of the mobile phase to be classified as an intermediate phase. At low temperatures, the polymeric motion is already minimal. However, in the nanostructured systems, the packed polymer is also restricted to smaller regions between the nanostructures. When the polymer is confined to this small space, it is more likely to physisorb to the nanostructures or zeolite because of its proximity and the increase in available surface area to attach to. These physisorption interactions occur because of VDW forces and therefore are more dependent on the quantity of surface area than the

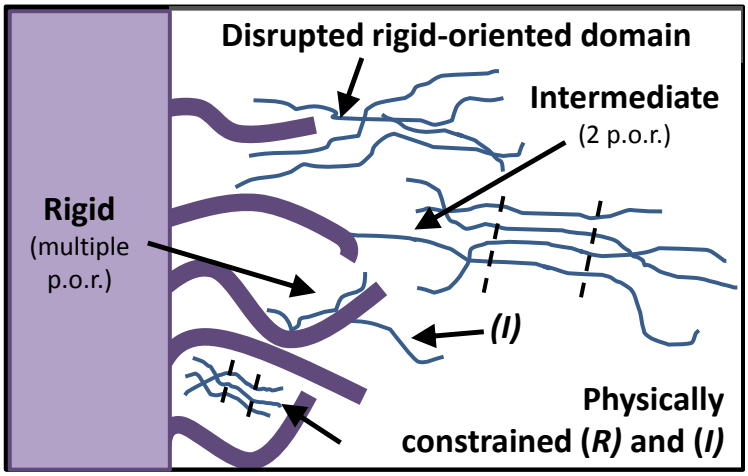

Figure 4-18. Illustration of the types of local polymer environments in a functionalized zeolite MMM system. (R) is the rigid, oriented, noncrystalline polymer domain and (I) is an intermediate domain where the polymer has one point of restraint (p.o.r.).

type of surface present. These physisorbed polymer regions create points of restraint and cause anisotropic motion of the polymer and more rigidity. In particular, there is a decrease in lifetime of the intermediate $T_{2\text{-}2}$ component compared to the pure polymer and bare LTA MMM at 30 °C. With increased temperature, the intermediate $T_{2\text{-}2}$ returns to that of the pure polymer. This occurs because the physical adsorption of polymers on the zeolite/nanostructure is relieved when a small amount of energy overcomes the weak, secondary forces holding the polymer in place. The anisotropically pinned polymers are able to break free of their points of attachment and the polymer approaches its original dynamical state.[159] It is important to note that the nanostructure can also disrupt interchain interactions that align the polymer and create the glassy portion of the system contributing to the decline in the amount of rigid polymer. This is observed by the rigid ($T_{2\text{-}1}$) shift to more intermediate ($T_{2\text{-}2}$) packing as indicated by the lower rigid-to-intermediate component ratio.

Quantitatively, the fitted values in **Figure 4-13** and **Figure 4-14** show the functionalized LTA MMMs have a larger change in relaxation properties with temperature than unfunctionalized LTA. The rigid portion of the polymer/inorganic composite is slightly different than that of the pure polymer. It can come from the interfacial region between the filler and the polymer and it is expected (and observed) that this type of environment would be more highly impacted by specific chemical compatibility issues. The rigid portion can come from the rigid ordered domains (as seen in the pure polymer) and new rigid domains created when polymers adsorb on the nanostructures (or zeolite) and have many points of restraint which does not facilitate spin transfer. Functionalization causes the same $\Delta T_{2\text{-}1}$ and ΔE^* trends with temperature

that was seen in the $Mg(OH)_2$ MMM. Thus, the MgO_xH_y nanostructures also plasticize the polymer, especially at higher temperatures, because of their surface nanostructure-polymer chemical interactions.

In the pure, LTA-polyimide system, there are Lewis and Brönsted acid-base interactions between the zeolite and the polymer as seen by Lee et al.[124] However, because the polymer is only slightly electron donating, these bonds should not be very strong. But the Brönsted acid-base interactions present have the potential to have up to 1000 kJ/mol bond energies. This type of interaction is much more significant than the other bond types that participate in adhesion including H-bonding (<40 kJ/mol) or Van der Waals forces (<10 kJ/mol). $Mg(OH)_2$ and MgO, on the other hand, are very basic (e^- donating). Because both the polymer and nanostructure show the same electron donating properties, nanostructure-zeolite interfaces will have Van der Waals and possibly H-bonding interactions (< 40 kJ/mol). But, once energy is applied to the system to overcome those secondary interactions, the basic character of each species may repel each other leading to the polymer motion observed in higher temperature systems in Mg based systems.

The four individual functionalization methods show only slight differences from each other. The modified and original solvothermal methods show very similar relaxation characteristics (both in shape and in fitted relaxation times) to each other and to the $Mg(OH)_2$ MMM. Specifically, these three MMMs show the same intensity and position of the inflection at 60 μs. The ion exchange (IE) MMM shows a higher degree of confinement at 30°C than the other functionalization methods, as indicated by the relaxation times. This observation is reasonable since the IE also shows good surface

functionalization on the surface (Chapter 2). Qualitatively, the IE MMM also shows the inflection, and also a slower-relaxing polymer phase beyond the inflection point at higher temperatures in comparison to the other functionalization methods. The Grignard MMM shows similar behavior at 30°C to the IE method in terms of the rigid: intermediate ratio and intermediate relaxation lifetime, though the rigid lifetime is significantly higher. However, when the membrane is heated, the relaxation curve changes in shape, especially at the 0-50 μs range, which prevents reliable curve fitting with **equation (4.7)**.

Lastly, the activation energies of the rigid and intermediate domains were calculated and shown in **Table 4-3** and have been alluded to throughout the chapter. These activation energies reinforce the theories explained throughout this chapter of the increased temperature dependence of MgO_xH_y containing membranes. The pure polymer and bare LTA MMMs (ΔE^* = 1.3 and 0.9 KJ/mol) which is similar to activation by thermal motion ($RT = \Delta E^*$ =2.48 KJ/mol at 25°C) in these domains. However, the $Mg(OH)_2$, modified solvothermal and ion exchange MMMs showed greater activation energies (ΔE^* = 6.1, 5.4, and 10.2) indicating that other factors are contributing to the ΔE^* as well.

4.4 Mechanical properties

4.4.1 Theory

Tapping mode atomic force microscopy was used to map the mechanical properties of membrane cross sections and image topological features simultaneously. Tapping mode has the advantage of eliminating plastic deformation of the sample and reducing the sample volume that interacts with the tip, thus greatly improving the spatial resolution.[160] It is difficult to determine the mechanical properties of a material by

tapping mode itself. Therefore, Harmonix mode on the AFM was used to determine these properties. In conjunction with a special mode, specifically designed torsional cantilevers **(Figure 4-19**) that have an offset tip location were used that allow both flexural (mostly ±Y signal from the cantilever oscillation) and torsional deflections (mostly ±X signal

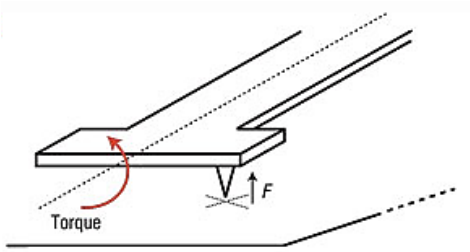

Figure 4-19. HarmoniX cantilever with an offset tip location. [160]

due to a change in force response on the offset tip).[160] This tip design was used to maximize the signal to noise ratio of the higher harmonic cantilever vibrations and the frequency response that was used to extract the mechanical data. The HarmoniX method uses the applied force on the tip to determine the elastic modulus based on the following relationship:

$$F_{tip} = \frac{4}{3} E^* \sqrt{R}\, d^{3/2} + F_{adh.} \qquad (8.1)$$

where F_{tip} is the sample-tip force, E* is the reduced Young's modulus, R is the tip radius, d is the indentation depth and F_{adh}. is the adhesive force between the tip and sample.[160,161] During the calculation, the Derjaguin-Muller-Toporov (DMT) model was used and the adhesion was assumed to be constant during the indentation.[160,161] The measurements in this chapter were left in arbitrary units because the actual elastic

properties of the material (especially in the case of soft materials) is highly dependent on the indentation depth.[162]

4.4.2 Experimental methods

HarmoniX mode was used with a Nanoscope Dimension 3100 AFM equipped with a Nanoscope V controller and Nanoscope software Version 7.3. All measurements were made under ambient conditions at room temperature. HMX AFM probes with a nominal tip radius of 10 nm, tip length of 4.5 μm, cantilever length of 200 μm and tip offset of 17 μm were used for the measurement. The data was analyzed using Bruker NanoScope Analysis software. Prior to imaging, the cantilever spring constant was determined using thermal tuning and the AFM photodetector sensitivity was calibrated by measuring force curves on a silicon sample.

The samples were made by fixing a 1 cm^2 section of the 30 wt. % loaded MMMs and pure polymer membrane as used in the NMR measurements to a glass slide with a thin layer of Superglue and drying the sample overnight. Samples were polished using Ted Pella diamond pastes in the following order of grain sizes: 3 μm, 1 μm, and 0.25 μm for approximately 5 minutes each to smooth the surface and expose a cross section.

4.4.3 Results

Mechanical measurements were mapped simultaneously with the sample height, phase, adhesion and dissipation of the sample and maps of these properties are shown in **Appendix B** for all five mixed matrix membranes. The elastic modulus measurements are summarized in **Figure 4-20** and the topological images in **Figure 4-21**. In each elastic modulus map, the zeolite particle is the lighter portion of the image and the polymer is

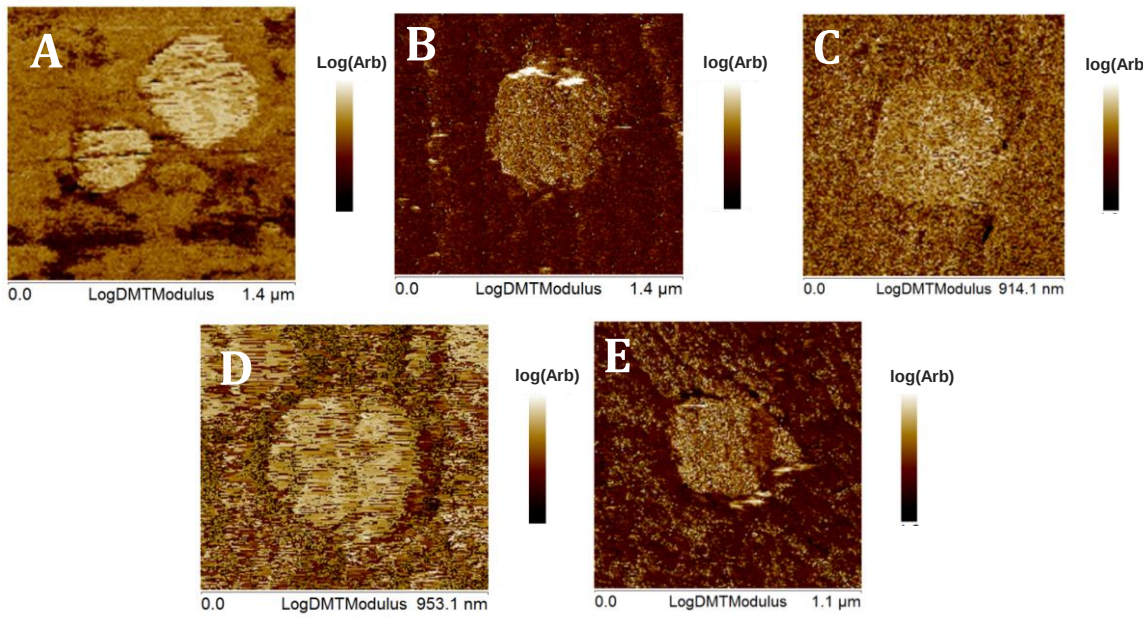

Figure 4-20. log (Modulus) of cross sections of a bare LTA MMM (A) and B)ion exchange, C) modified solvothermal, D) original solvothermal, and E) Grignard functionalized LTA MMMs.

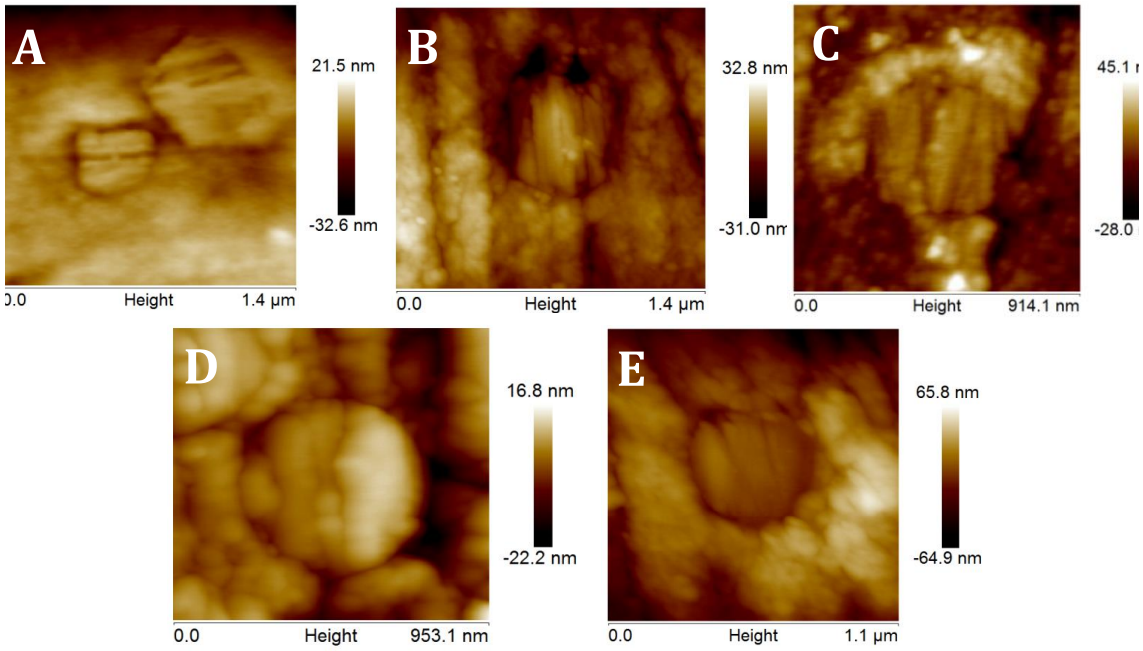

Figure 4-21. Height of cross sections of a bare LTA MMM (A) and B)ion exchange, C) modified solvothermal, D) original solvothermal, and E) Grignard functionalized LTA MMMs.

the darker portion. This agrees with the intuitive difference of mechanical properties for each phase where the zeolite is much harder than the polymer. The functionalization itself is not discernible in the images at the edge of the zeolite. However, the functionalization does cause a change in the density and elastic modulus of the polymer as seen by the differences in polymer interface properties between the different methods. The bare LTA, ion exchanged LTA, and modified solvothermal LTA (**Figure 4-20-A-C**) show a constant polymer modulus extending from the zeolite. The bare LTA membrane does have weaker regions of polymer that do not reflect a change in height indicating that the pure zeolite may contribute to a lower quality membrane but that the zeolite surface itself does not change the properties of the polymer at the interface. Additionally, the topographical image in **Figure 4-21-A** (or the 3D image in **Figure B-4)** shows the presence of a void between the phases that has been seen previously in SEM and TEM images in Chapter 3. The modified solvothermal and ion exchange functionalization methods also reflect a constant elastic modulus of the polymer surrounding the zeolite similar to the bare LTA membrane. This supports that the surface nanostructures of these methods do not significantly disrupt the polymer packing on the scale of tens of nanometers observable with this method. However, the original solvothermal and Grignard functionalization do not appear to show the same smooth transition. They have a lower elastic modulus region surrounding the particle of approximately 20-100 nm for the original solvothermal and 30-70 nm for the Grignard. This suggests that the nanostructures in these methods do disrupt the packing at the interface. Furthermore, they show a greater variation in the elastic modulus of the polymer itself even outside of this interfacial region. This most likely results from the excess in free functionalization that is

not attached to the zeolite. The Grignard and original solvothermal also show evidence of a gap in the topographical image similar to the gap present in the bare LTA MMM.

The lack of change in polymer crystallinity in the bare LTA MMM and pure polymer is consistent with the NMR results. However, the functionalization methods themselves do not show significant differences among themselves in NMR and thus the functionalization differences cannot be directly compared to the mechanical mapping results. The mechanical mapping does correlate to the quality of the nanostructures and their coverage that was determined in Chapter 2 confirming that more outward pointing nanostructures with more surface area are better at integrating into the polymer structure.

4.5 Conclusions

In conclusion, NMR spin relaxation measurements have led to significant insight into the interfacial interactions of the polymer with the surface nanostructures. It is shown that there are both steric and chemical contributions to the interaction between functionalized LTA and the polymer in MMMs. Firstly, the more confined polymer environment in functionalized MMMs due to the nanostructure presence was indicated by lower relaxation times at low temperatures. Secondly, an increase in the change in relaxation time (and curve shape) of the functionalized LTA MMMs with applied temperature that resembled that in a pure $Mg(OH)_2$ membrane showed the influence of specific chemical interactions due to the nature of the MgO_xH_y nanostructures.

The specific interactions include physical interlocking of the polymer. Additionally, it is suggested that the chemical bonding interactions such as H-bonding, Van der Waals forces and, in the case of the zeolite materials, acid-base interactions are present as well. It was hypothesized that the MgO_xH_y nanostructures showed poor

adhesion with the polymer because both the nanostructure and the polymer have electron donating properties and most likely repel each other.

Mechanical mapping of a cross section was able to show a difference in the nanometer-scale properties of the polymer in MMMs that supports the NMR study and provides additional information with respect to the influence of the nanostructuring methods. It confirms that the ion exchange and modified solvothermal methods resulted in the highest quality functionalized LTA MMM materials (though this does not necessarily reflect its gas separation performance).

5 Conclusions and Future Work

5.1 Summary

The theme of this work is improvement of the interface between zeolites and polymer in mixed matrix membrane composites via zeolite surface functionalization. Four methods of inorganic deposition on zeolites have been thoroughly characterized and their potential in MMM predicted. Then, the surface functionalized zeolites were used in Matrimid-based MMMs and the dispersion of zeolites, mechanical properties of the composite, and gas permeation were determined and, if possible, correlated to the nanostructure properties and their predicted potential. Lastly, the interface between the two materials was studied on a more local scale to show that the presence of nanostructures significantly changes the environment in the polymer.

5.2 Conclusions

In Chapter 2, inorganic surface structures were deposited on zeolite MFI and LTA using four surface deposition methods: Grignard decomposition reactions (G), solvothermal and modified solvothermal depositions (OS and MS), and ion-exchange induced surface crystallization (IE). These functionalized zeolites were then systematically characterized with XRD, SEM and TEM, elemental composition, and nitrogen adsorption. This thorough characterization showed that the nanostructures were MgO_xH_y in nature and each method produced its own unique nanostructure shape, size and coverage. The original solvothermal method in particular resulted in an excess of unattached functionalization. In contrast, the ion exchange method showed very good coverage of nanostructures with very little magnesium. In addition, the OS and G

methods had loosely attached nanostructures laying on the surface while the ion exchange and modified solvothermal methods appeared well attached. Lattice fringes confirmed all methods with the exception of the IE showed at least partial crystallinity. Nitrogen adsorption confirmed a significant addition of surface area for the OS and IE methods and a slight increase in the MS compared to the unfunctionalized LTA thus providing a method of quantifying the nanostructure surface roughening. The porosity decreased significantly for the two solvothermal methods because of pore blocking contributions from the solvent and nanostructures. Pure silica MFI reflected similar trends to the aluminosilicate LTA; however, the nanostructure shape and coverage were different for the two solvothermal methods. This indicates that the surface chemistry of the zeolite substrate impacts the resulting nanostructure shape and growth. From a summary of all the characterization, the ion exchange method was hypothesized to show the best gas separation properties.

Chapter 3 presented the use of functionalized zeolites in Matrimid MMMs. Cross section TEM showed that the polymer may have trouble penetrating into the nanostructures of the modified solvothermal method resulting in a reduced but not fully eliminated void between the phases. A quantitative assessment of dispersion in the membrane showed that all surface functionalization resulted in a better distribution than the bare LTA but that the modified solvothermal consistently showed the best MMM dispersion. Measurement of the elastic modulus and hardness of the membranes showed that all MMMs had better mechanical properties than pure polymer regardless of the presence of functionalization or specific functionalization method. The average elastic modulus values remained the same with increased particle loading but the distribution of

data greatly widened. Thus, at higher weight loadings, there was greater inhomogeneity in the membranes. The mechanical properties and dispersion had no correlation indicating the actual interfacial interaction due to the nanostructures is more important to the membrane properties. CO_2/CH_4 gas permeation corroborated that the higher weight loaded membranes were poorer in quality because they lack improvement in separation properties compared to lower loaded membranes as would be theoretically predicted. However, at the 15% wt. loading, the ion exchange MMM significantly improved the selectivity with a minimal change in permeability compared to the pure polymer or unfunctionalized LTA MMM. This membrane performance matches the hypothesis of the most appropriate zeolite functionalization method put forth in Chapter 2.

In Chapter 4, the interfacial characteristics of the polymer were studied. ^{1}H NMR transverse-relaxation studies were conducted on the pure polymer, functionalized and bare LTA MMMs, and a $Mg(OH)_2$ MMM. This technique was able to probe the polymer characteristics on a molecular scale and was able to resolve the interfacial region that occupies only a small volume of polymer. This experiment showed that the nanostructures had a significant impact on the polymer properties in the MMM 1) by disrupting and confining the polymer by its shape and physical characteristics and 2) by forming weaker bonds with the polymer due to the specific MgO_xH_y. It is believed that this occurs because the basic MgO_xH_y nanostructures have have minimal, or negative, acid-base interactions bonding with the electron donating poly(imide) material. Mechanical mapping of the cross section provides additional clues to the interface by showing that, on a slightly larger scale than NMR, the bare, ion exchanged, and modified solvothermal LTA show no disruption in the polymer mechanical properties across the

interface. However, the Grignard and original solvothermal MMMs had regions of weaker polymer that propagated from the zeolite. These results support that the functionalized nanostructures that protrude outward form the most continuous polymer properties across the interface and, therefore, are the least disruptive to the interfacial transition.

In conclusion, this work has shown a thorough characterization of every level in a MMM: the filler material, bulk properties, and the interfacial region. All levels of characterization confirm that the ion exchange method is the optimal surface modification method for use in CO_2/CH_4 gas separation membranes. When used in a MMM, it was able to increase in the CO_2/CH_4 selectivity from 30, of the pure polymer, to 40 while maintaining relatively constant CO_2 permeability – a significant improvement. Additionally, the IE method does not appear to disrupt the polymer packing by creating a region of weak polymer region across the interface of the two materials. These developments show that the ion exchange functionalization method of LTA is the most promising path towards a better LTA/Matrimid mixed matrix membrane.

5.3 Future Work

The work in this thesis has contributed to the knowledge of LTA/Matrimid MMMs and the individual methods of functionalization. However, there are several additional avenues for future research in order to grow and advance the MMM field.

5.3.1 Solvothermal Functionalization Mechanism and the Impact of Specific Surface Structures

Chapter 2 showed the solvothermal methods produced different nanostructure shapes and coverages depending on the type of zeolite used. This suggests that the

chemistry of the zeolite surface can actually impact the growth mechanism that guides the shape. Therefore, interesting future work would include several studies to understand this phenomenon. Firstly, the zeolite surface should be thoroughly characterized by zeta potential, or another similar method, to determine the surface charge of the zeolites. Additionally, the surface acidity and basicity can be characterized by contact angle experiments with a variety of basic and acidic liquids. These measurements will give a basic frame of reference for the specific zeolite surface properties and the differences between pure silica and aluminosilicate zeolites. Then, additional work should include a step by step characterization of the zeolites and the growth solution using XPS and TEM at several time points during the reaction. This can be used to determine where the nanostructures are grown, what the intermediate nanostructures look like, and how they grow. These experiments would contribute to a better understanding of the nanostructure growth mechanism, how that may vary with substrate properties, and whether surface a surface pretreatment may aid in forming more desirable nanostructures.

5.3.2 Assessment of Strength in Each Joint of the Interfacial Region

Despite a better understanding of the polymer zeolite interface from the work in Chapter 4, there is still a lot to be learned about the interfacial interactions. Though atomic force microscopy is not representative of the interactions in a true MMM, it can be used to extract a more fundamental understanding. For example, mini tensile strength tests can be conducted to determine the strength of attachment between the nanostructure and zeolite. This can be done by gluing an AFM cantilever to the functionalization and lifting the cantilever off until the break point while simultaneously recording a force curve. Additionally, this type of experiment can be done in situ in the TEM. This

particular method would allow observation of the point of break, such as at the interfacial joint or a break in the nanostructure itself, in addition to the applied force. In situ TEM or SEM tensile testing has been previously applied to measure the tensile strength and clarify the deformation mechanisms in polymer materials by Haque et al. and Zhu et al.[163,164] Additionally, this test can be expanded to approximate MMMs by repeating the same test on a microtomed MMM sample such as those shown in Chapter 3. This would allow observation of the three phase interactions present in MMMs working together: zeolite-nanostructure, nanostructure-polymer, and zeolite-polymer. This work would help to understand the fundamental interfacial mechanics that can contribute to the general composite literature.

Appendix A: Chapter 2 supplemental data

Table A-1. Elemental composition weight % of Ca-exchanged samples normalized to Si by EA, EDX, and XPS. *XPS values are for Na-exchanged samples.

		EA	EDX	XPS	EA	EDX	XPS	EA	EDX	XPS	EA	EDX	XPS
		Wt. % normalized to Si			Weight %			Atom %			Atom % normalized to Si		
LTA	Mg	x	0.0	0.0	x	0.0	0.0	x	0.0	0.0	x	0.0	0.0
	O	x	4.4	1.3	x	68.4	43.9	x	79.0	56.3	x	7.8	2.3
	Al	0.9	0.9	0.5	14.5	13.2	16.4	38.0	9.1	12.5	0.9	0.9	0.5
	Na	0.1	0.1	0.2	1.1	1.3	6.7	3.4	2.1	6.0	0.1	0.2	0.2
	Ca	0.6	0.1	x	9.5	1.5	x	16.7	0.7	x	0.4	0.1	XPS
	Si	1.0	1.0	1.0	16.6	15.4	33.0	41.8	10.2	24.1	1.0	1.0	1.0
Solvothermal	Mg	0.6	0.8	3.3	8.2	10.1	30.0	22.6	7.8	24.2	0.7	0.9	3.8
	O	x	5.0	5.4	x	63.3	49.0	x	74.2	60.0	x	8.8	9.4
	Al	0.9	0.9	1.2	12.3	11.9	11.3	30.4	8.3	8.2	0.9	1.0	1.3
	Na	0.0	0.1	0.1	0.5	1.0	0.6	1.5	0.8	0.5	0.0	0.1	0.1
	Ca	0.5	0.1	x	6.8	0.9	x	11.3	0.4	x	0.3	0.1	x
	Si	1.0	1.0	1.0	14.4	12.7	9.1	34.2	8.5	6.4	1.0	1.0	1.0
Modified Solvo.	Mg	0.3	1.2	1.3	4.4	10.0	19.0	12.6	3.6	14.0	0.3	0.3	1.6
	O	x	7.9	3.6	x	64.0	51.2	x	75.1	57.1	x	7.3	6.4
	Al	0.9	1.8	1.1	13.6	14.5	15.1	35.1	9.6	10.0	0.9	0.9	1.1
	Na	0.0	0.3	0.0	0.7	2.8	0.6	2.1	1.7	0.4	0.1	0.2	0.0
	Ca	0.4	0.1	x	6.1	0.6	x	10.6	0.5	x	0.3	0.0	x
	Si	1.0	1.0	1.0	15.9	8.1	14.1	39.5	10.3	9.0	1.0	1.0	1.0
Ion Exchange	Mg	0.1	0.1	0.2	1.2	1.5	4.9	3.4	1.2	3.9	0.1	0.1	0.2
	O	x	4.0	2.0	x	64.7	46.8	x	76.0	56.7	x	7.0	3.5
	Al	0.9	0.9	0.9	15.5	14.7	22.6	38.7	10.3	16.2	0.9	0.9	1.0
	Na	0.0	0.1	0.1	0.7	1.2	1.9	2.0	1.9	1.6	0.0	0.2	0.1
	Ca	0.4	0.1	x	7.9	1.5	x	13.2	0.7	x	0.3	0.1	x
	Si	1.0	1.0	1.0	17.8	16.3	23.8	42.7	10.9	16.4	1.0	1.0	1.0
Grignard	Mg	0.2	0.1	1.0	3.2	1.6	18.3	8.2	1.3	13.9	0.2	0.1	1.1
	O	x	4.5	2.3	x	66.1	44.7	x	77.0	51.5	x	7.9	4.1
	Al	0.9	0.9	0.8	15.2	12.7	14.5	35.5	8.8	9.9	0.9	0.9	0.8
	Na	0.0	0.2	0.2	0.8	3.0	3.4	2.1	2.5	2.8	0.1	0.3	0.2
	Ca	0.5	0.1	x	9.0	1.3	x	14.2	0.6	x	0.4	0.1	x
	Si	1.0	1.0	1.0	17.8	14.7	19.1	40.0	9.8	12.5	1.0	1.0	1.0

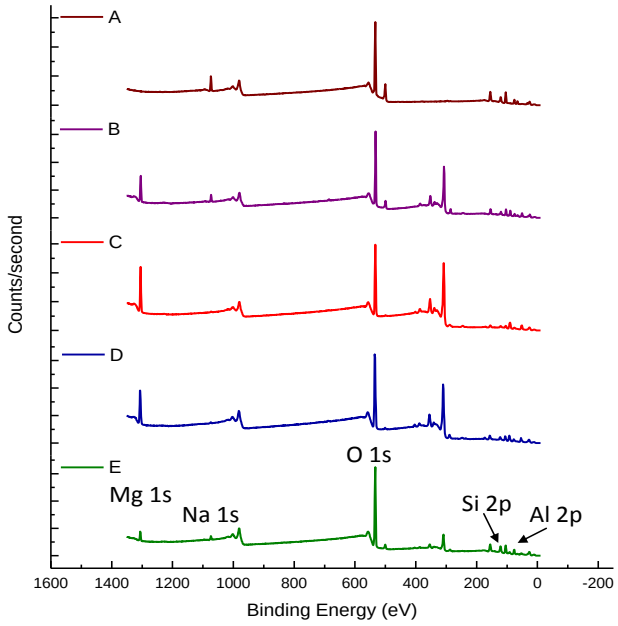

Figure A-1. XPS raw data of (a) unmodified 300 nm LTA particles, and after modification by (b) Grignard, (c) solvothermal, (d) modified solvothermal, and (e) ion exchange methods.

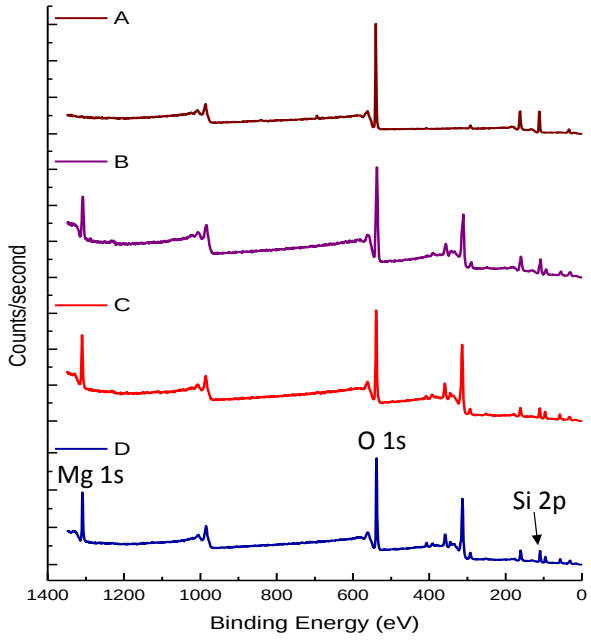

Figure A-2. XPS raw data of (a) unmodified 300 nm MFI particles, and after modification by (b) Grignard, (c) solvothermal, and (d) modified solvothermal methods.

Appendix B: Chapter 4 supplemental data

Section 4.3: NMR measurements.

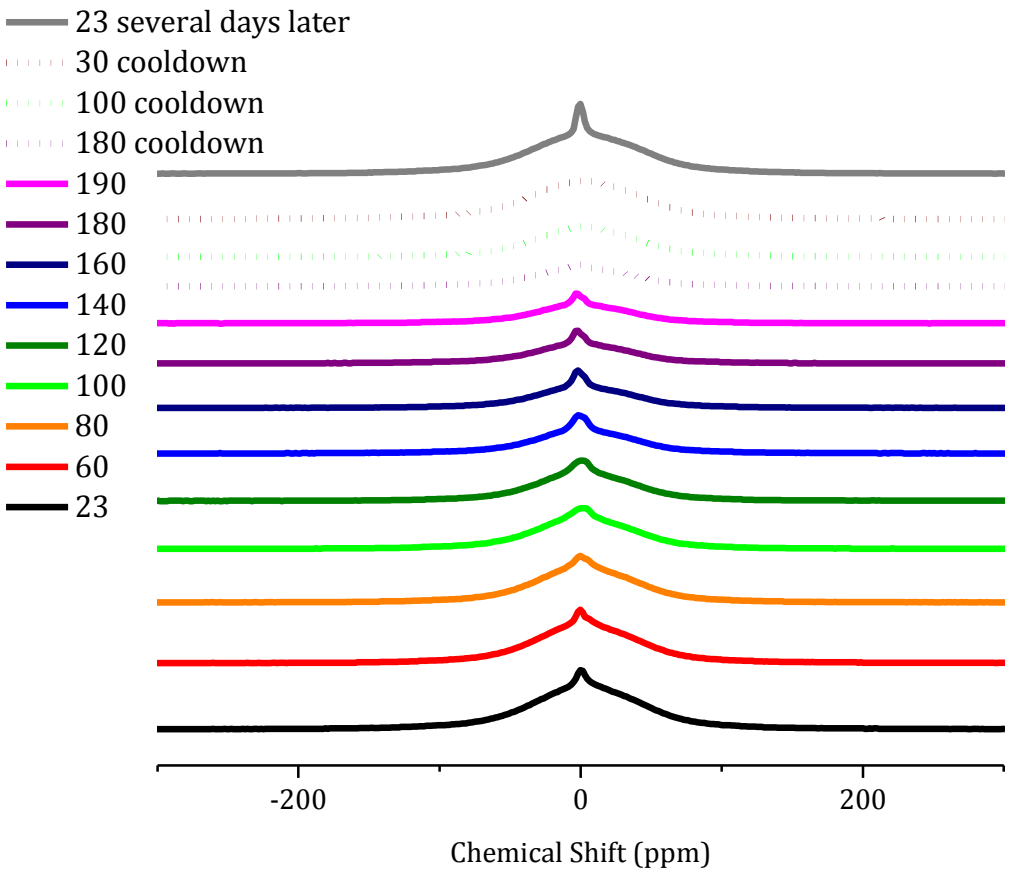

Figure B-3. Matrimid ^{1}H NMR spectra at increasing temperatures

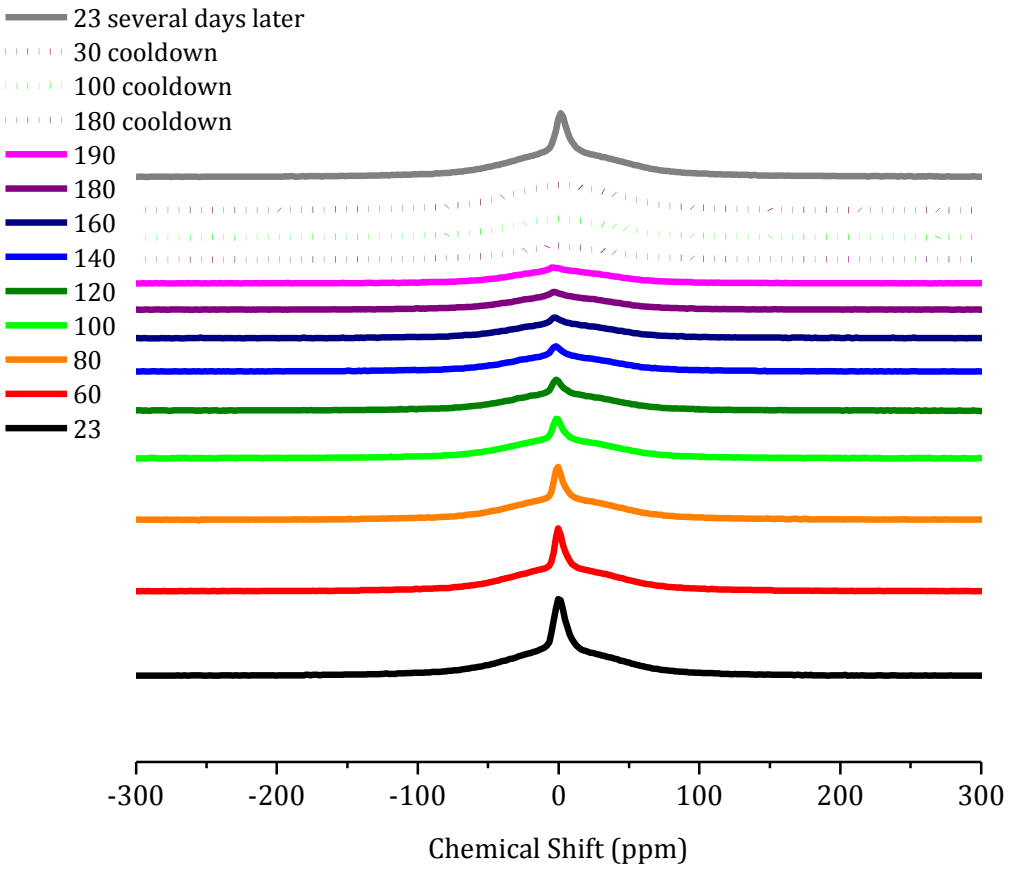

Figure B-4. Bare LTA/Matrimid MMM ^{1}H NMR spectra at increasing temperatures

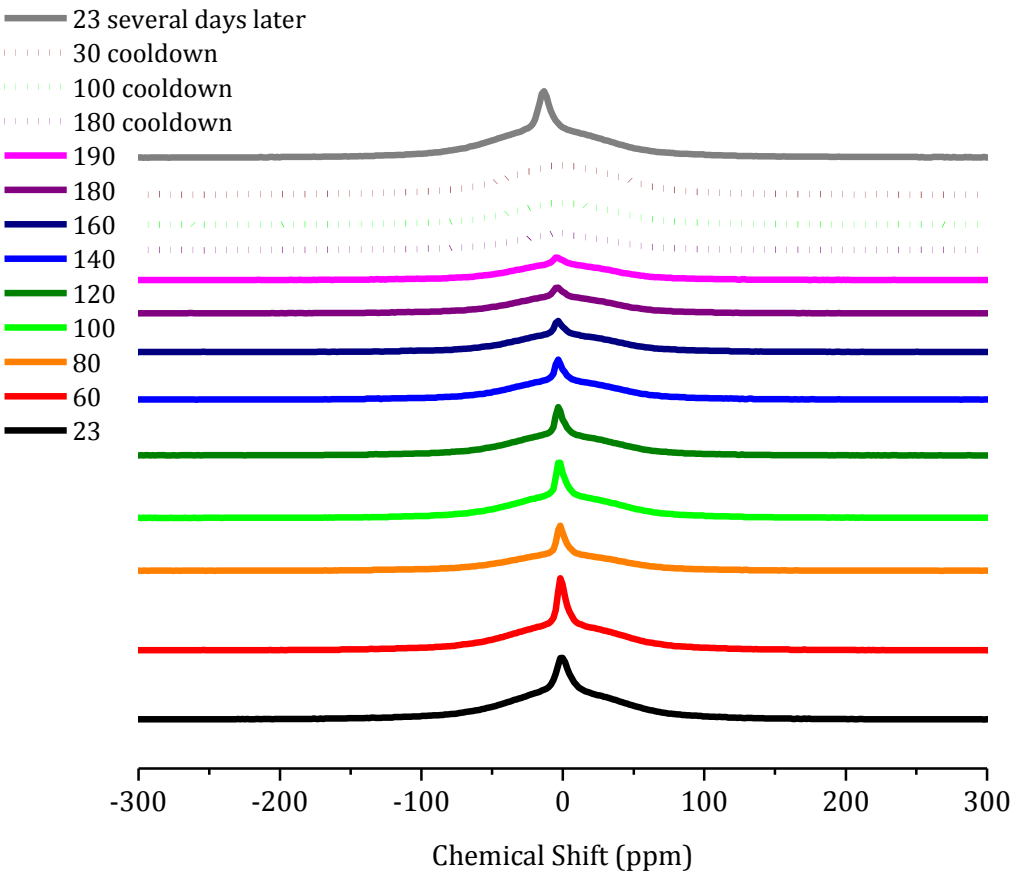

Figure B-5. Ion exchange modified LTA/Matrimid MMM ^{1}H NMR spectra at increasing temperatures

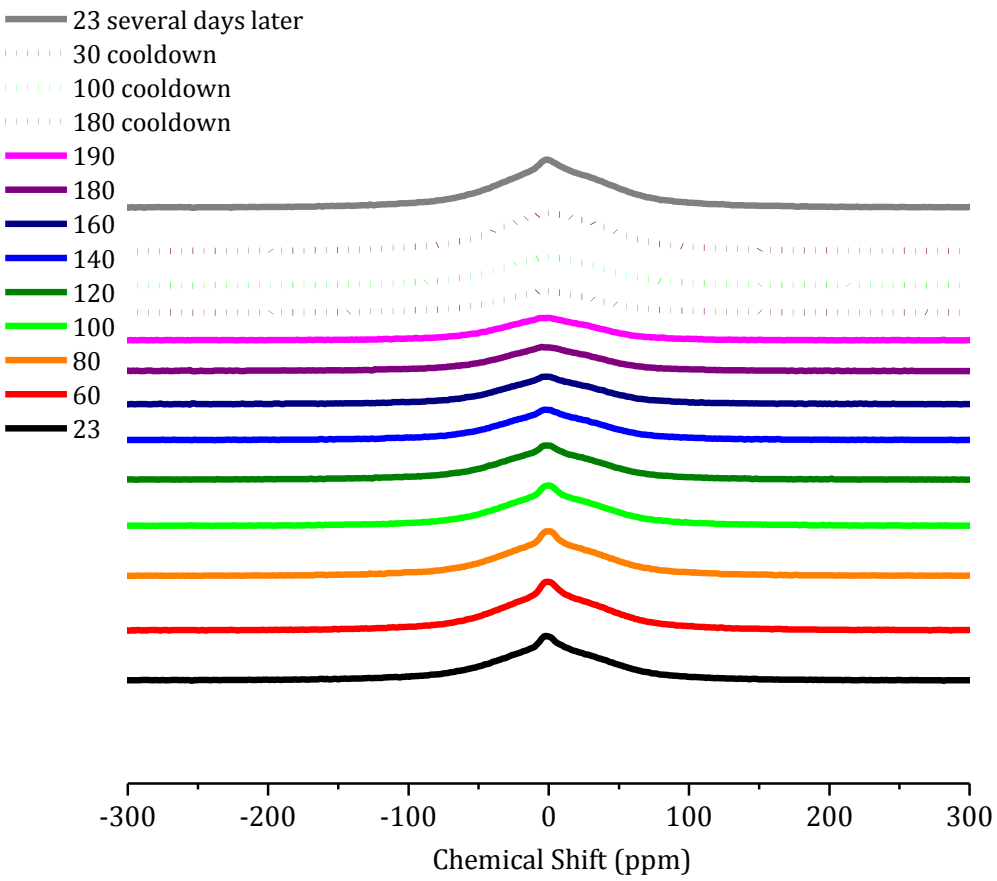

Figure B-6. Modified solvothermal modified LTA/Matrimid MMM ^{1}H NMR spectra at increasing temperatures

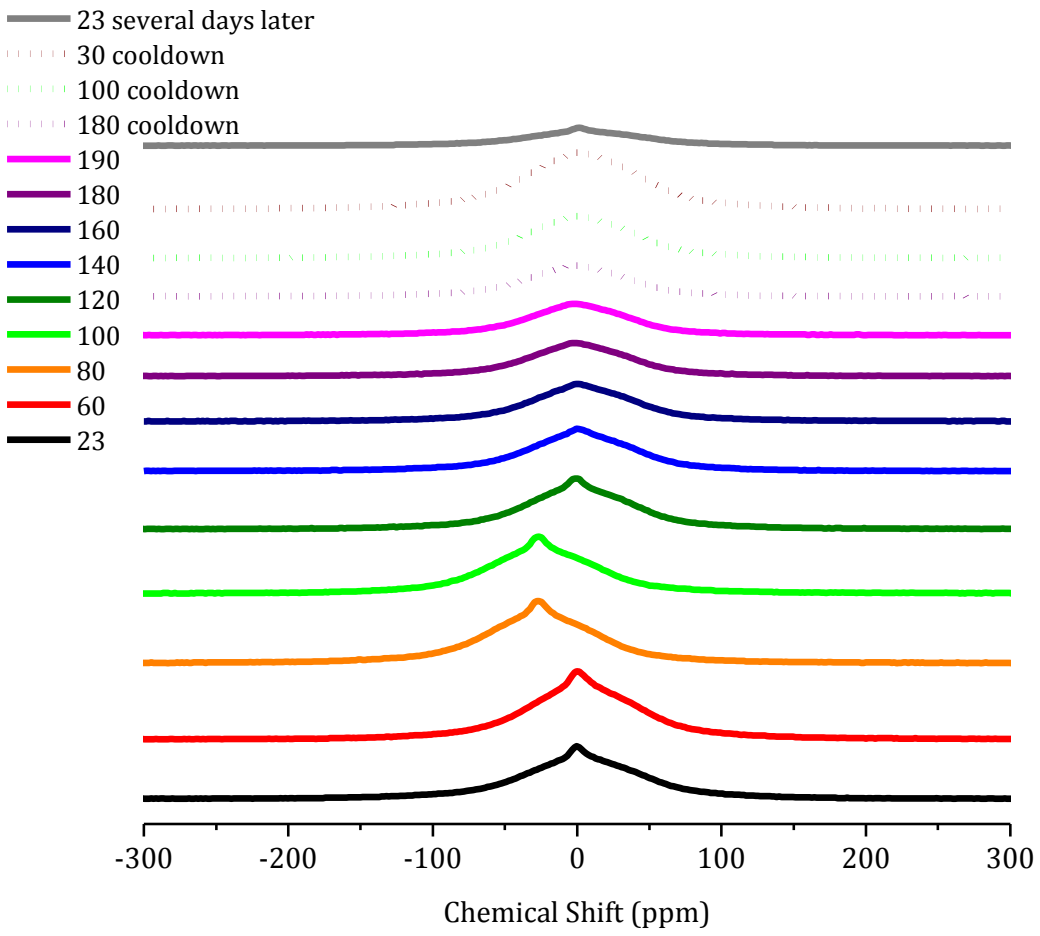

Figure B-7. Original solvothermal modified LTA/Matrimid MMM ^{1}H NMR spectra at increasing temperatures

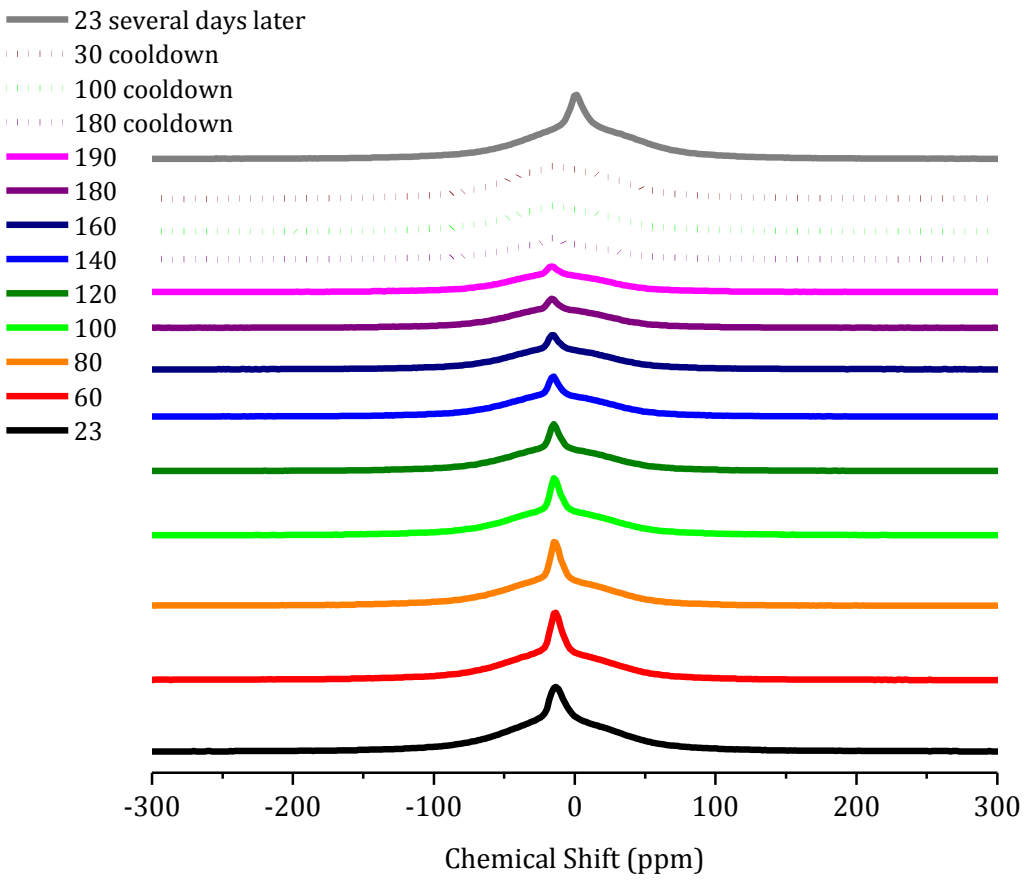

Figure B-8. Original solvothermal modified LTA/Matrimid MMM ^{1}H NMR spectra at increasing temperatures

Table B-2. Relaxation times of the polymer and composite materials measured by NMR.

	Deg. C	A_1	A_2	T_{2-1}	T_{2-2}	A_1/A_2 Ratio	A_1%
Matrimid	30	1.26 ± 0.03	0.50 ± 0.02	36.1 ± 0.5	678 ± 17	2.52	72
	100	1.35 ± 0.03	0.44 ± 0.02	37 ± 0.6	558 ± 30	3.07	75
	180	1.22 ± 0.03	0.50 ± 0.02	41.7 ± 0.6	548 ± 28	2.44	71
	190	1.15 ± 0.03	0.49 ± 0.02	44 ± 0.7	628 ± 30	2.35	70
Bare LTA/ Matrmid	**Deg. C**	**A_1**	**A_2**	**T_{2-1}**	**T_{2-2}**	**A_1/A_2 Ratio**	**A_1%**
	30	1.41 ± 0.05	0.43 ± 0.03	33.6 ± 0.6	607 ± 36	3.28	77
	100	1.3 ± 0.1	0.45 ± 0.07	36 ± 2	710 ± 75	2.89	74
	180	1.25 ± 0.06	0.48 ± 0.04	39 ± 1	586 ± 53	2.60	72
	190	1.3 ± 0.1	0.41 ± 0.07	37 ± 2	652 ± 106	3.17	76
$Mg(OH)_2$/ Matrimid	**Deg. C**	**A_1**	**A_2**	**T_{2-1}**	**T_{2-2}**	**A_1/A_2 Ratio**	**A_1%**
	30	0.7 ± 0.1	1.00 ± 0.06	43 ± 5	658 ± 42	0.70	41
	100	0.49 ± 0.07	1.20 ± 0.06	62 ± 12	658 ± 48	0.41	29
	180	0.45 ± 0.04	1.32 ± 0.06	91 ± 22	604 ± 46	0.34	25
	190	0.38 ± 0.04	1.29 ± 0.06	103 ± 37	703 ± 60	0.29	23
Ion Exch. LTA/ Matrimid	**Deg. C**	**A_1**	**A_2**	**T_{2-1}**	**T_{2-2}**	**A_1/A_2 Ratio**	**A_1%**
	30	1.5 ± 0.3	1.6 ± 0.3	22 ± 2	259 ± 53	0.94	48
	100	0.52 ± 0.03	1.27 ± 0.03	76 ± 11	562 ± 25	0.41	29
	180	0.58 ± 0.02	1.23 ± 0.05	116 ± 28	555 ± 40	0.47	32
	190	0.56 ± 0.03	1.25 ± 0.06	75 ± 7	497 ± 35	0.45	31
Mod. Solvo. LTA/ Matrimid	**Deg. C**	**A_1**	**A_2**	**T_{2-1}**	**T_{2-2}**	**A_1/A_2 Ratio**	**A_1%**
	30	1.2 ± 0.1	0.92 ± 0.09	34 ± 2	378 ± 57	1.30	57
	100	0.68 ± 0.09	0.97 ± 0.06	52 ± 7	682 ± 47	0.70	41
	180	0.56 ± 0.06	1.12 ± 0.06	83 ± 26	654 ± 62	0.50	33
	190	0.59 ± 0.07	1.09 ± 0.05	61 ± 7	630 ± 53	0.54	35
Orig. Solvo. LTA/ Matrimid	**Deg. C**	**A_1**	**A_2**	**T_{2-1}**	**T_{2-2}**	**A_1/A_2 Ratio**	**A_1%**
	30	1.20 ± 0.08	0.87 ± 0.06	35 ± 1	400 ± 43	1.38	58
	100	0.77 ± 0.07	0.96 ± 0.04	46 ± 3	605 ± 40	0.80	45
	180	0.67 ± 0.04	1.14 ± 0.03	62 ± 5	524 ± 26	0.59	37
	190	0.68 ± 0.04	1.12 ± 0.04	59 ± 3	521 ± 29	0.61	38
Grignard LTA/ Matrimid	**Deg. C**	**A_1**	**A_2**	**T_{2-1}**	**T_{2-2}**	**A_1/A_2 Ratio**	**A_1%**
	30	1.09 ± 0.07	1.5 ± 0.9	53 ± 4	227 ± 82	0.73	42
	100	X	X	X	X	X	X
	180	X	X	X	X	X	X
	190	X	X	X	X	X	X

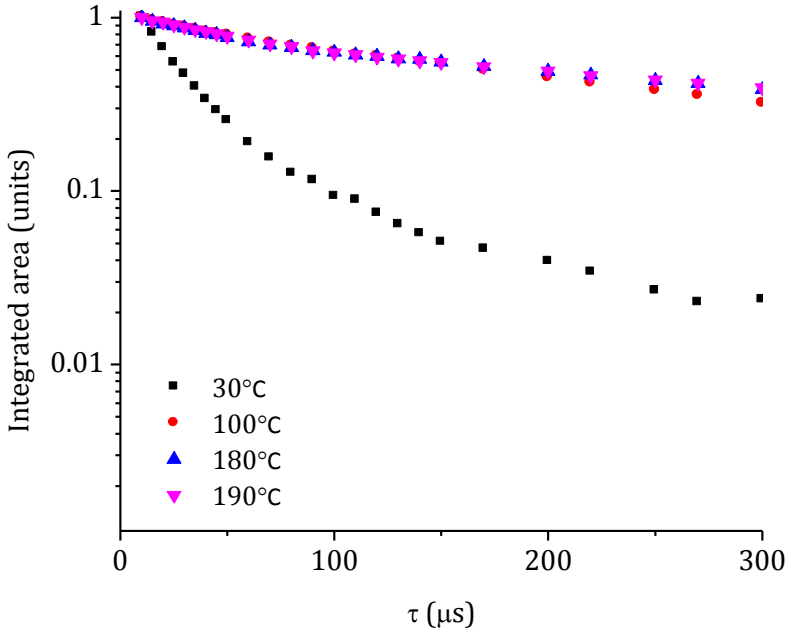

Figure B-9. T_2 relaxation curve for pure, solid zeolite LTA.

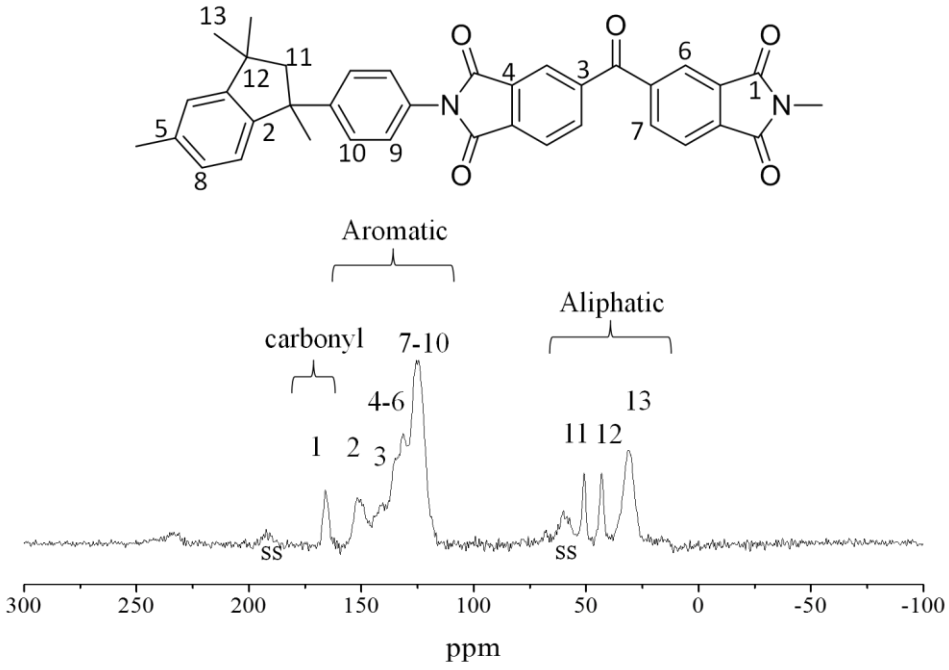

Figure B-10. ^{13}C CP-MAS spectra of Matrimid with a spinning frequency of 11kHz and contact time of 1.0 ms. Peak assignments are based off the work by Grobelny et al.[169]

Section 4.4-Mechanical

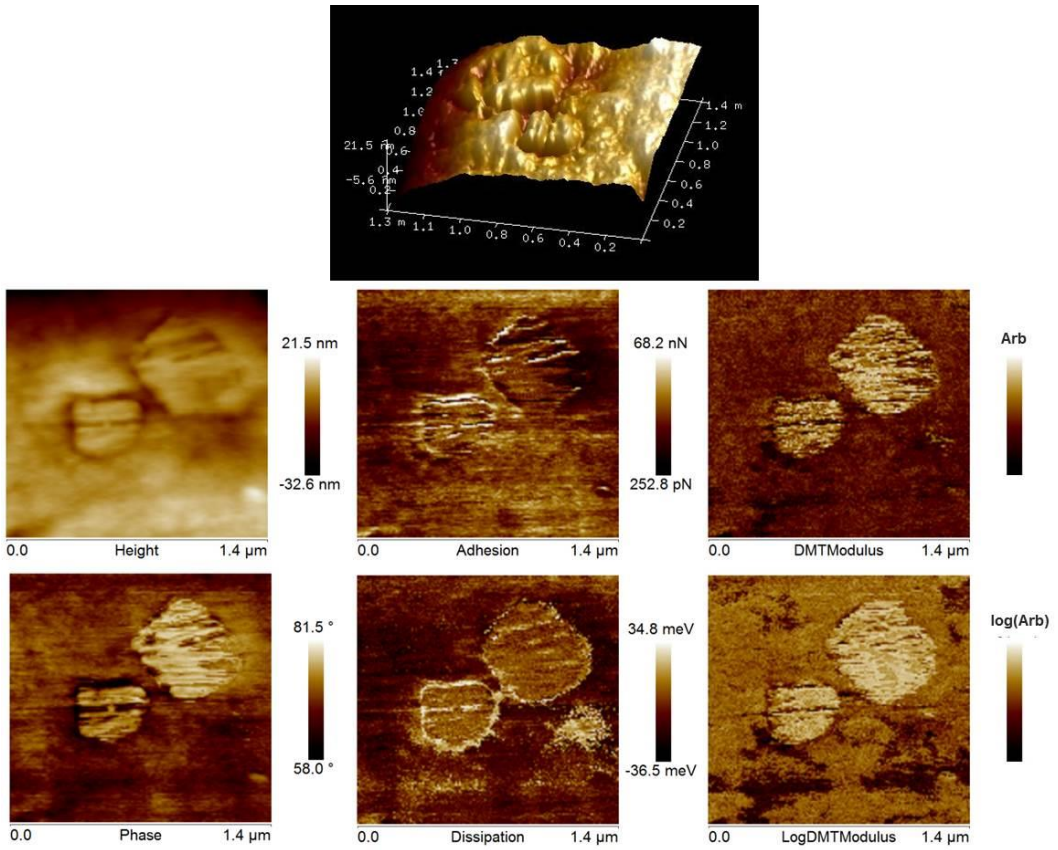

Figure B-11. Atomic force microscopy images of topography and material properties using HarmoniX mode of a cross section of LTA in Matrimid

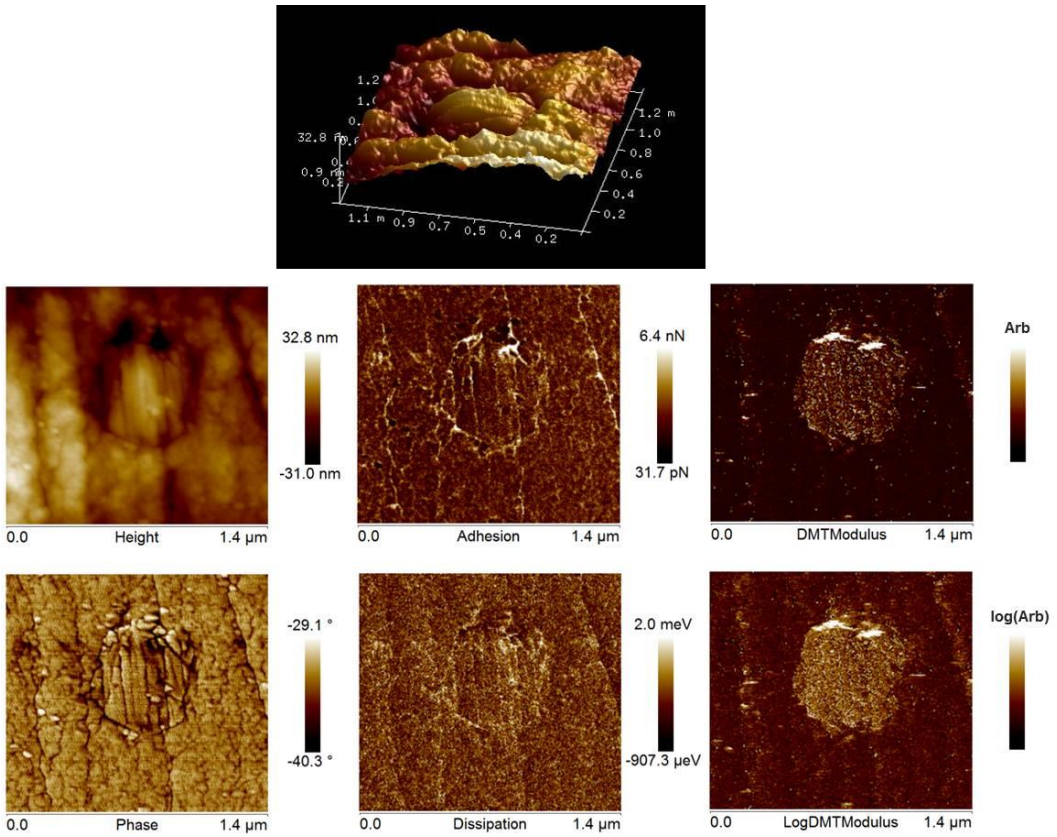

Figure B-12. Atomic force microscopy images of topography and material properties using HarmoniX mode of a cross section of ion exchange functionalized LTA in Matrimid

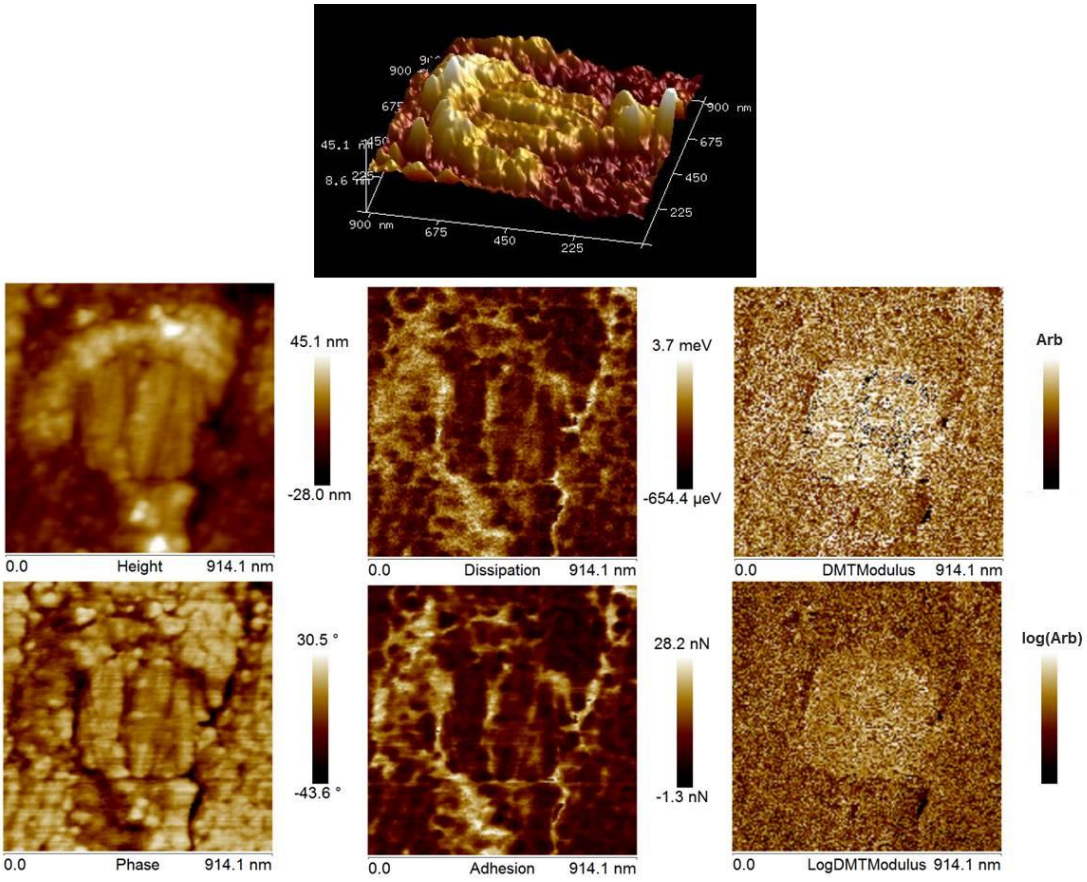

Figure B-13. Atomic force microscopy images of topography and material properties using HarmoniX mode of a cross section of modified solvothermal functionalized LTA in Matrimid

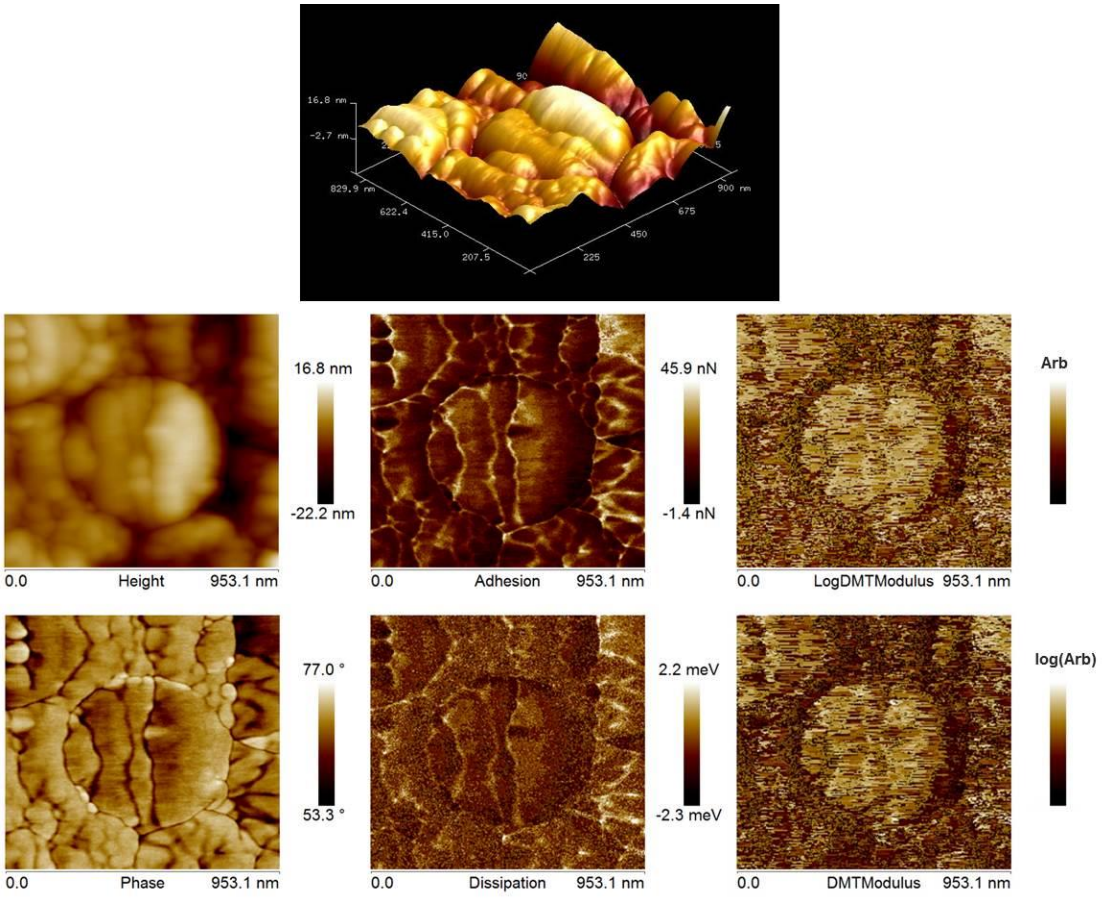

Figure B-14. Atomic force microscopy images of topography and material properties using HarmoniX mode of a cross section of original solvothermal functionalized LTA in Matrimid

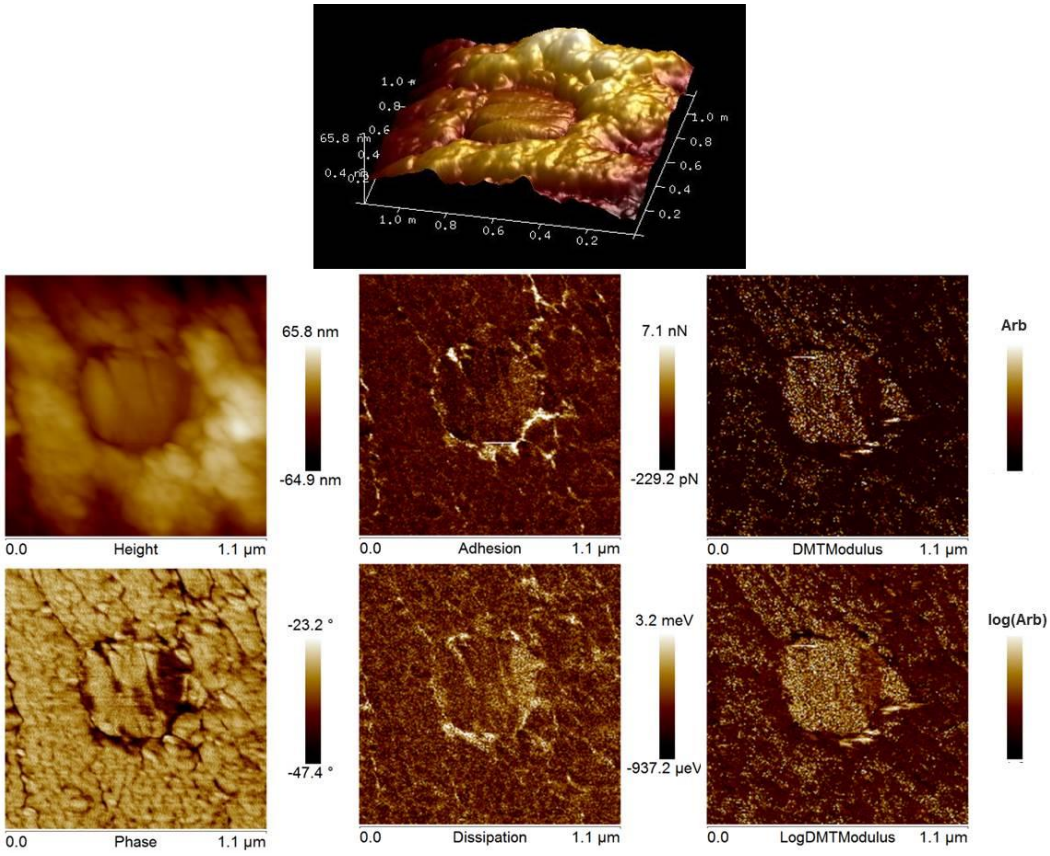

Figure B-15. Atomic force microscopy images of topography and material properties using HarmoniX mode of a cross section of grignard functionalized LTA in Matrimid

References

[1] Z.Y. Yeo, T.L. Chew, P.W. Zhu, A.R. Mohamed, S.-P. Chai, Conventional processes and membrane technology for carbon dioxide removal from natural gas: A review, Journal of Natural Gas Chemistry. 21 (2012) 282–298.

[2] W.M. Burnett, S.D. Ban, Changing prospects for natural gas in the United States, Science. 244 (1989) 305–310.

[3] R.W. Baker, K. Lokhandwala, Natural gas processing with membranes: An overview, Industrial & Engineering Chemistry Research. 47 (2008) 2109–2121.

[4] www.naturalgas.org.

[5] W.J. Koros, R. Mahajan, Pushing the limits on possibilities for large scale gas separation: which strategies? Journal of Membrane Science. 175 (2000) 181–196.

[6] T.-S. Chung, L.Y. Jiang, Y. Li, S. Kulprathipanja, Mixed matrix membranes (MMMs) comprising organic polymers with dispersed inorganic fillers for gas separation, Progress in Polymer Science. 32 (2007) 483–507.

[7] S. Sridhar, B. Smitha, T.M. Aminabhavi, Separation of carbon dioxide from natural gas mixtures through polymeric membranes—A review, Separation & Purification Reviews. 36 (2007) 113–174.

[8] P.S. Goh, A.F. Ismail, S.M. Sanip, B.C. Ng, M. Aziz, Recent advances of inorganic fillers in mixed matrix membrane for gas separation, Separation and Purification Technology. 81 (2011) 243–264.

[9] M. Wang, Y. Dongxiao, Z. Wang, J. Wang, S. Wang, Effects of pressure and temperature on fixed site carrier membranes for CO_2 separation from natural gas, 4 (2010) 127–132.

[10] C.A. Scholes, S.E. Kentish, G.W. Stevens, Carbon dioxide separation through polymeric membrane systems for flue gas applications, (2008) 52–66.

[11] A. Brunetti, F. Scura, G. Barbieri, E. Drioli, Membrane technologies for CO_2 separation, Journal of Membrane Science. 359 (2010) 115–125.

[12] R.T. Adams, J.S. Lee, T.-H. Bae, J.K. Ward, J.R. Johnson, C.W. Jones, et al., CO_2–CH_4 permeation in high zeolite 4A loading mixed matrix membranes, Journal of Membrane Science. 367 (2011) 197–203.

[13] R.F. Boyer, Mechanical motions in amorphous and semi-crystalline polymers, Polymer. 17 (1976) 996–1008.

[14] a. Bos, I.G.M. Punt, M. Wessling, H. Strathmann, I.G.M. Pünt, M. Wessling, et al., Plasticization-resistant glassy polyimide membranes for CO_2/CO4 separations, Separation and Purification Technology. 14 (1998) 27–39.

[15] L.M. Robeson, Correlation of separation factor versus permeability for polymeric membranes, Journal of Membrane Science. 62 (1991) 165–185.

[16] L.M. Robeson, The upper bound revisited, Journal of Membrane Science. 320 (2008) 390–400.

[17] J. Caro, M. Noack, P. Kolsch, R. Schafer, Zeolite membranes - state of their development and perspective, Microporous and Mesoporous Materials. 38 (2000) 3–24.

[18] R. Mahajan, W.J. Koros, Mixed matrix membrane materials with glassy polymers. Part 2, Polymer Engineering and Science. 42 (2002) 1420–1431.

[19] R. Mahajan, W.J. Koros, Mixed matrix membrane materials with glassy polymers. Part 1, Polymer Engineering and Science. 42 (2002) 1432–1441.

[20] A.M.W. Hillock, S.J. Miller, W.J. Koros, Crosslinked mixed matrix membranes for the purification of natural gas: Effects of sieve surface modification, Journal of Membrane Science. 314 (2008) 193–199.

[21] T.-H. Bae, J.Q. Liu, J.S. Lee, W.J. Koros, C.W. Jones, S. Nair, Facile high-yield solvothermal deposition of inorganic nanostructures on zeolite crystals for mixed matrix membrane fabrication, Journal of the American Chemical Society. 131 (2009) 14662–14663.

[22] T.-H. Bae, J. Liu, J. A. Thompson, W.J. Koros, C.W. Jones, S. Nair, Solvothermal deposition and characterization of magnesium hydroxide nanostructures on zeolite crystals, Microporous and Mesoporous Materials. 139 (2011) 120–129.

[23] S.M. Auerbach, K.A. Carrado, P.K. Dutta, Handbook of zeolite science and technology, Marcel Dekker, Inc., New York, 2003.

[24] C. and M. Baerlocher L.B., Database of Zeolite Structures, 2010 (1996).

[25] E.M. Flanigen, J.M. Bennett, R.W. Grose, J.P. Cohen, R.L. Patton, R.M. Kirchner, et al., Silicalite, a new hydrophobic crystalline silica molcular sieve, Nature. 271 (1978) 512–516.

[26] S. Shu, S. Husain, W.J. Koros, A general strategy for adhesion enhancement in polymeric composites by formation of nanostructured particle surfaces, Journal of Physical Chemistry C. 111 (2007) 652–657.

[27] R. Mahajan, W.J. Koros, Factors controlling successful formation of mixed-matrix gas separation materials, Industrial & Engineering Chemistry Research. 39 (2000) 2692–2696.

[28] R. Mahajan, R. Burns, M. Schaeffer, W.J. Koros, Challenges in forming successful mixed matrix membranes with rigid polymeric materials, Journal of Applied Polymer Science. 86 (2002) 881–890.

[29] T.T. Moore, W.J. Koros, Non-ideal effects in organic-inorganic materials for gas separation membranes, Journal of Molecular Structure. 739 (2005) 87–98.

[30] S. Shu, S. Husain, W.J. Koros, Formation of nanostructured zeolite particle surfaces via a halide/Grignard route, Chemistry of Materials. 19 (2007) 4000–4006.

[31] C. Perruchot, M. A. Khan, A. Kamitsi, S.P. Armes, T. von Werne, T.E. Patten, Synthesis of well-defined, polymer-grafted silica particles by aqueous ATRP, Langmuir. 17 (2001) 4479–4481.

[32] J. Pyun, K. Matyjaszewski, Synthesis of nanocomposite organic/inorganic hybrid materials using controlled/“living” radical polymerization, Chemistry of Materials. 13 (2001) 3436–3448.

[33] J.S. Wall, B. Hu, J.A. Siddiqui, R.M. Ottenbrite, Monolayer grafting of organo-silica nanoparticles on poly (ethylene naphthalate) films, Langmuir. 17 (2001) 6027–6029.

[34] T.-H. Bae, Engineering nanoporous materials for application in gas separation membranes, Ph.D. Thesis, Georgia Institute of Technology, 2010.

[35] S. Shu, S. Husain, W.J. Koros, Sonication-assisted dealumination of zeolite A with thionyl chloride, Industrial & Engineering Chemistry Research. 46 (2007) 767–772.

[36] S. Shu, Engineering the performance of mixed matrix membranes for gas separations, Ph.D. Thesis, Georgia Institute of Technology, 2007.

[37] J. Liu, T.-H. Bae, O. Esekhile, S. Nair, C.W. Jones, W.J. Koros, Formation of $Mg(OH)_2$ nanowhiskers on LTA zeolite surfaces using a sol–gel method, Journal of Sol-Gel Science and Technology. 60 (2011) 189–197.

[38] Y.D. Li, M. Sui, Y.Y. Ding, G.H. Zhang, J. Zhuang, C. Wang, et al., Preparation of $Mg(OH)_2$ nanorods, Advanced Materials. 12 (2000) 818–821.

[39] C.S. Cundy, P.A. Cox, The hydrothermal synthesis of zeolites: History and development from the earliest days to the present time, Chemical Reviews. 103 (2003) 663–701.

[40] L. Li, N. Liu, B. Mcpherson, R. Lee, Enhanced water permeation of reverse osmosis through MFI-type zeolite membranes with high aluminum contents, Industrial & Engineering Chemistry Research. 46 (2007) 1584–1589.

[41] C.S. Cundy, P.A. Cox, The hydrothermal synthesis of zeolites: Precursors, intermediates and reaction mechanism, Microporous and Mesoporous Materials. 82 (2005) 1–78.

[42] S.L. Burkett, M.E. Davis, Mechanism of structure direction in the synthesis of Si-ZSM-5 - An investigation by intermolecular ^{1}H ^{29}Si CP MAS NMR, Journal of Physical Chemistry. 98 (1994) 4647–4653.

[43] S. Mintova, Mechanism of zeolite A nanocrystal growth from colloids at room temperature, Science. 283 (1999) 958–960.

[44] H. Yan, J. Wu, X. Zhang, Y. Zhang, L. Wei, X. Liu, et al., Synthesis of magnesium hydroxide nanoneedles and short nanorods on polymer dispersant template, Journal of Materials Research. 22 (2007) 2544–2549.

[45] L. Kumari, W.Z. Li, C.H. Vannoy, R.M. Leblanc, D.Z. Wang, Synthesis, characterization and optical properties of $Mg(OH)_2$ micro-/nanostructure and its conversion to MgO, Ceramics International. 35 (2009) 3355–3364.

[46] M.J. Mckelvy, R. Sharma, A.V.G. Chizmeshya, R.W. Carpenter, K. Streib, Magnesium hydroxide dehydroxylation: In situ nanoscale observations of lamellar nucleation and growth, Chemistry of Materials. 13 (2001) 921–926.

[47] C. Henrist, J.P. Mathieu, C. Vogels, A. Rulmont, R. Cloots, Morphological study of magnesium hydroxide nanoparticles precipitated in dilute aqueous solution, Journal of Crystal Growth. 249 (2003) 321–330.

[48] Z. Zhao, F. Geng, H. Cong, J. Bai, M(OH)2 nanotubes in aqueous solutions of block copolymer P123, 1 (2006) 185–189.

[49] K. Zhu, W. Hua, W. Deng, R.M. Richards, Preparation of MgO Nanosheets with Polar (111) Surfaces by Ligand Exchange and Esterification - Synthesis, Structure, and Application as Catalyst Support, European Journal of Inorganic Chemistry. (2012) 2869–2876.

[50] W.L. Fan, S.X. Sun, X.Y. Song, W.M. Zhang, H.Y. Yu, X.J. Tan, et al., Controlled synthesis of single-crystalline $Mg(OH)_2$ nanotubes and nanorods via a solvothermal process, Journal of Solid State Chemistry. 177 (2004) 2329–2338.

[51] P.C. Lin, C.W. Huang, C.T. Hsiao, H. Teng, Magnesium hydroxide extracted from a magnesium-rich mineral for CO_2 sequestration in a gas-solid system, Environmental Science and Technology. 42 (2008) 2748–2752.

[52] N. Sutradhar, A. Sinhamahapatra, S.K. Pahari, P. Pal, H.C. Bajaj, I. Mukhopadhyay, et al., Controlled synthesis of different morphologies of MgO and their use as solid base catalysts, The Journal of Physical Chemistry C. 115 (2011) 12308–12316.

[53] F. Mohandes, F. Davar, M. Salavati-Niasari, Magnesium oxide nanocrystals via thermal decomposition of magnesium oxalate, Journal of Physics and Chemistry of Solids. 71 (2010) 1623–1628.

[54] A.G.V.G. Chizmeshya, M.J. Mckelvy, R. Sharma, R.W. Carpenter, H. Bearat, Density functional theory study of the decomposition of $Mg(OH)_2$: a lamellar dehydroxylation model, Materials Chemistry and Physics. 77 (2003) 416–425.

[55] S. Ramakrishna, J. Mayer, E. Wintermantel, K.W. Leong, Biomedical applications of polymer-composite materials: a review, Composites Science and Technology. 61 (2001) 1189–1224.

[56] Y. Huang, S. Lv, X. Tian, R.K.Y. Fu, P.K. Chu, Interface analysis of inorganic films on polyimide with atomic oxygen exposure, Surface and Coatings Technology. 216 (2013) 121–126.

[57] P.I. Ravikovitch, A. V Neimark, Density functional theory model of adsorption deformation, Langmuir. 22 (2006) 10864–8.

[58] J.C. Tan, A.K. Cheetham, Mechanical properties of hybrid inorganic-organic framework materials: establishing fundamental structure-property relationships., Chemical Society Reviews. 40 (2011) 1059–80.

[59] B. M. Girish, B. R. Basawaraj, B. M. Satish, D. R. Somashekar, Electrical resistivity and mechanical properties of tungsten carbide reinforced copper alloy composites, International Journal of Composite Materials. 2 (2012) 37–43.

[60] M. Liu, S. Yu, J. Tao, C. Gao, Preparation, structure characteristics and separation properties of thin-film composite polyamide-urethane seawater reverse osmosis membrane, Journal of Membrane Science. 325 (2008) 947–956.

[61] Y. Liu, X.L. Wang, F. Yang, X.R. Yang, Excellent antimicrobial properties of mesoporous anatase TiO2 and Ag/TiO2 composite films, Microporous and Mesoporous Materials. 114 (2008) 431–439.

[62] H. Choi, E. Stathatos, D.D. Dionysiou, Sol-gel preparation of mesoporous photocatalytic TiO2 films and TiO2/Al2O3 composite membranes for environmental applications, Thin Solid Films. 63 (2006) 60–67.

[63] C.M. Zimmerman, A. Singh, W.J. Koros, Tailoring mixed matrix composite membranes for gas separations, Journal of Membrane Science. 137 (1997) 145–154.

[64] G.J. Ehlert, H. a Sodano, Zinc oxide nanowire interphase for enhanced interfacial strength in lightweight polymer fiber composites., ACS Applied Materials & Interfaces. 1 (2009) 1827–33.

[65] K. Zhang, Y. Ma, L.F. Francis, Porous polymer/bioactive glass composites for soft-to-hard tissue interfaces., Journal of Biomedical Materials Research. 61 (2002) 551–63.

[66] I.A. Ibrahim, F.A. Mohamed, E.J. Lavernia, Particulate reinforced metal matrix composites - A review, Journal of Materials Science. 26 (1991) 1137–1156.

[67] V. Abetz, T. Brinkmann, M. Dijkstra, K. Ebert, D. Fritsch, K. Ohlrogge, et al., Developments in membrane research: From material via process design to industrial application, Advanced Engineering Materials. 8 (2006) 328–358.

[68] B. Libby, W.H. Smyrl, E.L. Cussler, Polymer-zeolite composite membranes for direct methanol fuel cells, Polymer. 49 (2003) 991–1001.

[69] M.L. Lind, A.K. Ghosh, A. Jawor, X.F. Huang, W. Hou, Y. Yang, et al., Influence of zeolite crystal size on zeolite-polyamide thin film nanocomposite membranes, Langmuir. 25 (2009) 10139–10145.

[70] R. Mahajan, W.J. Koros, Mixed matrix membrane materials with glassy polymers. Part 1, Polymer Engineering and Science. 42 (2002) 1420–1431.

[71] J.-S. Ye, H.F. Cui, X. Liu, T.M. Lim, W.-D. Zhang, F.-S. Sheu, Preparation and characterization of aligned carbon nanotube-ruthenium oxide nanocomposites for supercapacitors., Small. 1 (2005) 560–5.

[72] E.T. Thostenson, W.Z. Li, D.Z. Wang, Z.F. Ren, T.W. Chou, Carbon nanotube/carbon fiber hybrid multiscale composites, Journal of Applied Physics. 91 (2002) 6034.

[73] Y.-Y. Lin, C.-W. Chen, T.-H. Chu, W.-F. Su, C.-C. Lin, C.-H. Ku, et al., Nanostructured metal oxide/conjugated polymer hybrid solar cells by low temperature solution processes, Journal of Materials Chemistry. 17 (2007) 4571.

[74] W. Kowbel, C. Bruce, J. Withers, P. Ransone, Effect of carbon fabric whiskerization on mechanical properties of CC composites, Composites Part A: Applied Science and Manufacturing. 28 (1997) 993–1000.

[75] Z. Huang, H. Guan, W. Tan, X. Qiao, S. Kulprathipanja, Pervaporation study of aqueous ethanol solution through zeolite-incorporated multilayer poly(vinyl alcohol) membranes: Effect of zeolites, Journal of Membrane Science. 276 (2006) 260–271.

[76] D.W.W. Breck, W.G.G. Eversole, R.M.M. Milton, T.B.B. Reed, T.L.L. Thomas, Crystalline zeolites. I. The properties of a new synthetic zeolite, type A., Journal of the American Chemical Society. 78 (1956) 5963–5971.

[77] C.-H.H. Cheng, T.-H.H. Bae, B.A. McCool, R.R. Chance, S. Nair, C.W. Jones, Functionalization of the internal surface of pure-silica MFI zeolite with aliphatic alcohols, Journal of Physical Chemistry C. 112 (2008) 3543–3551.

[78] B.J. Schoeman, Analysis of the nucleation and growth of TPA-silicalite-1 at elevated temperatures with the emphasis on colloidal stability, Microporous and Mesoporous Materials. 22 (1998) 9–22.

[79] X. Du, E. Wu, Porosity of microporous zeolites A, X and ZSM-5 studied by small angle X-ray scattering and nitrogen adsorption, Journal of Physics and Chemistry of Solids. 68 (2007) 1692–1699.

[80] D.W. Breck, Zeolite molecular sieves: Structure, chemistry, and use, John Wiley & Sons Ltd., New York, 1974.

[81] R. Rakoczy, Y. Traa, Nanocrystalline zeolite A: synthesis, ion exchange and dealumination, Microporous and Mesoporous Materials. 60 (2003) 69–78.

[82] Y. Ding, G. Zhang, H. Wu, B. Hai, L. Wang, Y. Qian, Nanoscale magnesium hydroxide and magnesium oxide powders: control over size, shape, and structure via hydrothermal synthesis, Chemistry of Materials. 13 (2001) 435–440.

[83] M.M.J. Treacy, J.B. Higgens, eds., Collection of simulated XRD patterns for zeolites, 4th editio, Elsevier, New York, 2001.

[84] M.E. Lydon, K.A. Unocic, T. Bae, C.W. Jones, S. Nair, Structure−property relationships of inorganically surface-modified zeolite molecular sieves for nanocomposite membrane fabrication, Journal of Physical Chemistry C. 116 (2012) 9636–9645.

[85] P.G. Self, H.K.D.H. Bhadeshia, W.M. Stobbs, Lattice spacings from lattice fringes, Ultramicroscopy. 6 (1981) 29–40.

[86] International center for diffraction data, http://www.icdd.com/.

[87] EMAPS Diffraction utilities, http://emaps.mrl.uiuc.edu/.

[88] C.S. Fadley, Instrumentation for surface studies: XPS angular distributions, Journal of Electron Spectroscopy and Related Phenomena. 5 (1974) 725–754.

[89] J. Rouquerol, P. Llewellyn, F. Rouquerol, Is the BET equation applicable to microporous adsorbents?, Studies in Surface Science and Catalysis: Characterization of Porous Solids VII. 160 (2007) 49–56.

[90] J.H. de Boer, B.C. Lippens, B.G. Linsen, J.C.P. Broekhoff, A. van den Heuvel, T.J. Osinga, The t-Curve of multimolecular N2 adsorption, Journal of Colloid and Interface Science. 21 (1966) 405–414.

[91] M.E. Davis, Ordered porous materials for emerging applications, Nature. 417 (2002) 813–821.

[92] S. Turner, J.R. Sieber, T.W. Vetter, R. Zeisler, A.F. Marlow, M.G. Moreno-Ramirez, et al., Characterization of chemical properties, unit cell parameters and particle size distribution of three zeolite reference materials: RM 8850 – zeolite Y, RM 8851 – zeolite A and RM 8852 – ammonium ZSM-5 zeolite, Microporous and Mesoporous Materials. 107 (2008) 252–267.

[93] W.S. Rasband, Image J, http://rsbweb.nih.gov/ij/.

[94] H.S. Khare, D.L. Burris, A quantitative method for measuring nanocomposite dispersion, Polymer. 51 (2010) 719–729.

[95] AFM tip manufacturer, Nanoworld.com.

[96] Hysitron Tip Selection Guide, http://www.hysitron.com/.

[97] W.C. Oliver, G.M. Pharr, Measurement of hardness and elastic modulus by instrumented indentation: Advances in understanding and refinements to methodology, Journal of Materials Research. 19 (2004) 3–20.

[98] W.C. Oliver, G.M.M. Pharr, An improved technique for determining hardness and elastic modulus using load and displacement sensing indentation experiments, Journal of Materials Research. 7 (1992) 1564–1583.

[99] E. Wornyo, K. Gall, F. Yang, W. King, Nanoindentation of shape memory polymer networks, Polymer. 48 (2007) 3213–3225.

[100] T.T. Moore, S. Damle, P.J. Williams, W.J. Koros, Characterization of low permeability gas separation membranes and barrier materials; design and operation conditions, Journal of Membrane Science. 245 (2004) 227–231.

[101] S. Damle, W.J. Koros, Permeation equipment for high-pressure gas separation membranes, Industrial & Engineering Chemistry Research. 42 (2003) 6389–6395.

[102] D.G. Pye, H.H. Hoehn, M. Panar, Measurement of gas permeability of polymers. I. permeabilities in constant volume/variable pressure apparatus, Journal of Applied Polymer Science. 20 (1976) 1921–1931.

[103] M.H.G. Wichmann, M. Cascione, B. Fiedler, M. Quaresimin, K. Schulte, Influence of surface treatment on mechanical behaviour of fumed silica/epoxy resin nanocomposites, Composite Interfaces. 13 (2006) 699–715.

[104] M.Q. Zhang, M.Z. Rong, S.L. Yu, B. Wetzel, K. Friedrich, Effect of particle surface treatment on the tribological performance of epoxy based nanocomposites, Wear. 253 (2002) 1086–1093.

[105] B. Wetzel, F. Haupert, M. Qiu Zhang, Epoxy nanocomposites with high mechanical and tribological performance, Composites Science and Technology. 63 (2003) 2055–2067.

[106] J.E. Jakes, R.S. Lakes, D.S. Stone, Broadband nanoindentation of glassy polymers: Part II. Viscoplasticity, Journal of Materials Research. 27 (2011) 475–484.

[107] J. Sun, L.F. Francis, W.W. Gerberich, Mechanical properties of polymer-ceramic nanocomposite coatings by depth-sensing indentation, Polymer Engineering & Science. 45 (2005) 207–216.

[108] J.H. Park, S.C. Jana, The relationship between nano- and micro-structures and mechanical properties in PMMA–epoxy–nanoclay composites, Polymer. 44 (2003) 2091–2100.

[109] Y. Jiang, K. Tohgo, Y. Shimamura, Ultrasonic dispersion of SiO2 particles in glassy epoxy resin, Journal of Composite Materials. 46 (2011) 1159–1168.

[110] W. Soboyejo, Mechanical properties of engineered materials, Marcel Dekker, Inc., New York, NY, 2003.

[111] R. Tilley, Understanding solids: The science of materials, John Wiley & Sons Ltd., Hoboken, NJ, 2004.

[112] Z. Guo, T. Pereira, O. Choi, Y. Wang, H.T. Hahn, Surface functionalized alumina nanoparticle filled polymeric nanocomposites with enhanced mechanical properties, Journal of Materials Chemistry. 16 (2006) 2800.

[113] P. Musto, G. Ragosta, G. Scarinzi, L. Mascia, Polyimide-silica nanocomposites: spectroscopic, morphological and mechanical investigations, Polymer. 45 (2004) 1697–1706.

[114] S. Zhao, L. Schadler, H. Hillborg, T. Auletta, Improvements and mechanisms of fracture and fatigue properties of well-dispersed alumina/epoxy nanocomposites, Composites Science and Technology. 68 (2008) 2976–2982.

[115] S. Ahmed, F.R. Jones, A review of particulate reinforcement theories for polymer composites, Journal of Materials Science. 25 (1990) 4933–4942.

[116] U. Maitra, K.E. Prasad, U. Ramamurty, C.N.R. Rao, Mechanical properties of nanodiamond-reinforced polymer-matrix composites, Solid State Communications. 149 (2009) 1693–1697.

[117] Z. Zhang, K. Friedrich, Tribological characteristics of micro- and nanoparticle filled polymer composites, in: Polymer Composites, Springer, New York, 2005: pp. 169–185.

[118] D. Devaprakasam, P. V. Hatton, G. Möbus, B.J. Inkson, Nanoscale tribology, energy dissipation and failure mechanisms of nano- and micro-silica particle-filled polymer composites, Tribology Letters. 34 (2008) 11–19.

[119] V. Cannillo, F. Bondioli, L. Lusvarghi, M. Montorsi, M. Avella, M.E. Errico, et al., Modeling of ceramic particles filled polymer–matrix nanocomposites, Composites Science and Technology. 66 (2006) 1030–1037.

[120] R.K. Patel, B. Bhattacharya, S. Basu, Effect of interphase properties on the damping response of polymer nano-composites, Mechanics Research Communications. 35 (2008) 115–125.

[121] M.L. Oyen, R.F. Cook, A practical guide for analysis of nanoindentation data., Journal of the Mechanical Behavior of Biomedical Materials. 2 (2009) 396–407.

[122] a. Flores, F. Ania, F.J. Baltá-Calleja, From the glassy state to ordered polymer structures: A microhardness study, Polymer. 50 (2009) 729–746.

[123] T.S. Oh, L.P. Buchwalter, J. Kim, Adhesion of polyimides to ceramic substrates: Role of acid-base interactions, Journal of Adhesion Science and Technology. 4 (1990) 303–317.

[124] J.-H.H. Lee, B.J.R. Thio, T.-H.H. Bae, J.C. Meredith, Role of Lewis basicity and van der Waals forces in adhesion of silica MFI zeolites (010) with polyimides., Langmuir. 25 (2009) 9101–7.

[125] L.P. Buchwalter, Adhesion of polyimides to metal and ceramic surfaces: An overview, Journal of Adhesion Science and Technology. 4 (1990) 697–721.

[126] J. Drelich, J.D. Miller, A critical review of wetting and adhesion phenomena in the preparation of polymer-mineral composites, Minerals and Metallurgical Processing. 12 (1995) 197–204.

[127] M.K. Chaudhury, Interfacial interaction between low-energy surfaces, Materials Science and Engineering: Reports. (1996) 97–159.

[128] M. Sato, T. Kanbayashi, N. Kobayashi, Y. Shima, Hydroxyl groups on silica, alumina, and silica-alumina catalysts, Journal of Catalysis. 7 (1967) 342–351.

[129] V.E. Henrich, Electronic structure of mineral surfaces, in: P. V. Brady (Ed.), Physics and Chemistry of Mineral Surfaces, CRC Press, Inc., Boca Raton, 1996: pp. 64–141.

[130] F. Finocchi, C. Noguera, Electronic properties and modifications of acid-base strengths at non-stoichiometric and polar oxide surfaces, in: K.L. Mittal (Ed.), Acid-base Interactions: Relevance to Adhesion Science and Technology, Boston, 2000: pp. 187–204.

[131] G.A. Parks, The isoelectric points of solid oxides, solid hydroxides, and aqueous hydroxo complex systems, Chem. Rev. 65 (1965) 177–198.

[132] K.F. Hayes, L.E. Katz, Application of x-ray absorption spectroscopy for surface complexation modeling of metal ion sorption, in: P. V. Brady (Ed.), Physics and Chemistry of Mineral Surfaces, CRC Press, Inc., Boca Raton, 1996: pp. 148–220.

[133] M.M. Chehimi, A. Azioune, E. Cabet-Deliry, Acid-base interactions: relevance to adhesion and adhesive bonding, in: A. Pizzi, K.L. Mittal (Eds.), Handbook of Adhesive Technology, 2nd editio, Marcel Dekker, Inc., New York, NY, 2003: pp. 95–144.

[134] L.P. Buchwalter, Adhesion of polyimides to metals and metal oxides, Journal of Adhesion Science and Technology. 1 (1987) 341–347.

[135] E.L. Hahn, D.E. Maxwell, Spin echo measurements of nuclear spin coupling in molecules, Physical Review. 88 (1952) 1070–1084.

[136] J.P. Hornak, The basics of NMR: a hypertext book on nuclear magnetic resonance spectroscopy, http://www.cis.rit.edu/htbooks/nmr/chap-1/chap-1.htm.

[137] D.C. Douglass, V.J. Mcbrierty, Interfacial effects on the NMR of composite polymers, Polymer Engineering and Science. 19 (1979) 1054–1063.

[138] G. Simon, K. Baumann, W. Gronski, Mc determination and molecular dynamics in cross-linked 1,4-cis-polybutadiene: A comparison of transversal, Macromolecules. 25 (1992) 3624–3628.

[139] J. Leisen, I.J. Gomez, J. a Roper, J.C. Meredith, H.W. Beckham, Spatially resolved solid-state ^{1}H NMR for evaluation of gradient-composition polymeric libraries., ACS Combinatorial Science. (2012).

[140] J. Leisen, J. Breidt, ^{1}H NMR relaxation studies of cured natural rubbers with different carbon black fillers, Rubber Chemistry and Technology. 72 (1999) 1–14.

[141] A. Papon, K. Saalwächter, K. Schäler, L. Guy, F. Lequeux, H. Montes, Low-field NMR investigations of nanocomposites: Polymer dynamics and network effects, Macromolecules. 44 (2011) 913–922.

[142] S.-G. Choi, W.L. Kerr, Effects of chemical modification of wheat starch on molecular mobility as studied by pulsed ^{1}H NMR, LWT - Food Science and Technology. 36 (2003) 105–112.

[143] E.L. Hahn, Spin echoes, Physical Review. 80 (1950) 580–594.

[144] Queen's University, Basic Concepts T_2 - Relaxation time, (1999).

[145] B. Xu, J. Leisen, U. Boehme, U. Scheler, H.W. Beckham, ^{1}H NMR T_1 relaxation of polymer/montmorillonite nanocomposites with different clay contents and degrees of exfoliation: Magnetic field effects, Z. Phys. Chem. 226 (2012) 1229–1241.

[146] B. Xu, J. Leisen, H.W. Beckham, R. Abu-Zurayk, E. Harkin-Jones, T. McNally, Evolution of clay morphology in polypropylene/montmorillonite nanocomposites upon equibiaxial stretching: A solid-state NMR and TEM approach, Macromolecules. 42 (2009) 8959–8968.

[147] H. Tanaka, T. Nishi, Spin diffusion in block copolymers as studied by pulsed NMR, Physical Review B. 33 (1986) 32–42.

[148] W. Kuhn, P. Barth, S. Hafner, G. Simon, H. Schneider, Material properties imaging of cross-linked polymers by NMR, Macromolecules. 27 (1994) 5773–5779.

[149] J.C. Kenny, V.J. McBrierty, Z. Rigbi, D.C. Douglass, Carbon black filled natural rubber. 1. Structural investigations, Macromolecules. 24 (1991) 436–443.

[150] D. Moldovan, R. Fechete, D.E. Demco, E. Culea, B. Blümich, V. Herrmann, et al., The heterogeneity of segmental dynamics of filled EPDM by ^{1}H transverse relaxation NMR., Journal of Magnetic Resonance. 208 (2011) 156–62.

[151] B. Blumich, P. Blumler, K. Saito, NMR imaging and spatial information, in: I. Ando, T. Asakura (Eds.), Solid State NMR of Polymers (Studies in Physical and Theoretical Chemistry), 1st ed., Elsevier Science B.V., Amsterdam, 1998: pp. 123–163.

[152] D. Moldovan, R. Fechete, D.E. Demco, E. Culea, B. Blümich, V. Herrmann, et al., Heterogeneity of Nanofilled EPDM Elastomers Investigated by Inverse Laplace Transform ^{1}H NMR Relaxometry and Rheometry, Macromolecular Chemistry and Physics. 211 (2010) 1579–1594.

[153] T. Asakura, T. Ito, Poly(ethylene terephthalate), in: I. Ando, T. Asakura (Eds.), Solid State NMR of Polymers (Studies in Physical and Theoretical Chemistry), 1st ed., Elsevier Science B.V., Amsterdam, 1998: pp. 491–507.

[154] D.E. Axelson, Carbon-13 solid-state NMR of semicrystalline polymers, in: R.A. Komoroski (Ed.), High Resolution NMR Spectroscopy of Synthetic Polymers in Bulk, VCH Publishers, Inc., 1986: pp. 157–226.

[155] F. Zhou, W.J. Koros, Study of thermal annealing on Matrimid® fiber performance in pervaporation of acetic acid and water mixtures, Polymer. 47 (2006) 280–288.

[156] T.K. Kwei, T. Nishi, R.F. Roberts, A study of compatible polymer mixtures, Macromolecules. 7 (1974) 667–674.

[157] J.E. Anderson, D.D. Davis, W.P. Slichter, Pressure dependence of molecular motion in some elastomers, Macromolecules. 2 (1969) 166–169.

[158] J. Wang, J. Zhang, B. Li, M. Ding, Z. Feng, NMR spectra of polyimides: Interpretation and local chain motion study, Macromolecular Chemistry and Physics. 197 (1996) 651–666.

[159] V.J. McBrierty, K.J. Packer, Nuclear magnetic resonance in solid polymers, Cambridge University Press, Cambridge, UK, 1993.

[160] O. Sahin, S. Magonov, C. Su, C.F. Quate, O. Solgaard, An atomic force microscope tip designed to measure time-varying nanomechanical forces., Nature Nanotechnology. 2 (2007) 507–14.

[161] J.N. Israelachvili, Intermolecular and surface forces, 3rd editio, Academic Press Inc., Amsterdam, 2011.

[162] M.E. Dokukin, I. Sokolov, Quantitative mapping of the elastic modulus of soft materials with HarmoniX and PeakForce QNM AFM modes., Langmuir. 28 (2012) 16060–71.

[163] M.A. Haque, M.T.A. Saif, In-situ tensile testing of nano-scale specimens in SEM and TEM, Experimental Mechanics. 42 (2002) 123–128.

[164] Y. Zhu, H.D. Espinosa, An electromechanical material testing system for in situ electron microscopy and applications., Proceedings of the National Academy of Sciences of the United States of America. 102 (2005) 14503–8.

[165] A. Erdem-Şenatalar, M. Tatlier, Ş. Birgül Tantekin-Ersolmaz, Questioning the validity of present models for estimating the performances of zeolite- polymer mixed matrix membranes, Chemical Engineering Communications. 190 (2003) 677–692.

[166] S. Suzuki, H. Takaba, T. Yamaguchi, S. Nakao, Estimation of gas permeability of a zeolite membrane, based on a molecular simulation technique and permeation model, The Journal of Physical Chemistry B. 104 (2000) 1971–1976.

[167] T.T. Moore, Effects of materials, processing, and operating conditions on the morphology and gas transport properties of mixed matrix membranes, Ph.D. thesis, University of Texas at Austin, 2004.

[168] W. Derbyshire, M. Van Den Bosch, D. Van Dusschoten, W. MacNaughtan, I.A. Farhat, M.A. Hemminga, et al., Fitting of the beat pattern observed in NMR free-induction decay signals of concentrated carbohydrate-water solutions., Journal of Magnetic Resonance. 168 (2004) 278–83.

[169] J. Grobelny, D.M. Rice, F.E. Karasz, W.J. Macknight, High Resolution Solid-State Carbon-13 Nuclear Magnetic Resonance Study of Polybenzimidazole/Polyimide, Macromolecules. 2139 (1990) 2139–2144.

Vita

MEGAN ELIZABETH LYDON

Megan Lydon was born in San Jose, California to Donna and George Lydon. She received a B.S. in Chemistry from California Polytechnic State University, San Luis Obispo in 2008 before coming to Georgia Tech to pursue a doctorate in physical chemistry. When she is not working on her research, Megan enjoys exploring Atlanta and the south, travelling internationally, going to concerts and festivals, and reading. Megan will start her career at IBM in Essex Junction, Vt. in the fall as a chemistry lab engineer.